Delft University of Technology

Graduate Thesis

Comparative analysis of common practice fatigue versus multiaxial fatigue applied to a floating unit for wind turbine installation

Author:
S.T. Verlaan

Graduation committee:
Prof.dr.ir. M.L. Kaminski
ir. G.J. Grundlehner
dr. ir. Z. Li
ir. P. van Lieshout
ir. O. Sainz Avila

A thesis submitted in fulfilment of the requirements
for the degree of Master of Science
in

Offshore & Dredging Engineering
Structural Analysis and Design

November 2015

TU Delft Delft University of Technology

Boskalis

DELFT UNIVERSITY OF TECHNOLOGY

Abstract

Offshore & Dredging Engineering
Structural Analysis and Design

Master of Science

Comparative analysis of common practice fatigue versus multiaxial fatigue applied to a floating unit for wind turbine installation

by S.T. Verlaan

The demands for lighter structures and material saving constructions are leading to designs which approach the limit in strength of material. Therefore carrying out a fatigue analysis as part of the structural analysis becomes even more important. The objective of the thesis is to compare a common practice fatigue analysis with a multiaxial fatigue analysis for an installation unit that can install gravity based offshore wind turbines (up to 10MW) in its entirety.
The installation unit is a semi-submersible that can float around the foundation of the wind turbine which sits on a semi-submersible transport vessel. Then the installation unit docks on the transportation vessel and lifts the wind turbine with foundation. After that it will float off to the desired location where the installation unit submerges and places the wind turbine in a prepared pit on the sea bed. And finally the installation unit disconnects from the foundation of the wind turbine and returns to floater draft.
The installation unit consists of a floater, three columns and braces connecting the columns. The comparative fatigue analysis is done for a fillet weld connecting the diagonal brace with the floater. The weld is loaded by swell beam waves and wind sea waves coming from a variable direction. The loading causes cyclic stresses near the weld which contribute to the calculated fatigue damage. The stresses considered are the normal stresses perpendicular to the weld and the shear stresses along the weld.

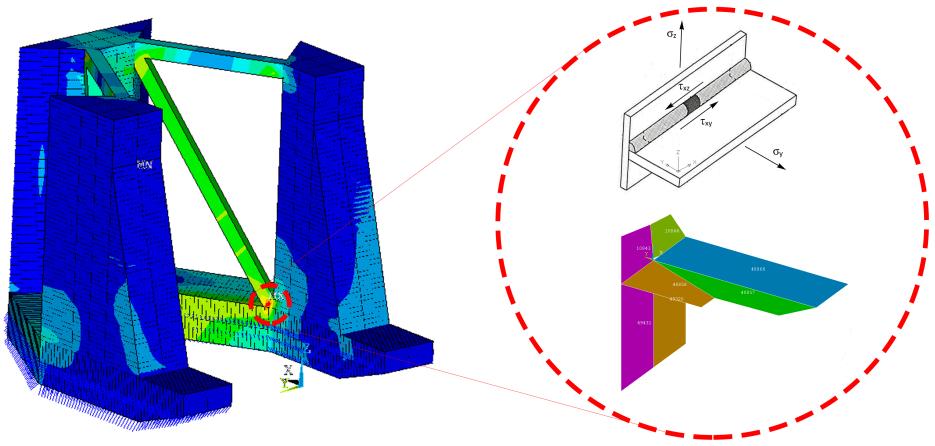

FIGURE 1: Installation unit and weld considered for fatigue analysis

A comparison is made between a common practice fatigue analysis and a multiaxial fatigue analysis. Because it is a qualitative comparison the level of detail of the FEM model is relatively low. The common practice fatigue analysis consists of performing rainflow counting on the stress time traces, relating the stress ranges to the corresponding SN curve and adding the cumulative damage. The multiaxial fatigue analysis consists of performing PDMR (Path Dependent Maximum Range) counting of the stress proportionality ($\sigma - \sqrt{3}\tau$) plot, relating the stress ranges to the corresponding SN curve and adding the cumulative damage.

The calculated fatigue damage depends on the material, the type of welded joint, the FEM model, the loading, cycle counting method and class of SN curve. The actual difference between both fatigue analyses is the simultaneous loading of normal and shear stresses. Experiments have shown that this simultaneous loading causes more fatigue damage. It is therefore considered that for the welded joint on the installation unit the calculated multiaxial fatigue damage will be the conservative method.

Acknowledgements

Starting with just the idea of an installation unit for gravity base wind turbines and ending up with a multiaxial fatigue analysis for a weld in the installation unit. It has been a nice process to go through and I have learned a lot about engineering and doing scientific research. On top of that I got to know Boskalis as a company and decided that I wanted to work for Boskalis after completing my thesis. I am glad and proud to say that I can now continue as a trainee within Boskalis.

I would like to thank Oscar Sainz Avila for the time and effort of being my daily supervisor during my graduation work. Explaining and helping me with subject that were new to him as well most of the times.

I would also like to thank Gertjan Grundlehner for the time and effort of being the overall supervisor. Guiding me with the bigger picture and helping me to keep the relation with the practical aspects of the thesis in mind. And a special thanks to both Gertjan and Oscar for supporting me when I applied for the traineeship within Boskalis.

Of course I want to thank my professor Mirek Kaminski as well. For helping me learn more about structural engineering and having regular progress meetings so there was a clear direction for the graduation thesis. And I would like to thank Paula van Lieshout for aiding me with fatigue related questions. Next I would like to thank Boskalis in general for letting me do my graduation thesis within the company and for letting me finish it even though the traineeship already started.

Finally I would like to thank my parents for raising me the best way possible and making it possible for me to get the Master of Science title. I hope they are proud of me for this achievement.

Contents

List of Figures

List of Tables

Nomenclature

A	(exposed) area	m^2
A_R	reference area	m^2
A_w	area of wetted element	m^2
a	width	m
BM	distance from center of buoyancy to metacenter	m
C	fatigue strength - scaling factor	-
C_A	added mass coefficient	–
C_d	drag coefficient	–
C_h	height coefficient	–
C_m	inertia coefficient	–
C_s	shape coefficient	–
D	cumulative damage	-
E	Young's modulus	[MPa]
F_c	current load	N
F_w	wind load	N
GM	distance from center of gravity to metacenter	m
g	gravitational acceleration	m/s^2
I	moment of inertia	m^4
KB	distance from keel to center of buoyancy	m
KG	distance from keel to center of gravity	m
k	stiffness	N/m
k_a	correction factor for aspect ratio of plate field	-
k_m	bending moment factor	-
k_{pp}	fixation parameter for plate	-
k_{ps}	fixation parameter for stiffeners	-
l	frame/stiffener span	m
M_w	moment due to wind load	Nm
M_y	moment on transverse axis	Nm
m	mass	kg
m_A	added mass per unit length	kg/m

m_s	slope - fatigue damage mechanism	-
N	fatigue life - number of cycles	-
N_i	number of loading cycles to failure	-
n_i	number of repetitions of stress ranges during structure design life	-
p	(lateral) pressure	kN/m^2
S	stress range	MPa
s	stiffener spacing	m
t	plate thickness	mm
u	current velocity	m/s
u_d	Distortion energy per unit volume	$[J/m^3]$
V	volume	m^3
v	vessel velocity	m/s
v_w	design wind speed	m/s
Z_s	section modulus	mm^3
z	vertical distance	m
θ	static trim angle	$^\circ$
θ_{p1}	angle between σ_x and σ_{p1}	$^\circ$
θ_{p2}	angle between σ_y and σ_{p1}	$^\circ$
θ_w	static trim angle due to wind load	$^\circ$
ν	Poisson's ratio	-
ρ_a	density of air	kg/m^3
ρ_w	density of seawater	kg/m^3
σ_1	principal stress 1	MPa
σ_2	principal stress 2	MPa
σ_{pl}	permissible bending stress	MPa
σ_{VM}	permissible bending stress	MPa
σ_x	normal stress in x-direction	MPa
σ_y	normal stress in y-direction	MPa
τ_{xy}	shear stress in xy-plane	MPa
ϕ_w	static heel angle due to wind load	$^\circ$
∇	submerged volume	m^3

Chapter 1

Introduction

In this chapter the relevance of the thesis topic is described and the objective of the thesis is given. The wind turbine installation concept is first explained in short and then a more detailed concept work plan is shown to get a better understanding. Finally a first impression of the scientific content with respect to the concept design is described.

1.1 Relevance thesis topic

Global energy demand continues to grow while fossil fuels, the main source of energy consumption, can not supply enough energy in the long term. To meet this future global energy demand several alternative energy sources are known. A well developed renewable energy source is wind energy. With wind turbines onshore and offshore there are numerous global possibilities.
However, installing wind turbines offshore is still rather inefficient. The majority of offshore wind turbines are bottom founded structures that require piles driven into the seabed, see Figure 1.1. These offshore wind turbines are installed in parts which takes quite some time and requires multiple vessels. To improve the efficiency of offshore wind turbine installation, a development is to install the complete wind turbine in its entirety. There are several options to install a wind turbine in its entirety. One of the options is floating wind turbines. Research in this topic is present but the concept is hard to realize due to tight restrictions on the motions of a wind turbine. Another option is gravity based wind turbine structures, this results in heavy structures. But heavy lift vessels are a huge investment, which brings up the thesis topic. The concept design of a gravity based wind turbine installation unit.

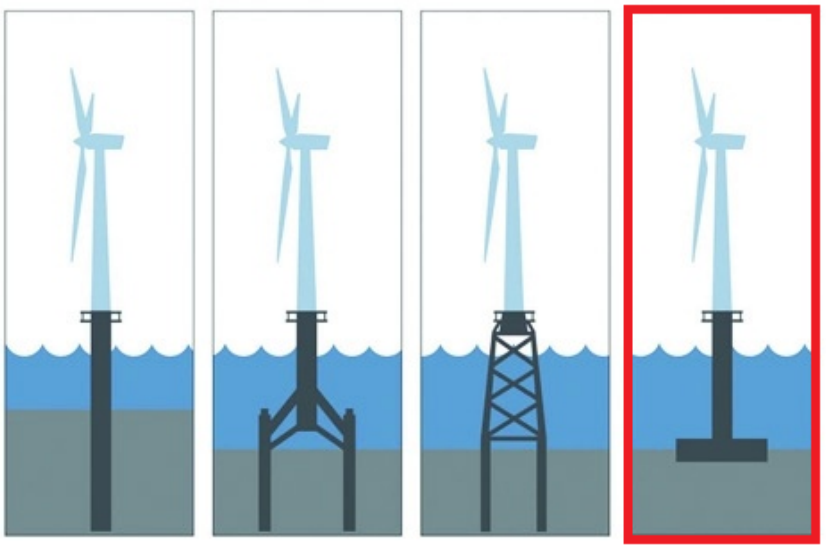

FIGURE 1.1: Bottom founded wind turbines and a gravity based wind turbine (right)

The installation unit would be a semi-submersible unit steel structure. The demands for lighter structures and material saving constructions are leading to designs which approach the limit in strength of material. Marine and offshore structures consist of metal constructions, the majority from structural steel, with welded connections. Operational and environmental loading on these structures are cyclic and cause multiaxial stress states within the structure. More developments on multiaxial fatigue lifetime predictions are needed for structures with optimal fatigue design.

1.2 Thesis objective

The objective of the thesis is to compare a common practice fatigue analysis with a multiaxial fatigue analysis for an installation unit that can install large gravity based offshore wind turbines (up to 10MW) in its entirety. The specifications of the foundation and wind turbine used in this thesis can be found in Appendix A.

1.3 Concept

The gravity based wind turbine is transported by a semi-submersible transport vessel. The installation unit is a semi-submersible that can float around the foundation of the wind turbine which sits on a semi-submersible transport vessel. Then the installation unit docks on the transportation vessel and lifts the wind turbine with foundation. After that it will float off to the desired location where the installation unit submerges and places the wind turbine in a prepared pit on the sea bed. And finally the installation

unit disconnects from the foundation of the wind turbine and returns to floater draft. The design of a comparable installation unit by Freyssinet [1] is shown in Figure 1.2.

FIGURE 1.2: Design of a comparable installation unit by Freyssinet

1.4 Concept work plan

The concept work plan consists of multiple consecutive installation stages. These stages are:

- Unloaded floating (station-keeping by tugboats)
- Docking on transport vessel
- Loaded float off
- Set down gravity based structure

A description is given for each installation stage with an associated schematic illustration.

Unloaded floating

The wind turbine installation unit is either towed or transported on a vessel to location. At location it maintains its position by tugboats, mooring lines or dynamic positioning. In this situation the unit is unloaded but can be ballasted to improve fatigue damage conditions or withstand storm conditions.

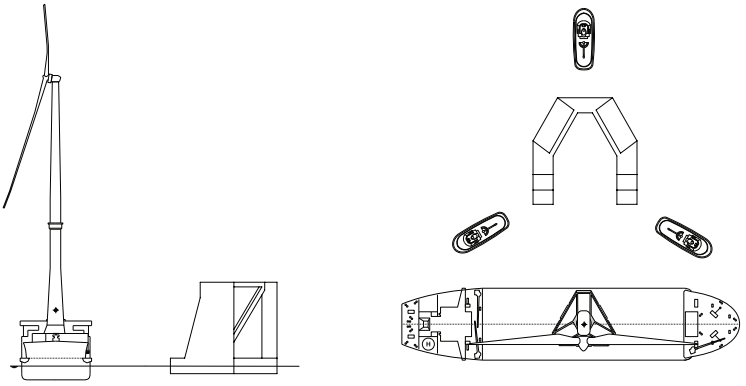

FIGURE 1.3: Unloaded floating (station-keeping by tugboats)

Docking

The transportation vessel loaded with a gravity based wind turbine arrives at location. The vessel will submerge the deck deep enough for the installation unit to float around the foundation and dock on the vessel. The T-class from Dockwise/Boskalis is expected to be a suitable transportation vessel because there are multiple identical ones which improves the availability. The deck of this vessel is considered large enough for one wind turbine (after placing additional buoyancy tanks) and can submerge the deck nine meters.

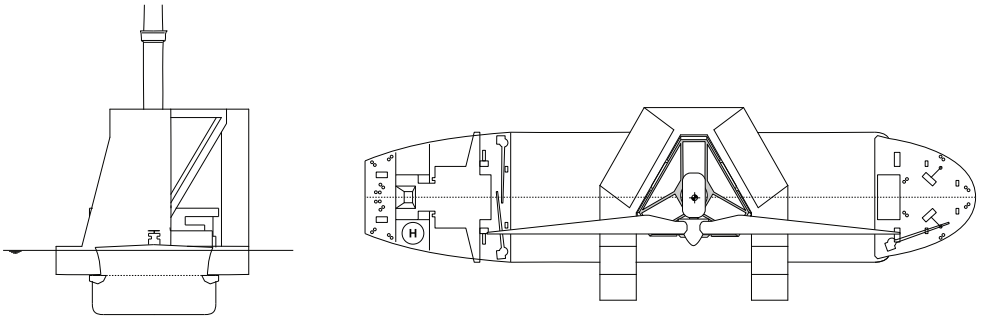

FIGURE 1.4: Docking on transportation vessel

Float off

After docking, the installation unit will connect to the foundation and lift the gravity based structure. The installation unit is now loaded and will float off. This is considered a critical stage of the installation procedure because of the limited space between the installation unit and the transportation vessel.

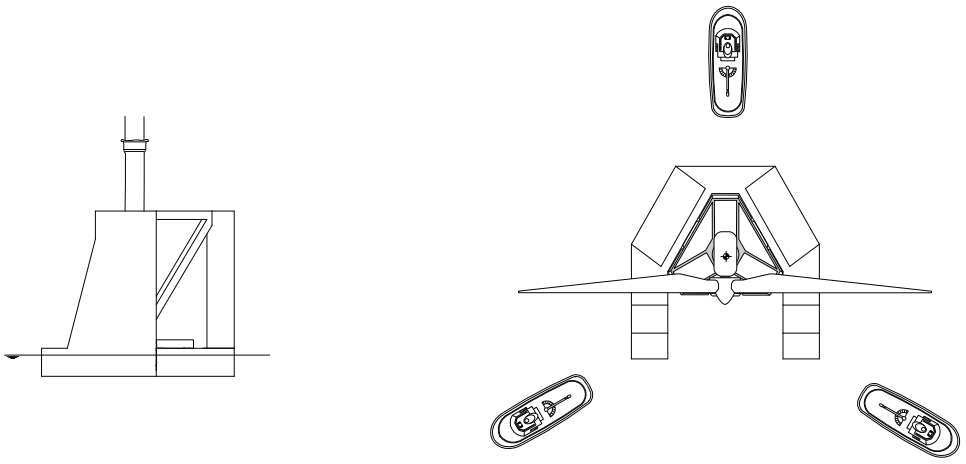

FIGURE 1.5: Loaded float off

Set down

The loaded installation unit is towed to location where it will be ballasted. The combination of structures submerges onto the seabed prepared pit. After set down of the foundation, the installation unit is disconnected and deballasted so it returns to floater draft.

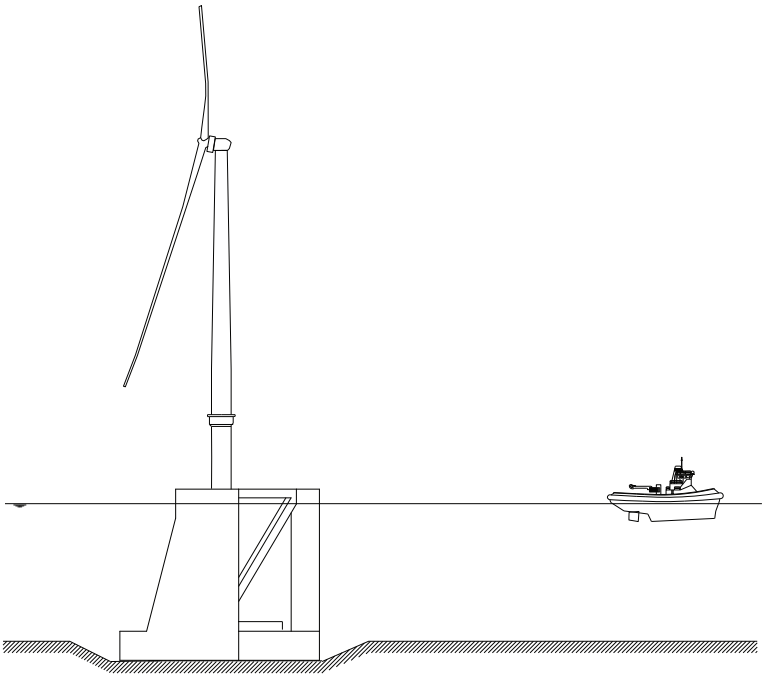

FIGURE 1.6: Set down gravity based structure

1.5 Scientific content

The required shape of the installation unit and the loading due to waves during operation make it that fatigue is considered as significant. Welded joints under proportional (in-phase) cyclic loading are relatively well understood and accepted by the classification societies. However welded joints under non-proportional (out-of-phase) cyclic loading with a multiaxial stress state generally have poor fatigue life predictions according to conventional hypotheses. In this thesis the comparison is made between a common practice and multiaxial fatigue analysis for a weld on the unloaded floating gravity based wind turbine installation unit.

The level of detail of the FEM model used in the analyses is relatively low. For an actual fatigue analysis it is not sufficient but because a comparison is made between different fatigue analyses it is considered sufficient.

Chapter 2

Initial installation unit

In this chapter the design method is explained and the different design constraints and requirements are listed in the design basis. The initial sizing according to hydrostatics of the installation unit is provided and the heave response amplitude operator (RAO) is estimated. The static stability and static loads on the unit are defined with associated trim and/or heel angles. The (local) motions and accelerations will be checked with Amarcon Octopus SEAWAY software based on strip theory. To close the chapter the initial design is presented with dimensions, stability and heel/trim angles and the motion characteristics.

2.1 Design basis

2.1.1 Design spiral

The design of the installation unit proceeds through three stages: concept, preliminary and contract design. The process of initial design is illustrated by the design spiral (Figure 2.1) which indicates that given the objectives, the design works towards the best solution adjusting and balancing the interrelated parameters.

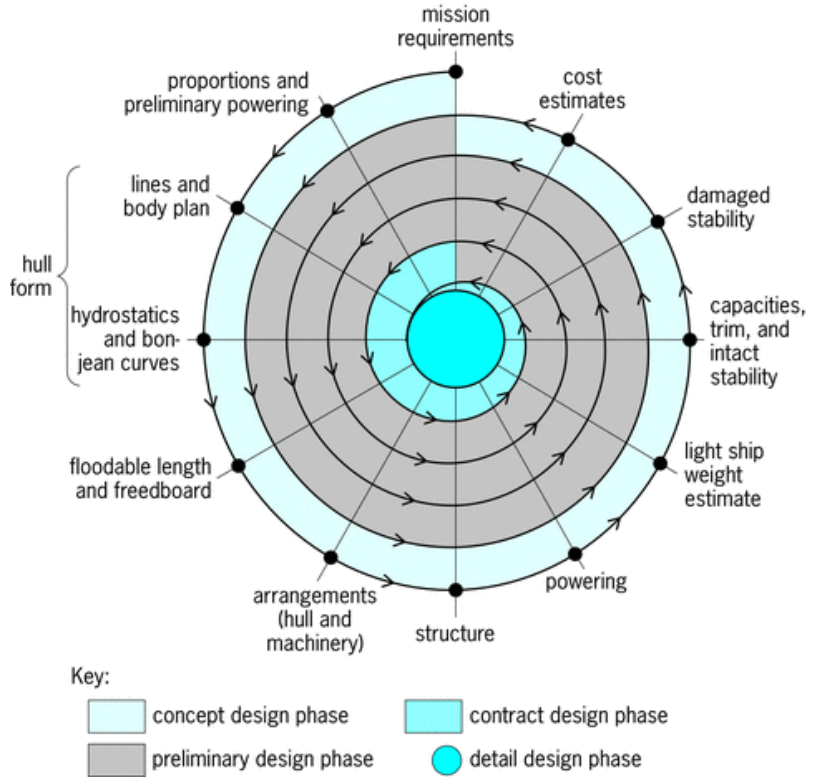

FIGURE 2.1: Design spiral

2.1.2 Geometrical constraints

To design the installation unit it has to comply with requirements and practical constraints. A number of these constraints are of a geometrical concern and they are listed in Table 2.1. An important parameter is the draft (loaded operation) of the installation unit because it is constrained by maximum water above the deck (9 m minus 0.5 m deck protection) of the transportation vessel. The width of the unit is constrained by the length of the deck of the transportation vessel. And the height of the unit is required to be at least equal to the water depth with an added amount of freeboard.

TABLE 2.1: Geometrical constraints

Unit dimensions	**Min**	**Max**
Width	-	70m
Height (50m water depth + 5m pit)	55m	-
Freeboard	4m	-
Draft (loaded operation)	-	8m
Clearance unit and T-class	0.5m	-

2.1.3 Stability constraints

The stability of the installation unit should always be guaranteed. This means in every operation stage and design condition, a minimum GM value providing a positive static stability. Also heel and trim in both intact and damage conditions are considered. The stability constraints are listed in Table 2.2, in which the angles are from DNV regulations [2].

Table 2.2: Stability constraints

	Min	**Max**
(intact) Heel/Trim angle	-	10-15°
(damaged) Heel/Trim angle	-	17°
GM (static stability)	1.5m	-

2.1.4 Turbine constraints

The wind turbine, especially the nacelle (top part), is a vulnerable piece of equipment. This leads to constraints to the motions the wind turbine can withstand. These constraints are listed in Table 2.3.

Table 2.3: Turbine constraints

	Min	**Max**
Nacelle acceleration	-	$3m/s^2$
Angle w.r.t. vertical	-	5°

2.1.5 Design conditions and limit states

Design conditions

Different modes of operation are characterized in terms of design conditions. Changes in the design conditions of the installation unit are accompanied by significant changes in draft, ballast, distance from adjacent vessels, etc. Limited variation of some of these parameters may be contained within a specific design condition, so the definition of design conditions is to some extent an arbitrary choice, arranged to cover all relevant combinations in a systematic and convenient way.
A typical set of design conditions is:

- Installation
- Operating
- Survival
- Transit
- Accidental
- Damaged

For each design condition a limited range of environmental conditions is specified. These limitations are clearly documented in the design analysis. The environmental conditions considered in the design are waves, wind, current and water depth.

Limit states

All relevant design criteria must be checked and satisfied for each design condition. The design criteria are expressed in terms of limit states. The limit states are:

- Ultimate Limit State (ULS) corresponding to the ultimate resistance for carrying loads
- Fatigue Limit State (FLS) related to the possibility of failure due to the effect of cyclic loading
- Accidental Limit State (ALS) corresponding to damage to components due to an accidental event or operational failure

Relevant design conditions and limit states

Within the concept design in this thesis not all design conditions are considered relevant. The main focus is on the operation of the installation unit so the installation and transit conditions are neglected. Furthermore not every combination of design condition and limit state is likely to occur and thus not considered relevant. All relevant combinations are listed in Table 2.4.

TABLE 2.4: Relevant design conditions and limit states

	Operating	*Survival*	*Accidental*	*Damaged*
ULS	x	x		
FLS	x	(x)		
ALS			x	x

2.2 Specifications initial design

Initial design impression

A 3D impression of the initial design of the unit is shown in Figure 2.2. The process of getting to this initial design is explained in the rest of this chapter. More detailed drawings including dimensions of the initial design are given in Figure B.1 in Appendix B.

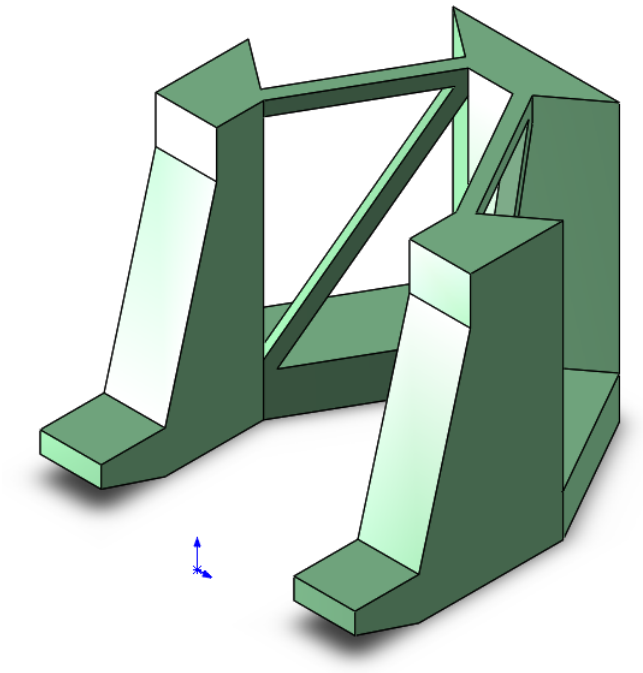

FIGURE 2.2: A 3D impression of the unit initial design

2.3 Initial sizing

2.3.1 Definition of motions

The six unit motions in the steadily translating system, as seen in Figure 2.3, are defined by three translations of the unit's center of gravity in the direction of the x-, y- and z-axis:

- surge in the longitudinal x-direction, positive forwards
- sway in the lateral y-direction, positive to port side
- heave in the vertical z-direction, positive upwards

And three rotations about these axes:

- roll about the x-axis, positive right turning
- pitch about the y-axis, positive right turning
- yaw about the z-axis, positive right turning

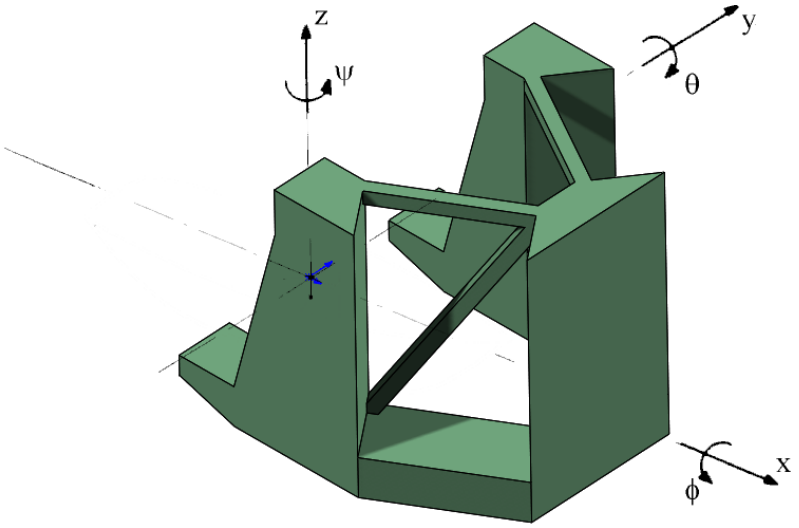

FIGURE 2.3: Definition of unit motions

2.3.2 Dimensions for hydrostatics

To design the unit a logical sequence of building the design is followed. First the floater part of the unit is given dimensions. Then the columns and the connections between the

columns are given dimensions. With these dimensions a design is found that complies with the geometrical constraints.

Foundation dimensions

The dimensions of the gravity based foundation of the wind turbine are specified in detail in Figure A.1 in Appendix A. The displacement of the foundation is taken into account in the calculations.

Floater

The floater fits around the foundation in a horseshoe like shape. The dimensions have to be large enough to make sure that the floater plus the turbine with foundation will float. This means a force balance between weight and buoyancy in equation (2.1).

$$mg = \rho_w \nabla g \tag{2.1}$$

with:

g	gravitational acceleration	[m/s^2]
m	mass	[kg]
ρ_w	density of seawater	[kg/m^3]
∇	submerged volume	[m^3]

An important restraint is the limited draft due to the workability draft of the transportation vessel. Since the floater part will submerge to relatively large water depth and has to resist wave loads on a large exposed area, it is assumed to have a structural density of 250 kg/m^3. The toes have a length such that the center of gravity of the unit loaded with foundation and turbine is (nearly) at the same location as the center of buoyancy.

Columns

There are three columns on top of the floater, one on the fore side and two on the aft. Each column consists of a base part and a top part. The columns have to pierce the water surface for stability and thus meet the height requirement which is the water depth and pit depth added. On top of that some freeboard is required which is set to 4 m. Furthermore they are placed close to the location of the foundation because the foundation will be connected to the columns. In the different draft stages, during the submerging of the foundation connected to the unit, there has to be stability. This leads

to a required minimum water plane area which consists of the length and width of the columns. Since the columns will submerge to relatively medium water depth and have to resist wave loads on a medium exposed area, they are assumed to have a structural density of 200 kg/m^3.

Column connections

The structural connections between the columns will give more overall strength to the structure and also provide walking space during the fully submerged stage. Since the connections will not submerge much and have to resist wave loads on a medium exposed area, they are assumed to have a structural density of 150 kg/m^3.

2.3.3 Motion estimations

Heave RAO

Heave is considered the governing motion when docking onto the transportation vessel. This is because of the large water plane area, which is needed for carrying the weight of the foundation and turbine, having a limited draft. To get an estimation of the heave motion of the unit the added mass and damping have to be calculated or assumed.
The added mass is calculated according to DNV [3]. This proceeds in equation (2.2).

$$m_A = \rho_w C_A A_R \tag{2.2}$$

with:

A_R	reference area	[m^2]
C_A	added mass coefficient	[-]
m_A	added mass per unit length	[kg/m]

In which:

$$A_R = \pi a^2 \tag{2.3}$$

with:

a	width	[m]

The unit is built from rectangle cross sections, the added mass coefficient is dependent on the aspect ratio of these rectangles. The associated values can be found in Figure 2.4 and Table 2.5.

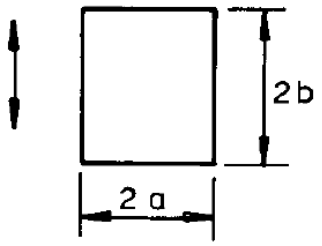

FIGURE 2.4: Aspect ratio for added mass

TABLE 2.5: Added mass coefficients

Aspect ratio (a/b)	**Added mass coefficient**
∞	1.0
10	1.14
5	1.21
2	1.36
1	1.51
0.5	1.70
0.2	1.98
0.1	2.23

The damping is estimated by assuming a value for the damping ratio, the damping over the critical damping. The value for the damping ratio is taken as 0.08.
The estimated heave RAOs for the initial design are given in Appendix B. One RAO for the unloaded unit and one for the loaded unit.

2.4 Stability and static loads

2.4.1 Definition of load cases

The static stability has to comply with the constraint given in Table 2.2. The stability is checked for different load cases. The cases are with or without the load of the foundation and turbine. And during the submerging of the unit, three different water plane areas can be distinguished. This gives the following load cases:

- Unloaded draft
- Loaded draft (floater)
- Loaded draft (column base)
- Loaded draft (column top)

Unloaded draft

The unloaded draft is considered the unit without the gravity based wind turbine. If the unit is in operation the unloaded draft is at floater draft. If the unit is in survival then the unloaded draft will be at column base or column top draft by adding water ballast. The reason is to minimize the water plane area and thereby reducing fatigue damage. This thesis is about the operation of the installation unit, thus the unloaded draft is considered at floater draft.

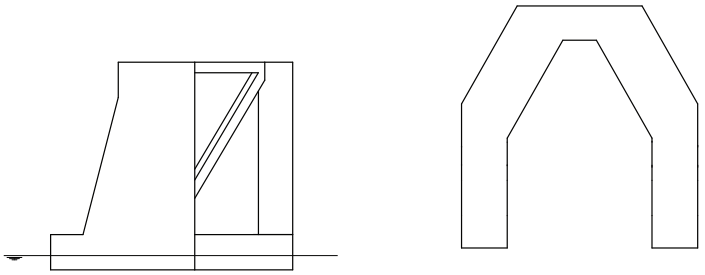

FIGURE 2.5: Unloaded floater draft

Loaded draft (floater)

The loaded draft consists of three stages. The first one is the loaded draft at floater draft. This load case is an important and critical case in the operation. Because it is the case during docking and float off. The water plane area of the foundation is not taken into account in the stability calculation. However the displacement of the foundation is taken into account in the buoyancy.

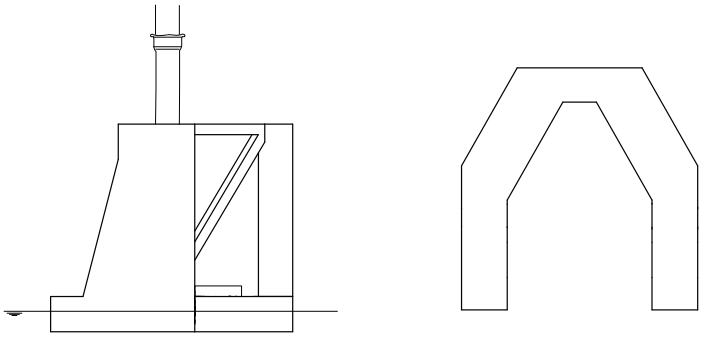

FIGURE 2.6: Loaded floater draft

Loaded draft (column base)

By adding water ballast the loaded floater draft reaches the loaded column base draft. The water plane area will decrease significantly and this will result in a change in stability.

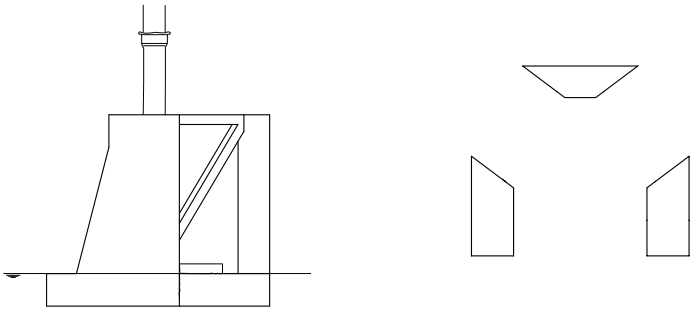

FIGURE 2.7: Loaded column base draft

Loaded draft (column top)

By adding even more water ballast the loaded column base draft reaches the loaded column top draft. The water plane area will again decrease significantly and this will result in a change in stability. In this case the center of buoyancy is moving further away with respect to the center of gravity in x-direction due to changes in submerged volume shapes. This causes a large moment on the unit, not just because of the increase in lever-arm but also an increase in weight.

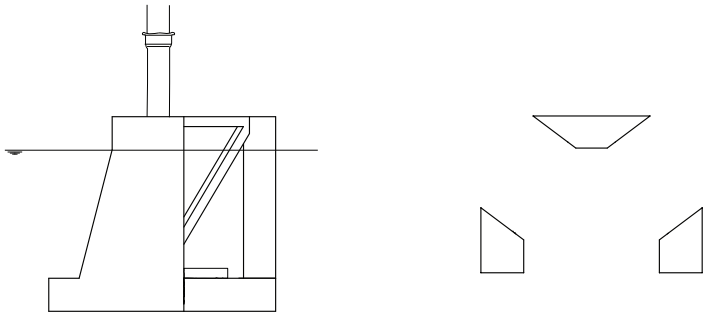

FIGURE 2.8: Loaded column top draft

2.4.2 Wind load

An important load on the unit is the wind load. The wind load causes a static and dynamic load on the unit. In this thesis only the static part of the load will be determined. The static wind load causes the unit to heel and/or trim, depending on the wind direction. The design wind velocity is 36 m/s, the wind in the calculation is considered coming from starboard or head wind. The static wind load can be calculated according to equation (2.4) from DNV regulations [3].

$$F_w = 0.5 C_s C_h \rho_a v_w^2 A \tag{2.4}$$

with:

A	(exposed) area	[m^2]
C_h	height coefficient	–
C_s	shape coefficient	–
F_w	wind load	[N]
v_w	design wind speed	[m/s]
ρ_a	density of air	[kg/m^3]

2.4.3 Intact stability

The static stability is calculated according J.M.J. Journee and W.W. Massie [4].
It is calculated in transverse and longitudinal direction.

$$GM_T = KB + BM_T - KG \tag{2.5}$$

$$GM_L = KB + BM_L - KG \tag{2.6}$$

with:

BM	distance from center of buoyancy to metacenter	[m]
GM	distance from center of gravity to metacenter	[m]
KB	distance from keel to center of buoyancy	[m]
KG	distance from keel to center of gravity	[m]

The distance between the keel and the center of buoyancy is calculated as the sum of submerged volumes times the distance to the center of the associated volume divided by the total submerged volume, see equation (2.7).

$$KB = \frac{\sum \nabla_i z_i}{\nabla} \tag{2.7}$$

The distance between the center of buoyancy and metacenter is calculated as the moment of inertia of the water plane area divided by the submerged volume. The moment of inertia is calculated for both transverse (equation (2.8)) and longitudinal (equation (2.9)) direction.

$$BM_T = \frac{I_T}{\nabla} \tag{2.8}$$

$$BM_L = \frac{I_L}{\nabla} \tag{2.9}$$

with:

I_T	inertia of water plane in transverse direction	[m^4]
I_L	inertia of water plane in longitudinal direction	[m^4]

The distance between the keel and the center of gravity is calculated as the sum of masses times the distance to the center of gravity of the associated mass divided by the total mass, see equation (2.10). The center of gravity of the foundation and turbine is specified in Appendix A.

$$KG = \frac{\sum m_i z_i}{m} \tag{2.10}$$

2.4.4 Static heel/trim

Due to a misalignment between the center of gravity and center of buoyancy, during the different load cases, there will be a trim angle (equation (2.11)). There will be no heel angle because of longitudinal symmetry.

$$\theta = \sin^{-1} \frac{M_y}{\rho_w g \nabla G M_T} \tag{2.11}$$

with:

M_y	moment on transverse axis	[Nm]
θ	static trim angle	[°]

The static wind load causes a heeling and/or trimming moment, using the associated GM value, on the structure according to equations (2.12) and (2.13).

$$\phi_w = \sin^{-1} \frac{M_w}{\rho_w g \nabla G M_L} \tag{2.12}$$

with:

M_w	moment due to wind load	[Nm]
ϕ_w	static heel angle due to wind load	[°]

$$\theta_w = \sin^{-1} \frac{M_w}{\rho_w g \nabla G M_T} \tag{2.13}$$

with:

θ_w static trim angle due to wind load [°]

2.4.5 Damaged stability

After a collision, explosion or another cause of damage the unit will be in a new load case. The new load case is caused by flooding of one or two compartments of the unit. Which will make the unit heel/trim and perhaps induce instability.
The damage will be assessed for one case. This is the case in which the end of the toes of the floater collide with the T-class or a tugboat. Two damage situations are now possible, one of the toes or both toes will be flooded. The reason for choosing this damage case is that the compartments in this area of the unit are expected to be the largest and at the same time this is furthest from the center of gravity of the unit. It follows that flooding of this area will cause the largest possible bending moment from a damage case on the unit.

Damage definition

In the DNV regulations [2] the extent of damage to a column stabilized unit and deep draft floating installations is defined. The horizontal penetration depth of the design damage is to be taken as 1.5 m. Furthermore columns and braces shall be assumed flooded by damage having a vertical extent of 3 m occurring at any level between 5 m above and 3 m below the draft of the load cases. No vertical bulkhead shall be assumed damaged, except where bulkheads are spaced closer than a distance of one eighth of the column perimeter at the draft under consideration.

Bulkhead locations

A first estimate of the compartments is made by positioning the bulkheads. The bulkheads are important in the overall strength of the unit as well. This means the bulkheads have to comply with some common sense from structural point of view. For example the vertical transverse bulkheads in the toes of the unit will be extended from the column above.

2.4.6 Accidental events

During operation all kinds of accidental events can occur. Human errors like forgetting to close a valve. But also equipment failures like failure of the lifting tools causing increased motion of the load or even a drop of the load.

2.5 Initial seakeeping analysis

2.5.1 Strip theory

The unit is considered to be a rigid body, floating in the surface of an ideal fluid, which is homogeneous, incompressible, free of surface tension, irrotational and without viscosity. It is assumed that the problem of the motions of this floating body in waves is linear or can be linearised. Consequently, only the external loads on the underwater part of the unit are considered here and the effect of the above water part will be fully neglected.
The strip theory solves the three-dimensional problem of the hydromechanical and exciting wave forces and moments on the unit by integrating the two-dimensional potential solutions over the unit's length. Interactions between the cross sections are ignored for the zero-speed case. So, each cross section of the unit is considered to be part of an infinitely long cylinder. The strip theory is a slender body theory, so one should expect less accurate predictions for ships with low length to breadth ratios.
The strip theory is based on the potential flow theory. This holds that viscous effects are neglected, which can deliver serious problems when predicting roll motions at resonance frequencies. In practice, for viscous roll damping effects can be accounted fairly by empirical methods.
Furthermore the strip theory is based on linearity. This means that the unit motions are supposed to be small, relative to the cross sectional dimensions of the unit. Only hydrodynamic effects of the hull below the still water level are accounted for. So, when parts of the unit go out of or in to the water or when green water is shipped, inaccuracies can be expected. Also, the theory does not distinguish between alternative above water hull forms. Because the added resistance of a ship due to the waves is proportional to the relative motions squared, its inaccuracy will be gained strongly by inaccuracies in the predicted motions.
As can be read in Theoretical Manual of SEAWAY [5].

2.5.2 Software input

The hull shape is defined for the unloaded and loaded case both at floater draft in 11 cross sections. In the loaded case the foundation is seen as part of the installation unit. With the dimensions given in Appendix B. The mass radius of gyration about the x-axis is calculated as given in equation 2.14. This is also done for the mass radii about the y-axis and z-axis.

$$k_{xx} = \sqrt{\frac{I_{xx}}{m}} \tag{2.14}$$

with:

I_{xx}	mass moment of inertia	[kgm^2]
k_{xx}	radius of gyration about x-axis	[m]

If the unit is modeled as equivalent blocks then the mass moments of inertia can be calculated as:

$$I_{xx} = \sum m_i(y_i^2 + z_i^2) \tag{2.15}$$

$$I_{yy} = \sum m_i(x_i^2 + z_i^2) \tag{2.16}$$

$$I_{zz} = \sum m_i(x_i^2 + y_i^2) \tag{2.17}$$

The forward speed of the unit is taken as 0. The frequency range is taken from 0.05 rad/s to 2.5 rad/s in steps of 0.0125. For the wave directions the input is in steps of 15 degrees all the way around. As for the sea states the JONSWAP spectrum is considered with a significant wave height (Hs) of 3 m and periods from 3.5 s to 17.5 s in steps of 1. The roll damping as frequency dependent potential damping.

2.5.3 Motion characteristics

The displacements and accelerations for multiple sea states and the governing wave direction (90°) are calculated for the loaded unit. The wave direction is 90°because during float off this will be the case. This is done for certain points on the hull of the unit and wind turbine. These point are located at the bottom of the outside ends of the toes and at the bottom of the floater at the location where the sloped end starts. For the accelerations the nacelle of the wind turbine is taken as a point.
The natural periods for the loaded case are:

- Heave period: 9.86 s
- Roll period: 13.62 s

- Pitch period: 21.65 s

2.5.4 Workability

In Figure 2.9 the workability with regard to the displacements and accelerations is shown for the governing point. It is determined with a clearance between the unit and the transportation vessel of 0.5 m and a 3 hour extreme. The clearance is the submerged deck minus the loaded draft of the unit but also minus 0.5 m of fendering.

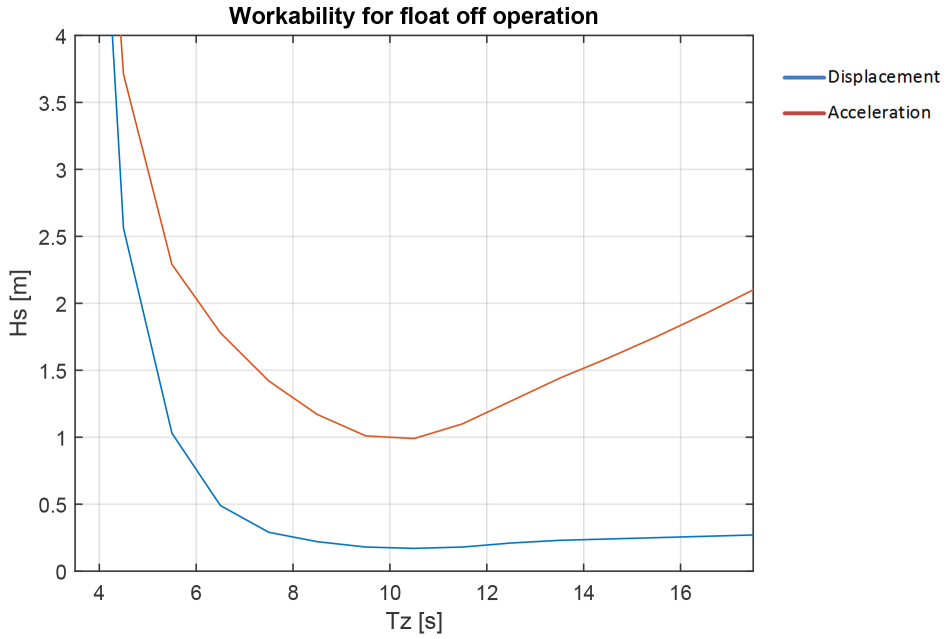

FIGURE 2.9: Workability for float off operation

Chapter 3

Preliminary installation unit

In this chapter the process from initial design to preliminary design is given. The different structural loads acting on the installation unit are defined. The pressures and inertial loads from a hydrodynamic diffraction are translated to the global FEM model. Analysis of the stresses leads to improvements in the structural design which will give a preliminary design. The stress ranges in the preliminary design will be used for the fatigue analyses.

3.1 Structural load definition

3.1.1 Structural loads

There are multiple loads acting on the structure during operation of the unit. Each of these loads contribute to the global stress in the structure. By knowing this stress the structural elements can be defined: bulkheads, girders, stiffeners, etc. This will lead to the strength of the unit and gives more detailed information about the mass distribution. The main structural loads are:

- Live & Dead loads
  - Weight of the structure
  - Weight of GBF & Wind turbine
  - Water ballast
- Environmental loads
  - Wave load

  - Current load
  - Wind load
  - Lateral pressure
- Impact loads

Each of these structural loads is defined and is assigned to design condition(s) and limit state(s) listed in Table 2.4.

3.1.2 Live & Dead loads

Dead load

The dead load includes loads that are relatively constant over time. It consists of the weight of the structure itself. The weight of the columns acts on the floater of the unit which causes shear forces. To significantly reduce shear stresses in the floater, bulkheads will be located in the extension of the columns. The dead load is relevant for the ultimate limit state in operating and survival condition.

Live load

Live loads are temporary, of short duration, or a moving load. Live loads include all the forces that are variable within the object's normal operation cycle not including construction or environmental loads.
The gravity base foundation (GBF) and wind turbine hanging from the columns of the installation unit is considered a live load. The weight of the foundation and wind turbine will cause both a shear force and bending moment on the columns. Furthermore the GBF and wind turbine can move independently of the installation unit which causes dynamic loads like vibrations or even impact.
The water ballast within the installation unit and foundation is also considered a live load. The ballast is distributed over several compartments, the water is able to slosh causing a dynamic load on top of the static weight load of the ballast. The static weight load causes a shear force and bending moment on the floater.
The live loads are relevant for the ultimate limit state in operating and survival condition. They may also be relevant for the fatigue limit state in operating condition, depending on the structural stress range and the frequency of the loads.

3.1.3 Environmental loads

Wave load

The wave load depends on the wave energy spectrum, sea state, wave direction, hull shape and relative velocity. The wave energy spectrum is chosen according to a certain operating location of the installation unit. The sea state consists of a significant wave height and wave period. The wave direction can be from 0°to 360°, but since the hull shape is symmetrical in the longitudinal axis only 0°to 180°have to be considered.
Multiple combinations of sea state and wave direction have to be checked to meet the workability requirements and find the 'worst-case' regarding structural stress due to the wave load.
Wave loads are relevant for the ultimate and fatigue limit state in operating and survival condition.

Current load

The current load is calculated according to the Morison equation (3.1). In an oscillatory flow with flow velocity u(t), the Morison equation gives the inline force parallel to the flow direction.

$$F_c = \rho_w V \frac{du}{dt} + \rho_w V (C_m - 1)(\frac{du}{dt} - \frac{dv}{dt}) + 0.5\rho_w A C_d (u - v)|u - v| \tag{3.1}$$

with:

C_d	drag coefficient	[-]
C_m	inertia coefficient	[-]
F_c	current load	[N]
u	current velocity	[m/s]
V	volume	[m^3]
v	vessel velocity	[m/s]

The first two terms in the equation are inertia forces and the last term is the drag force. The first term in the equation is the Froude-Krylov force and the second term is the hydrodynamic mass force. The contribution of vortex induced vibrations is not considered significant because there are not much slender members within the structure. Current loads are relevant for the ultimate limit state in operating and survival condition.

Wind load

The static wind load is already described in Chapter 2. The dynamic wind load is of less importance. Also for the wind load the contribution of vortex induced vibrations is not considered significant because there are not much slender members within the structure. Wind loads are relevant for the ultimate limit state in operating and survival condition.

Lateral pressure

The lateral pressure on the unit is caused by the water pressure due to the water depth. Since the unit will submerge to 55 m water depth, the maximum lateral pressure will be around 5.5 bar. This will have an effect on the outer plating of the unit, especially at the floater and lower sides of the columns.
The lateral pressure is relevant for the ultimate limit state in operating condition.

3.1.4 Impact loads

An impact load is a high force applied over a short time period when two or more bodies collide. The effect on the structure depends critically on the relative velocity of the bodies to one another. Examples of impact loads are collisions between the unit and transportation vessel (damage case in Chapter 2) or a collision between the unit and wind turbine. Impact loads are relevant for damaged condition in the accidental limit state. And depending on the design requirements, impact loads can also be relevant for operating condition in the ultimate limit state.

3.2 Structural members

3.2.1 Floater

The primary structural members are bulkheads, transverse frames and longitudinal stiffeners. The bulkheads are taken as the same thickness as the outer plating of the unit. The transverse frames are T-profiles and the longitudinal stiffeners are bulb profiles. The initial dimensions of the structural members are calculated according to the Offshore Standard by DNV for structural design of offshore units [6].
The thickness of plating subject to lateral pressure with respect to yield is given by equation (3.2).

$$t = 15.8 \frac{k_a s \sqrt{p}}{\sqrt{\sigma_{pl} k_{pp}}} \tag{3.2}$$

with:

k_a	correction factor for aspect ratio of plate field	[-]
k_{pp}	fixation parameter for plate	[-]
p	(lateral) pressure	[kN/m^2]
s	stiffener spacing	[m]
t	plate thickness	[mm]
σ_{pl}	permissible bending stress	[MPa]

The lateral pressure will be the hydrostatic water pressure. The stiffener spacing will be 0.3 m, to keep the longitudinal stiffeners continuous throughout the structure this spacing may vary around 0.3 m. The correction factor for aspect ratio of plate field is 1.0 and the fixation parameter for plate is 0.9. The permissible bending stress depends on the minimum yield stress and the equivalent stress for global in-plane membrane stress.

The section modulus for the transverse frames and longitudinal stiffeners subjected to lateral pressure with respect to yield are given by equation (3.3).

$$Z_s = \frac{l^2 sp}{k_m \sigma_{pl} k_{ps}} 10^6 \tag{3.3}$$

with:

k_m	bending moment factor	[-]
k_{ps}	fixation parameter for stiffeners	[-]
l	frame/stiffener span	[m]
Z_s	section modulus	[mm^3]

The stiffener span, or frame spacing, will be 0.9 m, to have the transverse frames evenly distributed between the bulkheads this value can vary around 0.9 m. For the initial structural members the dimensions given in Figure 3.2 are used.

3.2.2 Columns

For the columns the initial structural members consist of bulkheads and transverse frames. The bulkheads are the same thickness as the outer plating, as in the floater. Also the transverse frames have the same dimensions and spacing as in the floater. There are no longitudinal stiffeners in the columns to save on weight, which leads to lower costs and more stability.

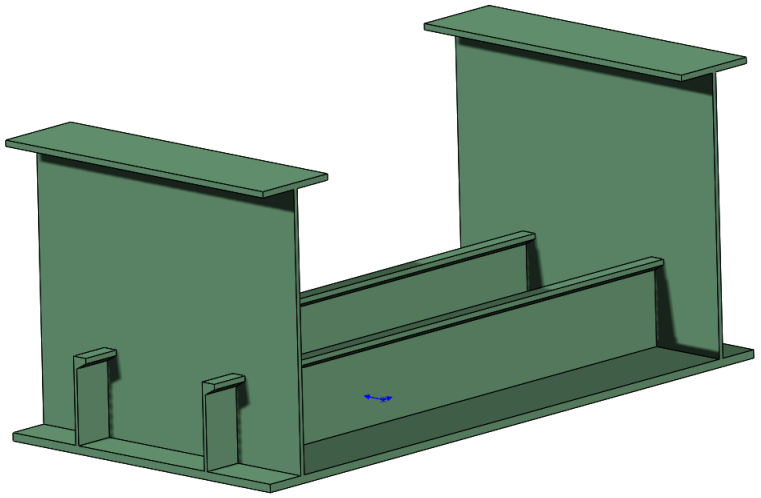

FIGURE 3.1: 3D impression of initial stiffened plate

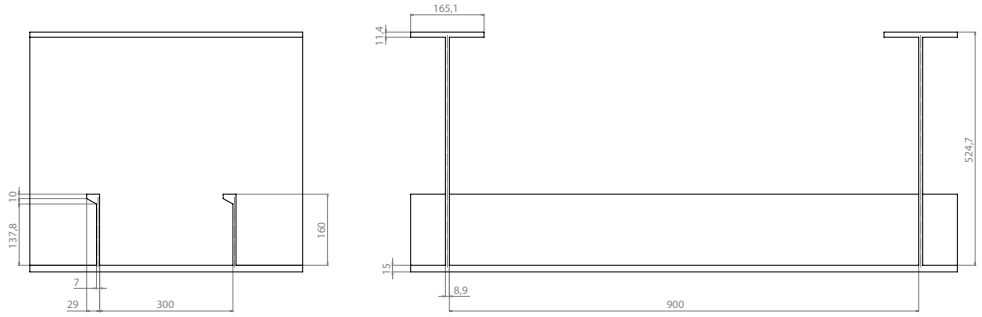

FIGURE 3.2: Dimensions of initial structural members

3.2.3 Braces

The braces are square thin walled connections between the columns, both in horizontal and diagonal direction. The outer dimensions of the braces are 3x3 m with a plate thickness of 15 mm. The braces are expected to take quite some loads and therefor it is expected that are likely to be hot spots in the fatigue analysis.

3.3 Flow diagram: From design to stress RAOs

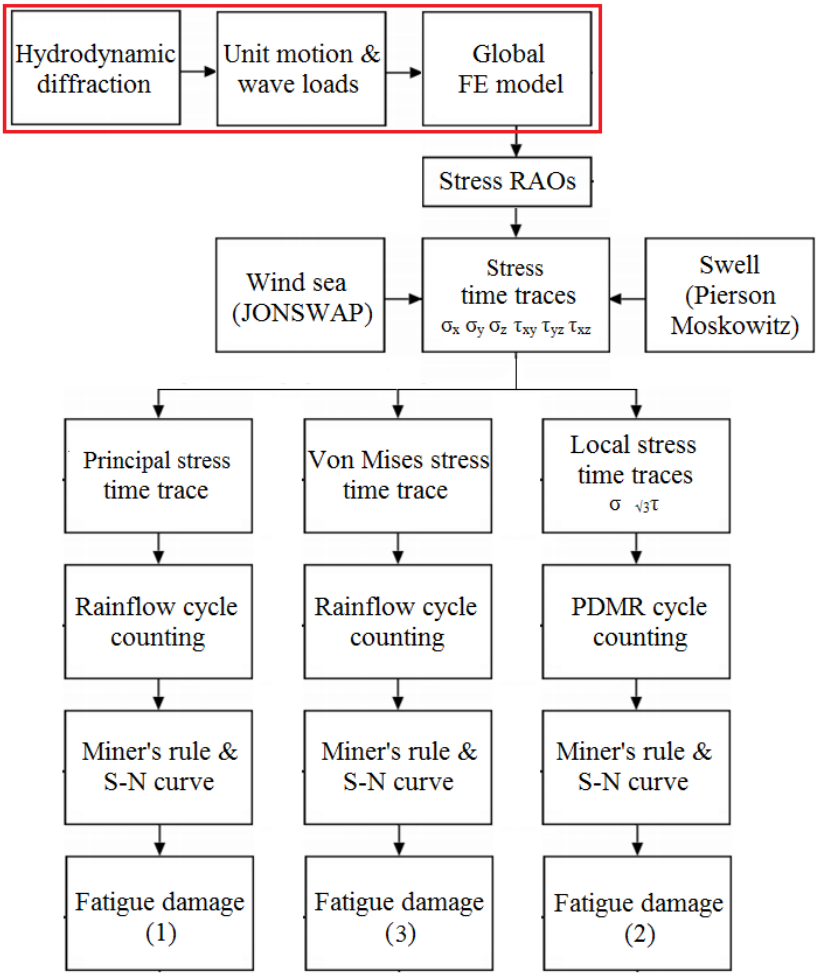

FIGURE 3.3: Flow diagram: From design to stress RAOs

3.4 Hydrodynamic diffraction

3.4.1 Diffraction theory

A hydrodynamic diffraction analysis, performed by the Ansys Aqwa program, gives the wave loads and motion responses of the unit in waves, including their hydrodynamic interaction. The hydrodynamic diffraction is based on a three-dimensional source distribution technique for the solution of the linearised velocity potential problem. For this approach the fluid is assumed to be inviscid, homogeneous, irrotational and incompressible. It computes fluid pressures and wave loads on the basis of the velocity potential around the unit. For the computations, the mean wetted part of the hull of the unit is approximated by a number of plane elements. Each element represents a distribution

of source singularities, each of which contributes to the velocity potential describing the fluid flow.

3.4.2 Software input

The diffraction analysis is done for a chosen frequency range, significant wave height and for multiple wave directions. With the pressure distribution on the hull due to the wave loads, a global structural model can be loaded and the required structural members of the unit can be determined.
The input for Ansys Aqwa is given in table 3.1.

TABLE 3.1: Ansys Aqwa input for hydrodynamic diffraction

Parameter	**Value or range (step size)**
Draft	4.9 m
Frequency range	0.05-2 rad/s (0.05)
Significant wave height	2.0 m
Wave directions	0-360°(15)
Water depth	1000 m
Mass	10,440 t
Center of gravity	
x	39.6 m
y	0 m
z	21.8 m
Radius of gyration	
k_{xx}	29.4 m
k_{yy}	26.9 m
k_{zz}	30.4 m

3.4.3 Diffraction output

The diffraction analysis output consists of pressures on the wetted hull and the motions of the unit. The motions can be compared to the motions collected from the strip theory computation. The pressures on the hull and the inertia forces due to the motions can be transferred to the global FEM model.

RAOs

The RAOs of heave, roll and pitch for 90°beam waves obtained from the diffraction analysis are shown in Figure 3.4. These RAOs are considered governing because these

motions contribute to the vertical motion. The vertical motion is important when the unit is docking the transportation vessel to pick up the gravity based wind turbine.

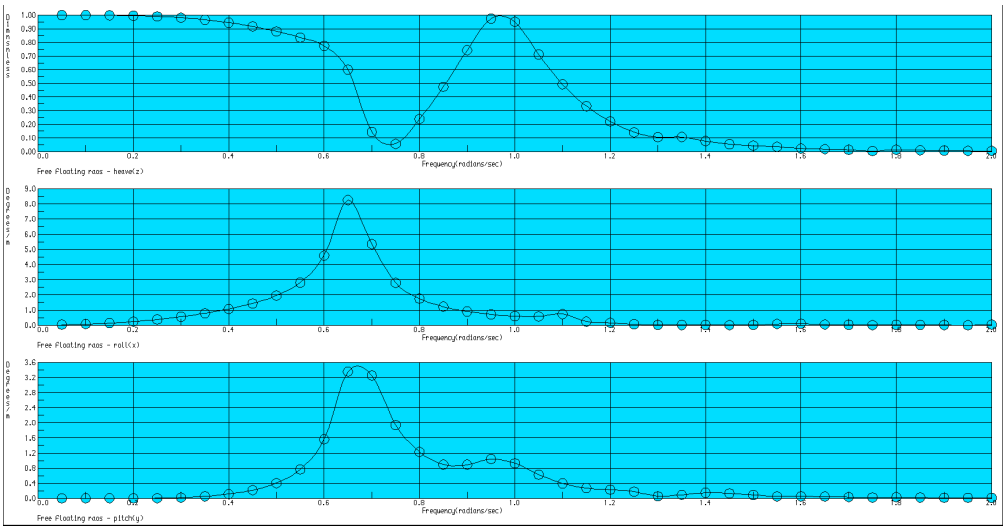

FIGURE 3.4: Heave, pitch and roll RAOs from diffraction analysis

Pressures and motions

In Figure 3.5 the pressure contours on the wetted hull of the unit are shown. This figure shows the pressure contours for head waves and beam waves as examples. The red contours show relatively high pressures and the blue contours the lower pressures. From these pressure contours a first insight into the wave loading on the unit can be seen.

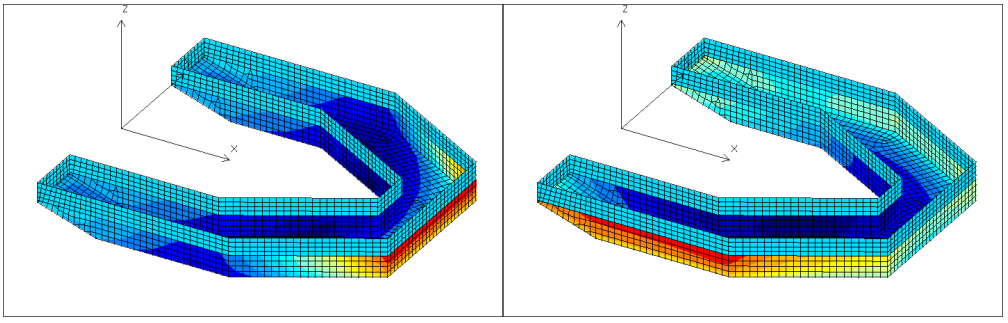

FIGURE 3.5: The pressure contours on the wetted hull for head and beam waves

3.5 Global FEM model

To perform a global hull analysis a FEM model is created. This model is simplified because the objective of the global hull analysis is to find the spots in the structure where fatigue is critical. As stated in Chapter 1 the element size is relatively large for

a fatigue analysis. But because it is a qualitative comparison between different fatigue analyses the element size is considered sufficient.
The FEM model consists of shell elements only, this means the frames and stiffeners are modeled as equivalent plates. The cross section area of the stiffeners on a plate is added to the cross section area of that plate. This gives a plate thickness of 19.7 mm for the outer plating and bulkheads. The frames are modeled as 'open' bulkheads in which the area of the T-frames is kept equivalent to a plate. This gives a plate thickness of 12.9 mm for a frame height of 0.5 m. In Figures 3.6 and 3.7 the FEM model and a section in the structure is shown. The material used for the global FEM model is structural steel with an elastic modulus of 210 GPa and a Poisson ratio of 0.3.

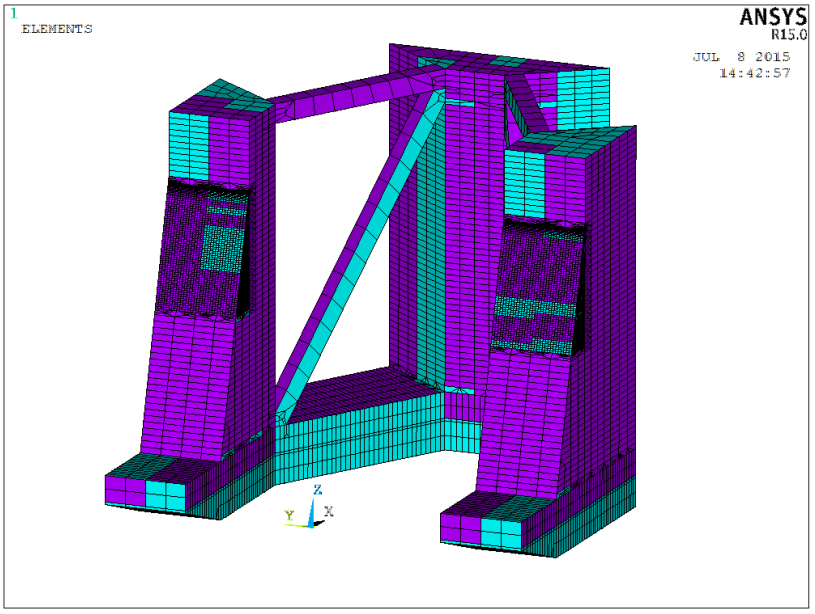

FIGURE 3.6: Global FEM model

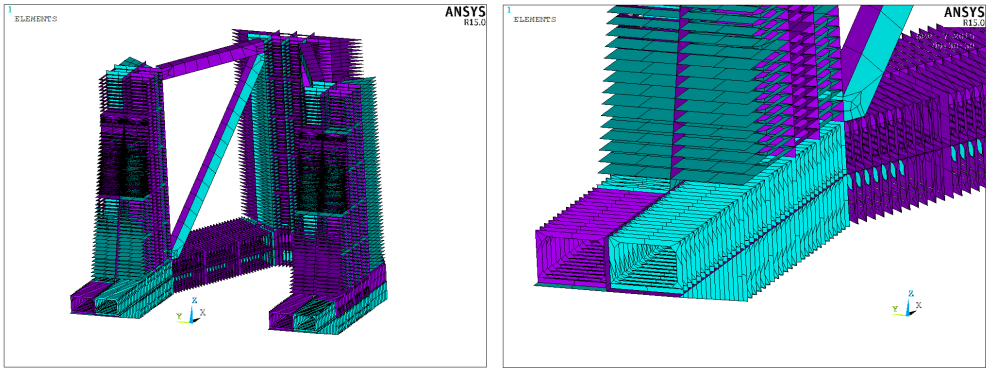

FIGURE 3.7: Inside structure of global FEM model

3.6 Model validation

Before translating the wave loads on the FEM model, the model is validated. First the mass properties of the diffraction model are compared to the mass properties of the FEM model in Table 3.2. Then two cases are done to check the model. The model is constrained by 4 nodes with all degrees of freedom equal to zero as shown in Figure 3.8. The first case is done by only applying gravity on the model and check if the reaction forces in the nodes are equal to the weight of the structure. The second case is done by applying the hydrostatic load case and check if the reaction forces in the nodes are in equilibrium or close to equilibrium.

TABLE 3.2: Mass properties of diffraction and global FEM model

	Diffraction model	**Global FEM model**
Mass	10,439 t	10,411 t
k_{xx}	29.4 m	29.2 m
k_{yy}	26.9 m	26.7 m
k_{zz}	30.4 m	30.2 m

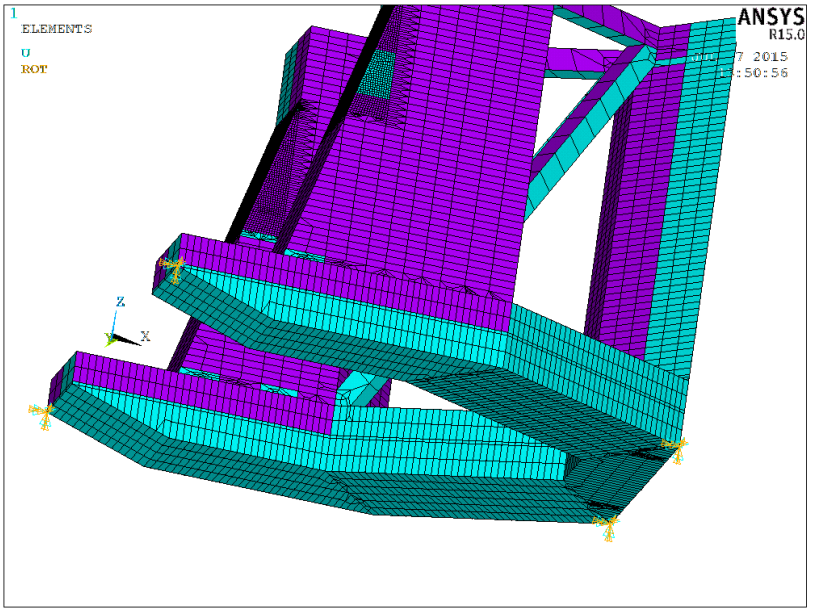

FIGURE 3.8: Constraints for validating the global FEM model

```
PRINT F    REACTION SOLUTIONS PER NODE

 ***** POST1 TOTAL REACTION SOLUTION LISTING *****

 LOAD STEP=     1  SUBSTEP=     1
  TIME=    1.0000      LOAD CASE=   0

 THE FOLLOWING X,Y,Z SOLUTIONS ARE IN THE GLOBAL COORDINATE SYSTEM

   NODE      FX          FY          FZ
  38115 -0.10406E+08-0.28526E+07-0.20340E+08
  38192  0.10397E+08-0.62603E+07-0.30945E+08
  38246  0.10398E+08 0.62680E+07-0.30941E+08
  38707 -0.10390E+08 0.28449E+07-0.20333E+08

TOTAL VALUES
VALUE  -0.96280E-01 0.35549E-05-0.10256E+09
```

FIGURE 3.9: Reaction forces in the nodes for gravity load

As can be seen in Figure 3.9 the sum of reaction forces on the nodes in x- and y-direction are small. The sum of the reaction forces in z-direction are about equal to the mass of the global FEM model multiplied with the gravitational acceleration.

```
PRINT F    REACTION SOLUTIONS PER NODE

 ***** POST1 TOTAL REACTION SOLUTION LISTING *****

 LOAD STEP=     1  SUBSTEP=     1
  TIME=    1.0000      LOAD CASE=   0

 THE FOLLOWING X,Y,Z SOLUTIONS ARE IN THE GLOBAL COORDINATE SYSTEM

   NODE      FX          FY          FZ
  38115 -0.86700E+06-0.21658E+06  44464.
  38192  0.87266E+06 0.48878E+06 -57425.
  38246  0.86011E+06-0.49133E+06 -67677.
  38707 -0.86608E+06 0.22056E+06  45111.

TOTAL VALUES
VALUE   -316.54      1424.8     -35527.
```

FIGURE 3.10: Reaction forces in the nodes for hydrostatic load

As can be seen in Figure 3.10 the sum of reaction forces on the nodes in x- and y-direction are small compared to the individual forces on each node. The sum of the reaction forces in z-direction are small compared to the mass of the global FEM model multiplied with the gravitational acceleration. This means that the model is close to equilibrium and considered validated good enough for its purpose.

3.7 Model constraints

To prevent the global FEM model from rigid body motion constraints have to be added. The actual purpose of the constraints is to counteract the sum of the remaining reaction forces after putting a wave load on the model. The constraints are modeled as springs on the nodes of the wetted surface elements. One end of each spring is attached to a node on the hull below the waterline and the other end is connected to a fixed point as can be seen in Figure 3.11. The stiffness of the springs is defined by equation (3.4). The most common element area below the waterline is 0.9 x 2.25 = 2.025 m^2 which leads to a spring stiffness of k = 20.4 kN/m.

$$k = A_w \rho_w g \tag{3.4}$$

with:

A_w	area of wetted element	[m^2]
k	spring stiffness	[N/m]

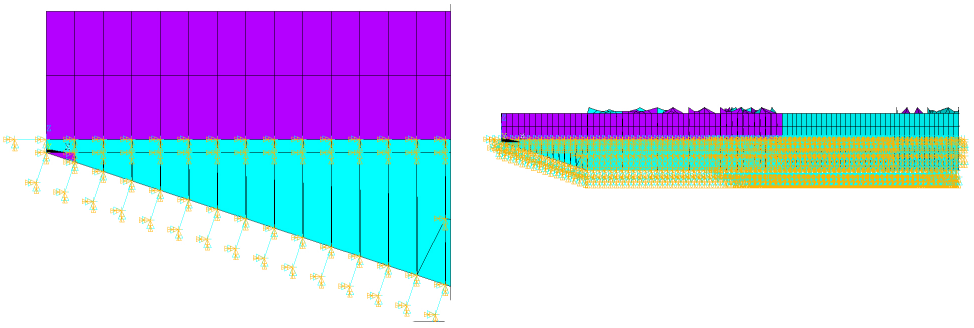

FIGURE 3.11: Side view of springs on nodes below the waterline

By putting the pressure and inertia loading from the diffraction on the global FEM model, stresses in the structure can be observed with a stress contour plot. An example of such a stress contour plot is shown in Figure 3.12.

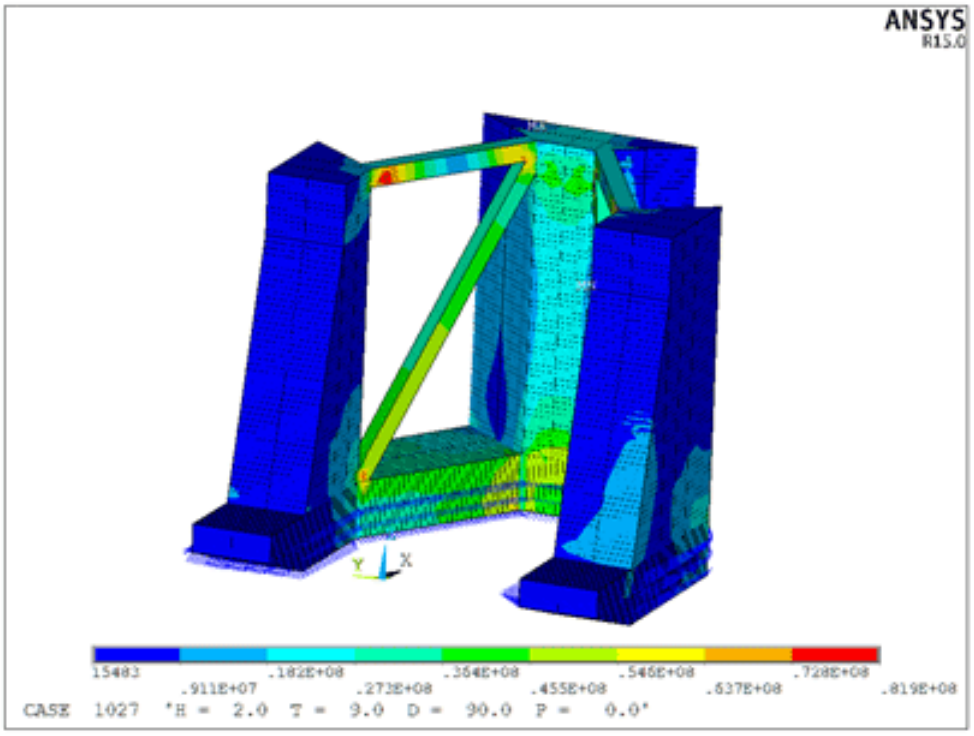

FIGURE 3.12: Example of stress contours within the structure

Chapter 4

Theory on fatigue

In this chapter an introduction to stresses and fatigue for metallic structures is given. And the relevant background theory for uniaxial and multiaxial fatigue is briefly described.

4.1 Stress transformation and equivalent stress

A point in a solid body subjected to a general three-dimensional state of stress has a normal stress and two shear stress components acting on each face. It is possible to determine the unique orientation of an element having only principal stresses acting on its faces. These principal stresses are assumed to have magnitudes of maximum, intermediate and minimum value; $\sigma_{max} \geq \sigma_{int} \geq \sigma_{min}$ [7]. In this thesis only plate elements are used, so a 2D analysis of the principal stresses is sufficient. The angle of the maximum and minimum principal stresses with respect to the original axis can be calculated by differentiating with respect to θ, which leads to equations (4.1 and 4.2).

$$\tan 2\theta_{p1} = \frac{2\tau_{xy}}{\sigma_x - \sigma_y} \tag{4.1}$$

$$\theta_{p2} = \theta_{p1} + 90 \tag{4.2}$$

with:

θ_{p1}	angle between σ_x and σ_{p1}	[deg]
θ_{p2}	angle between σ_y and σ_{p1}	[deg]
σ_x	normal stress in x-direction	[MPa]
σ_y	normal stress in y-direction	[MPa]
τ_{xy}	shear stress in xy-plane	[MPa]

The magnitude of these principal stresses can then be determined by equation (4.3).

$$\sigma_{1,2} = \frac{\sigma_x + \sigma_y}{2} \pm \sqrt{\left(\frac{\sigma_x - \sigma_y}{2}\right)^2 + \tau_{xy}^2} \tag{4.3}$$

with:

σ_1	principal stress 1	[MPa]
σ_2	principal stress 2	[MPa]

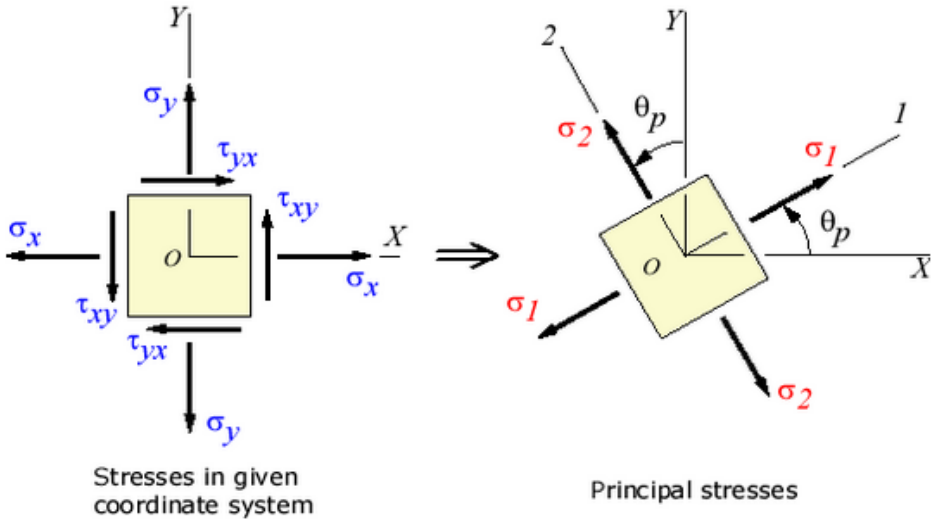

FIGURE 4.1: Principal stress directions

By knowing the principal stresses it is possible to determine the absolute maximum shear stress according to the Mohr's circle.
If the principal stresses have the same sign the absolute maximum shear is equal to:

$$\tau_{abs} = \frac{\sigma_{max}}{2} \tag{4.4}$$

If the principal stresses have opposite signs the absolute maximum shear is equal to:

$$\tau_{abs} = \frac{\sigma_{max} - \sigma_{min}}{2} \tag{4.5}$$

A three-dimensional state of stress can be written as an equivalent stress. This can be done according to a distortion energy theory, which states that the actual distortion energy should be less than the distortion energy in a simple tension case. In this case distortion is the change of shape without changing the volume.
The distortion energy per unit volume for a general three-dimensional case is given in

terms of principal stress values as:

$$u_d = \frac{1+\nu}{3E}[\frac{(\sigma_1-\sigma_2)^2+(\sigma_2-\sigma_3)^2+(\sigma_3-\sigma_1)^2}{2}] \tag{4.6}$$

with:

E	Young's modulus	[MPa]
u_d	Distortion energy per unit volume	$[J/m^3]$
ν	Poisson's ratio	-

Distortion energy for a simple tension case at the time of yielding is given as:

$$u_{d,s} = \frac{1+\nu}{3E}\sigma_y^2 \tag{4.7}$$

The stress terms in equation (4.6) are the basis for an equivalent stress, the Von Mises stress. This stress is used to compare the Von Mises stress in a FEM model with the yield stress of the material. It can also used in fatigue analysis to simplify the three-dimensional stress states. The Von Mises stress can be rewritten as:

$$\sigma_{VM} = \sqrt{\sigma_{xx}^2+\sigma_{yy}^2+\sigma_{zz}^2-\sigma_{xx}\sigma_{yy}-\sigma_{yy}\sigma_{zz}-\sigma_{zz}\sigma_{xx}+3(\tau_{xy}^2+\tau_{yz}^2+\tau_{zx}^2)} \tag{4.8}$$

4.2 Background fatigue theory

Metal structures exhibit damage by fatigue when subjected to repeated cyclic loading. The magnitude of stress in each cycle is normally not sufficient to cause rupture with a single cycle. A (large) number of cycles is therefore needed for rupture. The initiation or nucleation of a crack is followed by its growth until the critical crack size of the parent metal under the operating load is reached leading to rupture. Multiple cracks can nucleate during cyclic load. The fatigue crack nucleates and grows at stresses below the tensile strength of the metal. The crack advances continuously, its growth rate is dependent on the magnitude of the load and the geometry of the component. Also the nucleated crack may not grow at all or may propagate extremely slow resulting in high fatigue life of the component if the applied stress is less than the metal fatigue limit.
The fatigue domain is complicated, since there are quite some factors that influence the fatigue life of a structure. At first the structure is of importance, the relevant properties are listed here.

- Material (structural steel, aluminum, etc.)
- Geometry

- Welded joints (notches and heat-affected zones)
- Residual stresses
- Initial defects

Furthermore, the type of cyclic loading is of interest.

- Constant or varying amplitude
- Constant or fluctuating mean stress
- Uniaxial or multiaxial stress state
- Proportional multiaxial or non-proportional multiaxial

And finally the theory used to calculate the fatigue life determines a significant part of the outcome. As the theory is dependent on the structure and the loading it is important to apply the correct associated method. A distinction can be made between the theories for uniaxial fatigue and multiaxial fatigue. For both, the relevant theories are described in the next section.

4.2.1 Uniaxial fatigue

Existing theory on uniaxial fatigue is accepted by the classification societies and is considered reasonably well understood. The theory is stress and strain based for global and local approaches, as presented by D. Radaj and C.M. Sonsino [8]. The global approach has the advantage that it is less detailed, thus it requires less computation time. The local approaches have the advantage of being more accurate.

- Global approach
  - Nominal stress
- Local approaches
  - Hot spot structural stress
  - Notch stress

Nominal stress

Nominal stress is the stress calculated in the sectional area under consideration, disregarding the local stress raising effects of the welded joint, but including the stress raising effects of the macrogeometric shape of the component in the vicinity of the joint, such as e.g. large cutouts [9]. For materials having a ductile behavior the Von Mises stress criterion is used as equivalent stress criterion. Once the equivalent nominal stress amplitude is calculated, the multiaxial stress state is reduced to an equivalent uniaxial stress state. This equivalent stress approach should only be used for proportional loading or in-phase loading conditions, where the principal axes directions remain fixed during the loading cycle. For welded joints the equivalent stress can be compared to S-N curves (stress range vs fatigue life cycles, Figure 4.2) of a certain weld class type [10]. For each class of weld joint the relationship between the applied stress range and the number of cycles to failure under constant amplitude loading conditions is given in equation (4.9).

$$log(N) = log(C) - m * log(S) \tag{4.9}$$

with:

C	fatigue strength - scaling factor
m	slope - fatigue damage mechanism
N	fatigue life - number of cycles
S	stress range

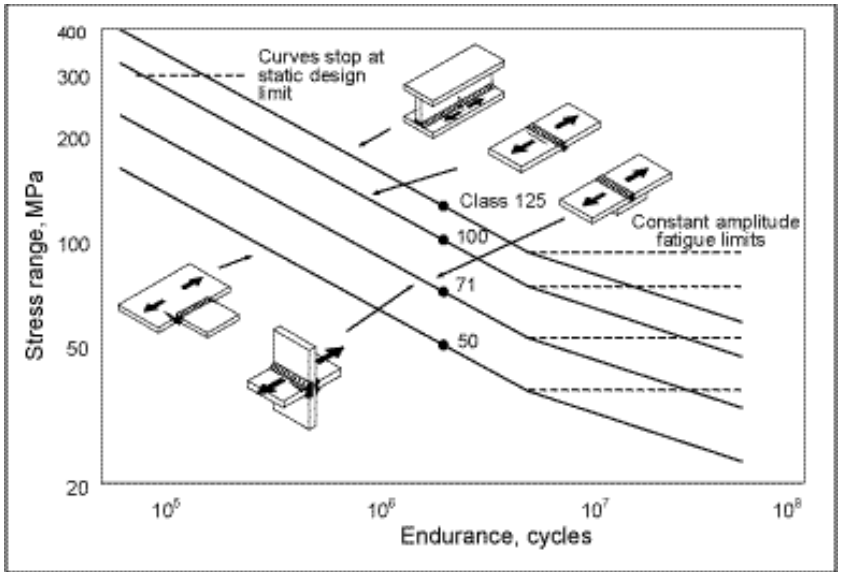

FIGURE 4.2: Example of S-N curves according to IIW design recommendation

Hot spot stress

The structural or geometric stress at the hot spot includes all stress raising effects of a structural detail excluding that due to the local weld profile itself. So, the non-linear peak stress caused by the local notch, i.e. the weld toe, is excluded from the structural stress [9]. The structural stress approach for welded joints aims to determine the structural stress at the crack initiation point of the weld toe (hot spot). And then to compare this stress with the nominal stress. Nominal and structural stress are considered to be equivalent in respect of a definite notch or detail class S-N curve. The stresses are determined at a small and a larger distance from the weld toe and after that linearly extrapolated to the weld toe, see Figure 4.3. The exact position of the two reference points is defined dependent on the geometrical parameters which determine the stress field. The hot spot structural stress approach is sufficiently well founded in the medium- and high-cycle fatigue range, the range with predominantly elastic behavior.

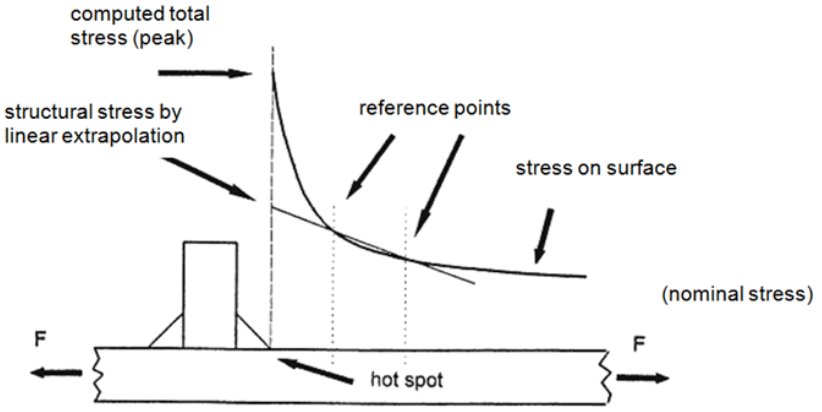

FIGURE 4.3: Definition of structural stress

Notch stress

Effective notch stress is the total stress at the root of a notch, obtained assuming linear-elastic material behavior. To take account of the variation of the weld shape parameters, as well as of the non-linear material behavior at the notch root, the actual weld contour is replaced by an effective one. For structural steels and aluminum alloys an effective notch root radius of r = 1 mm has been verified to give consistent results. For fatigue assessment, the effective notch stress is compared with a single fatigue resistance curve, although, as with other assessment methods, it is necessary to check that the fatigue resistance curve for parent metal is not exceeded [9].

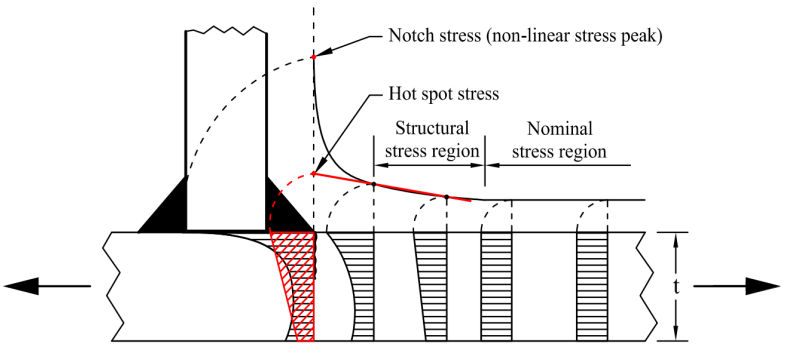

FIGURE 4.4: Definition of nominal, structural and notch stress

4.2.2 Multiaxial fatigue

Multiaxial fatigue analysis is categorized into five viewpoints according to B.R. You and S.B. Lee [11]:

- Empirical formulas and modifications of the Coffin-Manson equation
- Application of stress or strain invariants
- Use of the space averages of stress or strain
- Critical plane approaches
- Use of energy which has accumulated on the materials

The empirical formulas and modifications of the Coffin-Manson equation focus on an equivalent stress like Von Mises stress. The Von Mises stress is found to be inaccurate for multiaxial fatigue analyses. With the empirical formulas and the modifications of the Coffin-Manson equation the relation between experimental results and the Von Mises stress has improved. However this can only be used for proportional loading.
The application of stress or strain invariants describe the fatigue strength with stress invariants. These stress invariants are used to incorporate the nonlinear effect of higher mean stresses.
The use of the space averages of stress or strain define a generalized failure criterion. This failure criterion takes both normal and shear stress into account on a certain plane. This plane is based on averages of observed stresses in the material.
Fatigue analysis using the concept of critical plane is very effective because the critical plane concept is based upon the fracture mode or the initiation mechanism of cracks. In the critical plane concept, after determining the maximum shear strain (or stress) plane, many researchers define the parameter as the combination of the maximum shear strain (or stress) and normal strain (or stress) on that plane to explain the multiaxial fatigue

behavior.
All aforementioned stress- or strain-based criteria are lacking in consideration of the multiaxial stress-strain response of the material that is a crucial part of the fatigue process. The fatigue process is generally believed to involve cyclic plastic deformations which are dependent on the stress-strain path. Thus, the stress- or strain-based criteria cannot reflect the path dependence of the fatigue process sufficiently. The energy concept includes the explicit consideration of the multiaxial stress-strain response.

In this thesis both the critical plane approach and the energy concept are used. The critical plane is the plane in which the crack is expected to develop. For a welded joint this plane can be predicted according to experimental results. The influence of the stress-strain path is taken into account by using a certain way of counting the stress ranges per cycle. This method for counting is called PDMR (Path Dependent Maximum Range) and is later explained.

As stated earlier cyclic loading can cause proportional (in-phase) and non-proportional (out-of-phase) normal and shear stress, see Figure 4.5. For non-proportional loading the direction of the principal stresses varies with time. Experimental results on welded steel joints [12] and [13] show a decrease of fatigue life in presence of out-of-phase multiaxial loading if it is evaluated by means of an equivalent stress.

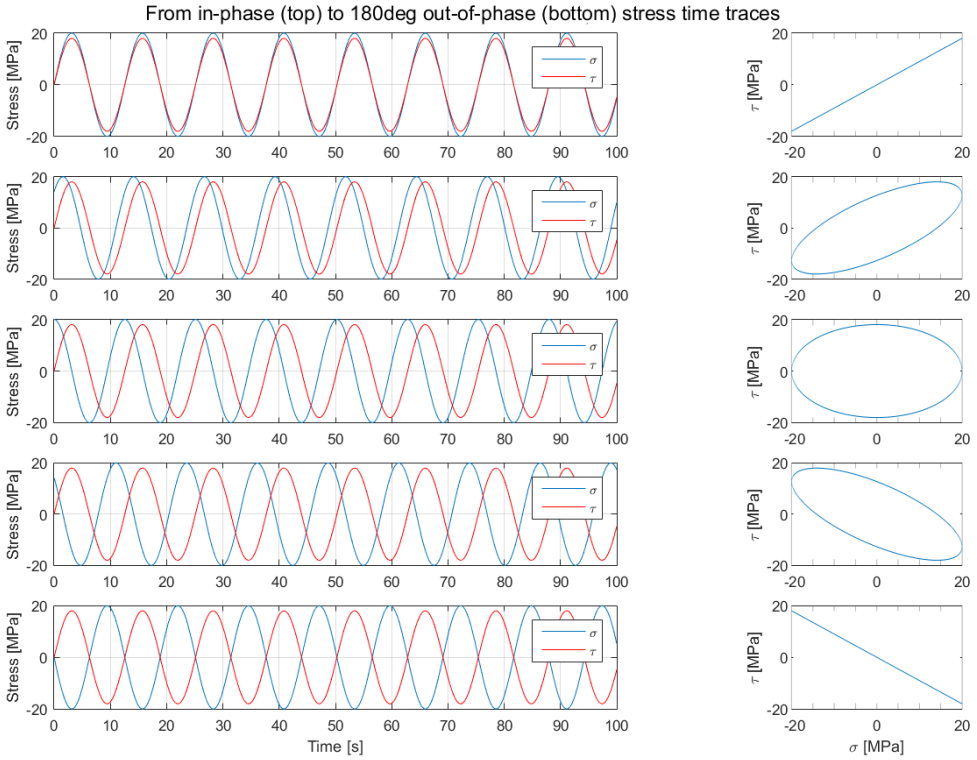

FIGURE 4.5: Example of proportionality between normal and shear stress

From the proportionality plots the presence of each stress component can be checked as well as the proportionality. For example, if the proportionality plot $\sigma - \sqrt{3}\tau$ is made for all stress components a total of nine plots will be created. In Figure 4.6 this is done for a vertical element from the welded joint, see in Figure 5.7, loaded by waves coming from 90 degrees. As can be seen the stresses σ_y, τ_{xy} and τ_{yz} are zero. Therefore only two of the proportionality plots show a non-proportional relation, these are $\sigma_x - \sqrt{3}\tau_{xz}$ and $\sigma_z - \sqrt{3}\tau_{xz}$. For the multiaxial fatigue analysis the normal stress is considered to be the stress perpendicular to the weld, so in the case of this vertical element the $\sigma_z - \sqrt{3}\tau_{xz}$ plot will be analyzed.

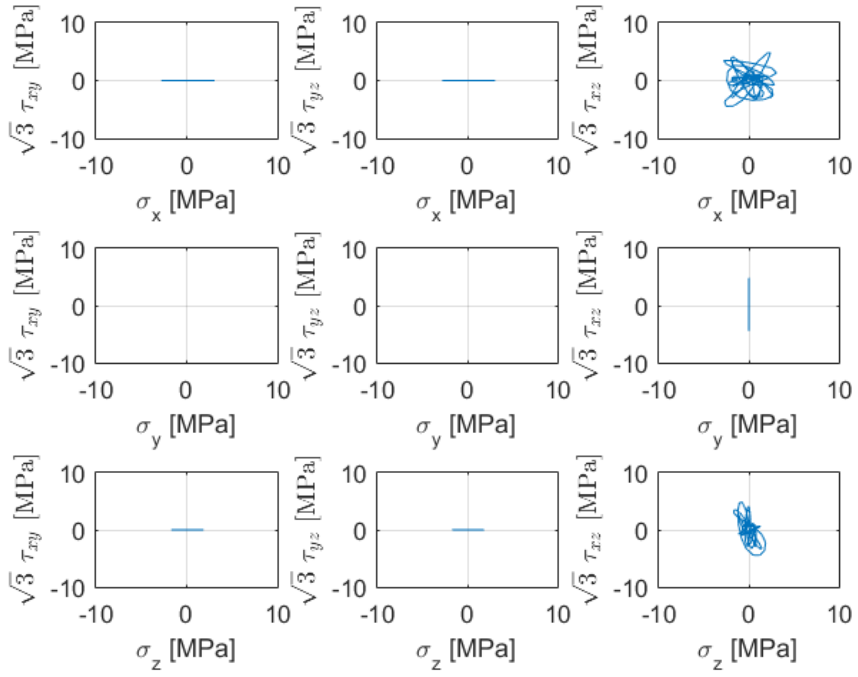

FIGURE 4.6: Example of proportionality for a vertical element in the welded joint

4.3 Fatigue crack growth

The fatigue process includes initiation or nucleation and growth of micro-cracks. Crack initiation life consists of crack nucleation and micro-crack growth up to a length of about several hundred micrometers (i.e. microscopic growth). At this length scale, microstructure texture and crack surface morphology can play a dominant role on crack growth behavior. For a weld these micro-cracks are already present due to process of welding. Crack growth life typically consists of a period of small crack growth followed by long crack growth (i.e. macroscopic growth). For the small crack growth regime, the crack is typically affected by the local plasticity and does not generate its own plastic zone. In contrast, longer cracks at the macroscopic level are generally less affected by the local plasticity and they generate their own plastic zone at the crack tip.

Three types of crack growth modes can be distinguished as seen in Figure 4.7. Mode I is caused by normal stresses, either tensile or compressive. Mode II and II are caused by shear stresses. Experimental observations suggest material, load magnitude, initial crack tip condition, load ratio, load phase relation and mean stress affect the crack growth mode. In plate-type geometries under multiaxial stresses, cracks often form under mixed-mode loading; however, they usually turn into a mode I macro-crack soon after micro-crack growth. The crack growth rate can be described by Paris' law (equation

4.10), which relates the stress intensity factor range to sub-critical crack growth under a fatigue stress regime. In this thesis the actual crack propagation and path are not analyzed.

$$\frac{da}{dN} = C\Delta K^m \tag{4.10}$$

with:

$\frac{da}{dN}$	crack growth rate	[mm/cycle]
ΔK	stress intensity factor range	[MPa]

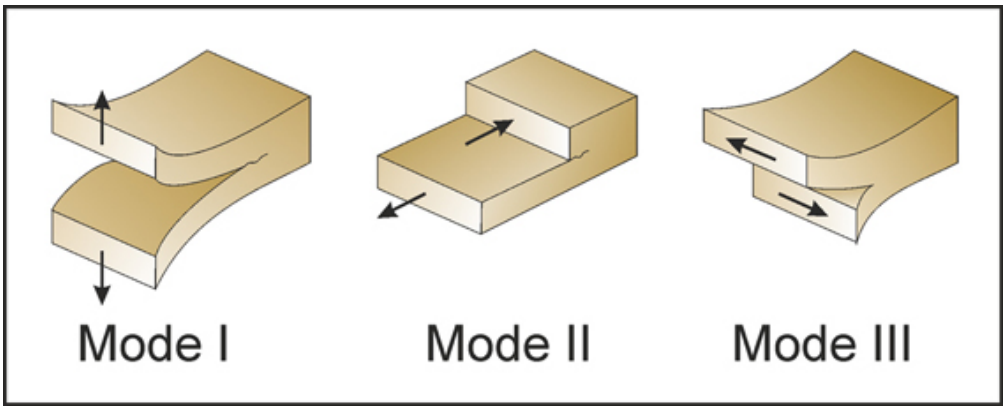

FIGURE 4.7: Types of crack growth modes

Chapter 5

Methods for fatigue analyses

In this chapter the methods used in this thesis to get the results for the different fatigue analyses are explained step by step. From finding the fatigue hot spot to the fatigue damage.

5.1 Governing load cases

To find the fatigue sensitive locations in the structure governing load cases are checked. The governing load cases are applied to the unloaded draft load case described in Chapter 2. These loads, consisting of wave pressures and inertial loads, are extracted from the hydrodynamic diffraction and translated by load mapping into the global FEM model. This leads to stresses in the structural members. From these stresses an initial understanding of the loading and the structure is gained.
First a case with significant wave height of 0 m is done to check the hydrostatic results. Then hydrodynamic cases can be run by defining wave direction, wave frequency/period, significant wave height and phase. The governing cases have the highest stress ranges at certain parts of the structure.
From DNV recommended practice C103 [14] multiple characteristic hydrodynamic responses for a typical twin pontoon semi-submersible are given. These responses are normally governing for the global strength of the unit. The installation unit is not very different from a twin pontoon semi-submersible with horizontal braces. Therefore it will be assumed that these responses (and small variations) are also the governing responses for the installation unit. The Von Mises stresses for four responses are checked. The relation between the wave length and wave period for 55m water depth is given by [3] and shown in Appendix C. The chosen waves for the four governing cases are shown in Figure 5.1.

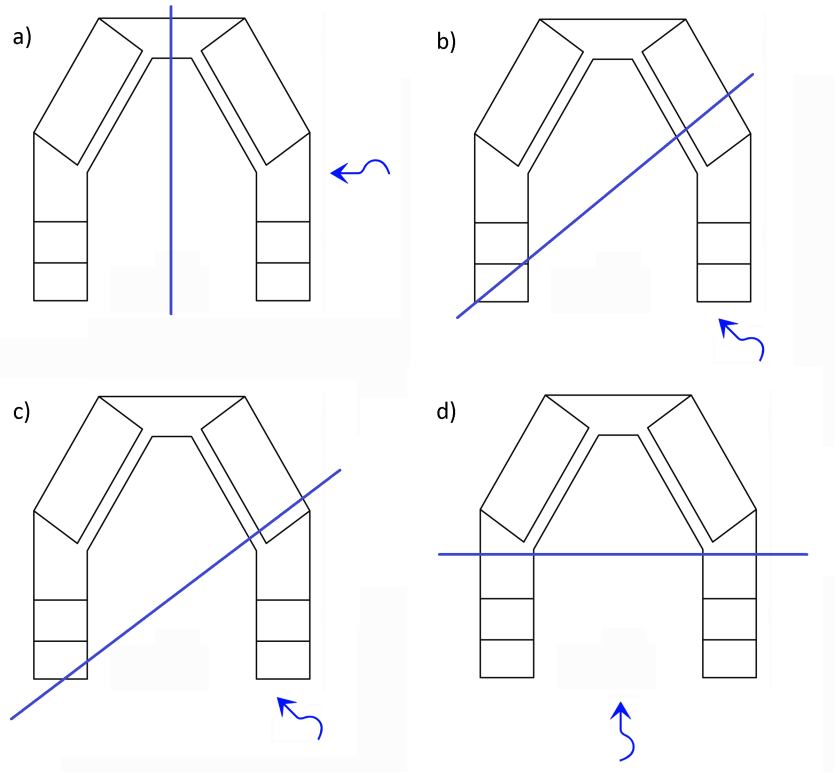

FIGURE 5.1: Waves crests for governing cases: a) Split b) Torsion c) Longitudinal shear d) Bending

5.1.1 Split force

A split force between the toes of the floater is critical for beam waves with a wave length of about twice the breadth of the unit. This response will give a maximum bending moment in the bow of the structure connecting the two toes of the floater. Also the diagonal braces take a large part of the response to keep the toes in place with respect to the bow of the structure. The maximum Von Mises stress is expected to be found for a wave phase of 0°when the wave crest is approximately in the center of the toes. Or for this beam wave with a wave phase between 90°and 150°when the wave crest is at one of the toes.

TABLE 5.1: Wave properties for the split force load case

H_s [m]	T_z [s]	Direction [deg]
2.0	9.67	90

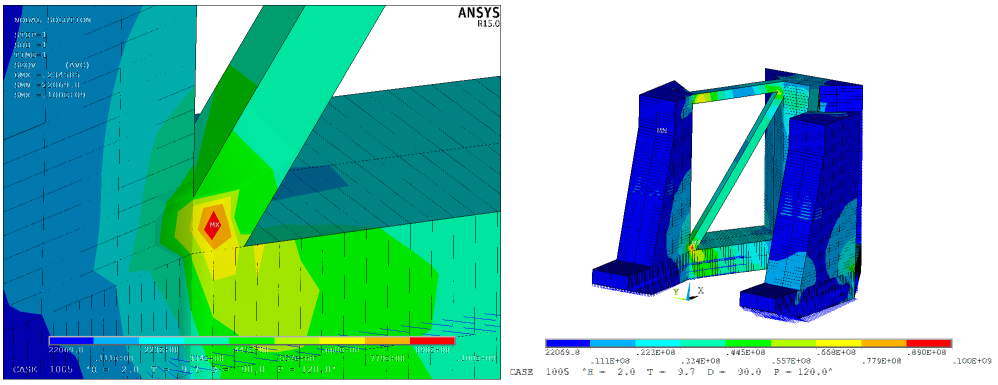

FIGURE 5.2: Von Mises stress contours for split force load case

5.1.2 Torsion moment

A torsion moment about a transverse horizontal axis is critical in a diagonal sea with a wave length of approximately the distance of the diagonal between the toe end and the corner of the bow. This response will give a maximum axial force in the diagonal braces. The diagonal wave will also cause a split force. The maximum Von Mises stress for the unit is expected to be for a wave direction between 30°and 60°and a wave phase of 0°.

TABLE 5.2: Wave properties for the torsion moment load case

H_s [m]	T_z [s]	Direction [deg]
2.0	7.39	60

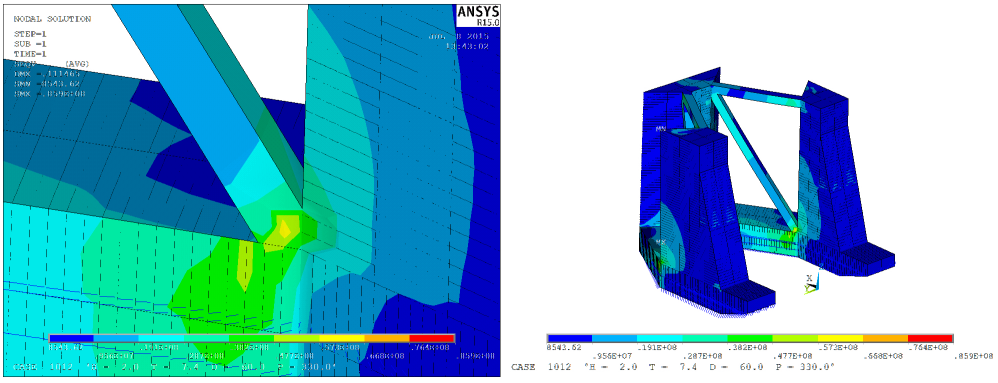

FIGURE 5.3: Von Mises stress contours for torsion moment load case

5.1.3 Longitudinal shear force

A longitudinal shear force between the toes of the floater is critical in a diagonal sea with a wave length of approximately 1.5 times the distance of the diagonal between the

toe end and the corner of the bow. This response has the same force components as the torsion moment load case but now the longitudinal shear forces are maximized. The maximum Von Mises stress for the unit is expected to be for a wave direction between 30°and 60°and a wave phase of 0°.

TABLE 5.3: Wave properties for the longitudinal shear force load case

H_s [m]	T_z [s]	Direction [deg]
2.0	8.98	60

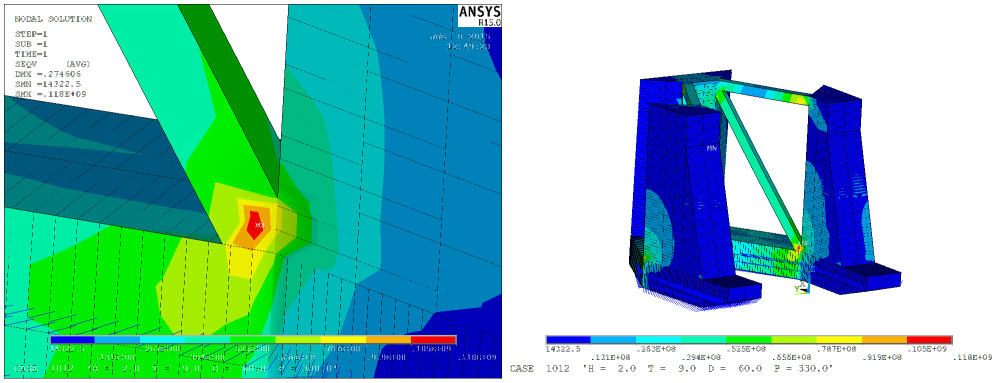

FIGURE 5.4: Von Mises stress contours for longitudinal shear load case

5.1.4 Bending moment

A vertical wave bending moment is critical for head waves and a wave length of approximately the length of the unit. This response will cause a bending moment on the floater of the unit. The maximum Von Mises stress for the unit is expected to be for a wave with a phase of 0°.

TABLE 5.4: Wave properties for the bending moment load case

H_s [m]	T_z [s]	Direction [deg]
2.0	6.61	0

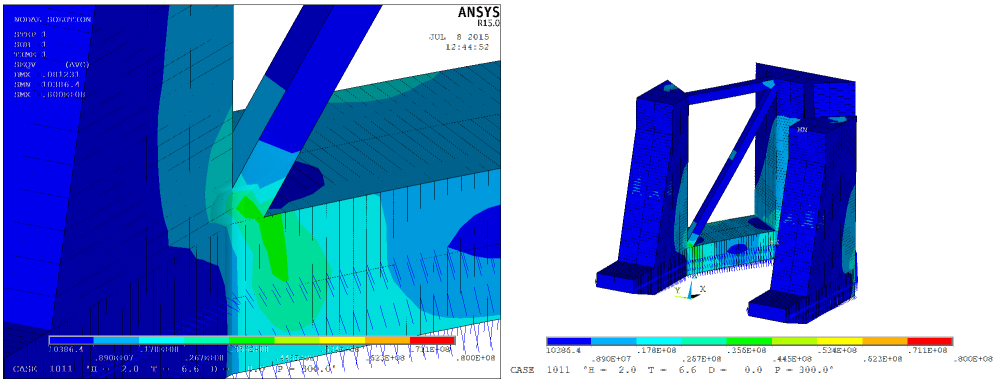

FIGURE 5.5: Von Mises stress contours for bending moment load case

5.2 Hot spot location

From these governing load cases it can be concluded which parts of the structure are governing for the fatigue life. For all four cases the lower connection of the diagonal braces is considered a hot spot with regard to fatigue. This is because the Von Mises stress range at this part of the structure is relatively high. From here on the horizontal, longitudinal welded connection between the diagonal brace and the floater is considered for the fatigue analysis as shown in Figure 5.6. Only the loading due to waves when the unit is at unloaded floater draft is considered.

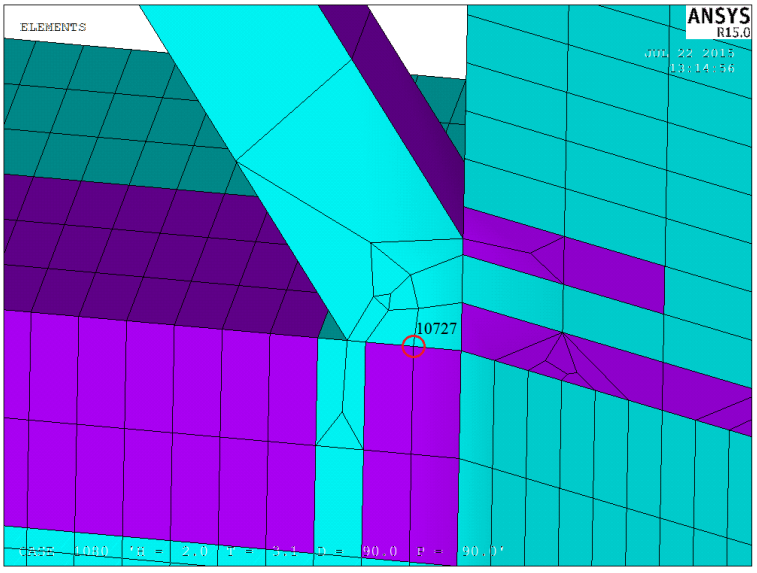

FIGURE 5.6: Node 10727, located on the longitudinal weld connecting the diagonal brace with the floater

5.2.1 Welded joint

Multiple nodes are located on the weld in this part of the structure. The elements used for the fatigue analysis are the elements connected to node number 10727, see Figure 5.7. Multiple elements are connected to this node and each element has a stress output consisting of three normal stresses and three shear stresses for both sides of the plate. These stresses are translated from the global to a local coordinate system. An example of this output is given in Figure 5.8. From this output the normal stress perpendicular to the weld and the corresponding shear stress in the weld for each element are extracted. And also the in-plane principal stresses for each element can be determined.

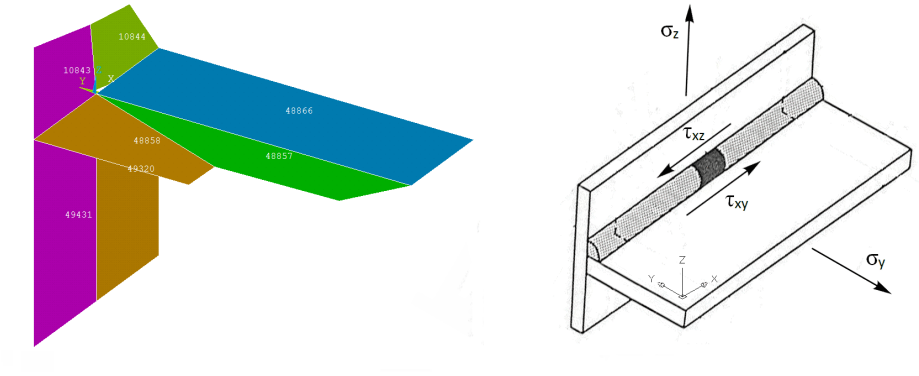

FIGURE 5.7: Elements connected to node 10727 with local coordinate system

```
PRINT S    ELEMENT SOLUTION PER ELEMENT

***** POST1 ELEMENT NODAL STRESS LISTING *****

 LOAD STEP=    15  SUBSTEP=     1
  TIME=    15.000      LOAD CASE=   0
 SHELL RESULTS FOR TOP/BOTTOM ALSO MID WHERE APPROPRIATE

 THE FOLLOWING X,Y,Z VALUES ARE IN COORDINATE SYSTEM   11


 ELEMENT=   10843        SHELL181
   NODE     SX          SY          SZ          SXY         SYZ         SXZ
  10748  0.99448E+06 0.11128E-02 0.24180E+06 -33.267      22.595    -0.67546E+06
  10727  0.99448E+06 0.11128E-02 0.24180E+06 -33.267      22.595    -0.67546E+06
   9456  0.99448E+06 0.11128E-02 0.24180E+06 -33.267      22.595    -0.67546E+06
   9457  0.99448E+06 0.11128E-02 0.24180E+06 -33.267      22.595    -0.67546E+06
  10748  0.98670E+06 0.11041E-02 0.23847E+06 -33.006      22.239    -0.66481E+06
  10727  0.98670E+06 0.11041E-02 0.23847E+06 -33.006      22.239    -0.66481E+06
   9456  0.98670E+06 0.11041E-02 0.23847E+06 -33.006      22.239    -0.66481E+06
   9457  0.98670E+06 0.11041E-02 0.23847E+06 -33.006      22.239    -0.66481E+06
```

FIGURE 5.8: Example of output for an element connected to node 10727. For each node connected to the element the stress in the top and bottom of the plate is given.

5.3 Flow diagram: From stress RAOs to stress time traces

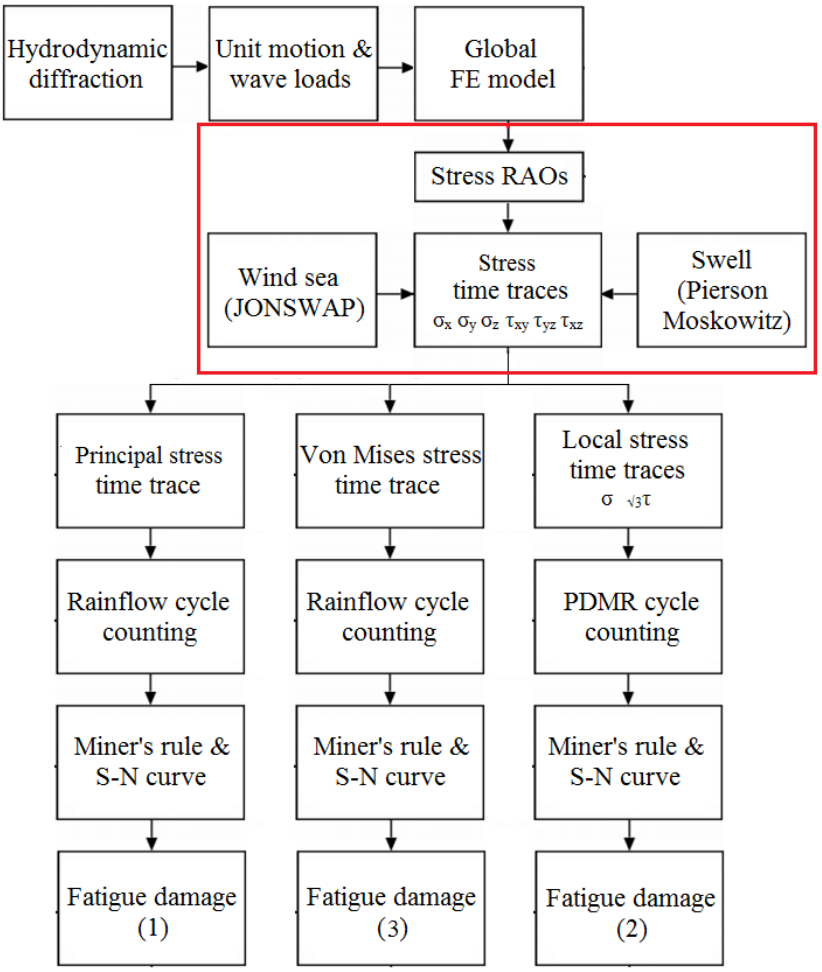

FIGURE 5.9: Flow diagram: From stress RAOs to stress time traces

5.4 Stress RAOs

5.4.1 In- and out-of-phase components

For a certain wave direction, 40 different wave frequencies (0.05 - 2 rad/s) are considered. To obtain the stress response of the structure in time two phases of each frequency are considered. One component which is in-phase and one component which is out-of phase (phase angle 90°). By combining the in-phase and out-of-phase the stress response for that wave frequency and wave direction is obtained, see equation (5.1).

$$\sigma(t) = A * cos(\omega * t) + B * cos(\omega * t + \frac{\pi}{2}) \tag{5.1}$$

5.4.2 Magnitude and phase

The stress RAO is the stress response of the structure to regular waves with a certain wave direction. To do a multiaxial fatigue analysis it is necessary to have a stress RAO for both the normal and shear stress.
To get the stress RAO the magnitude for each frequency has to be determined, equation (5.2). This means that for a single wave direction 80 wave loads are considered to obtain the stress RAO. The phase relation corresponding to each frequency is also determined as they will be used later in the analysis, equation (5.3).

$$|\sigma| = \sqrt{A^2 + B^2} \tag{5.2}$$

$$\angle\sigma = tan^{-1}(\frac{B}{A}) \tag{5.3}$$

The normal stress RAO (σ_z) for wave loading with 90 degree wave direction is shown in Figure 5.10. From this RAO it can be seen that there is a peak in the RAO at a frequency of $0.65 rad/s$. This frequency coincides with a wave length of about half the width of the structure. So apparently for this wave length the normal stress in vertical direction at the weld has a maximum. Which can be explained because for this wave the starboard side of the unit would be in a trough while the port side is in the wave peak. Thus the structure has a relatively large vertical deformation for this particular wave.

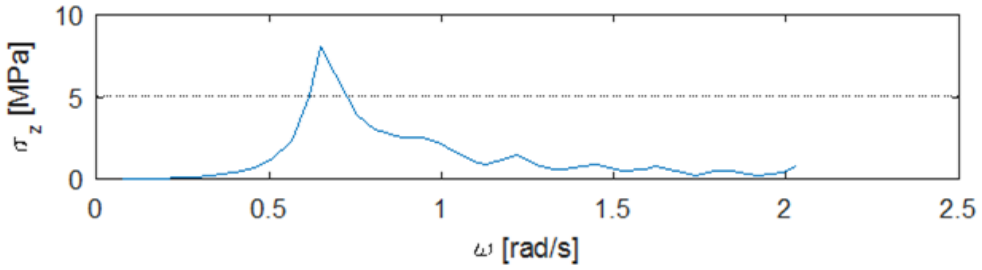

FIGURE 5.10: Stress RAO σ_z for waves coming from 90 degrees

5.5 Sea states

An operation timeline is created in which the operation phases of the installation unit are described in time windows of 6 hours. This is done for a specific part of the North Sea related to meteorological data for 10 years time (1997-2006). The operation phases

consist of float on, connecting, float off, positioning and releasing. In between the operation phases a waiting time is built in because each operation requires a certain limit sea state. From this timeline the total exposure time at unloaded floater draft can be determined with the corresponding average sea states and wave directions for both wind sea as swell. The exposure time is used to determine the fatigue damage. The total exposure time at unloaded floater draft for 10 year data is 36,438 hours, which is about 4 years. This is very conservative because for long waiting times the unit will submerge to reduce the loading on the structure. The time the unit is submerged is not taken into account for now.

In Figure 5.11 a wave scatter diagram for both the wind sea and swell is given for the sea states when the unit is at unloaded floater draft. Each point represents the significant wave height and peak period of 6hr measurements. The unit is assumed to be 90 degrees with respect to the transportation vessel. The transportation vessel is assumed to be taking head waves from swell, which means the installation unit is in beam waves from swell. In Figure 5.12 the relative wave direction of the wind sea to the swell is shown.

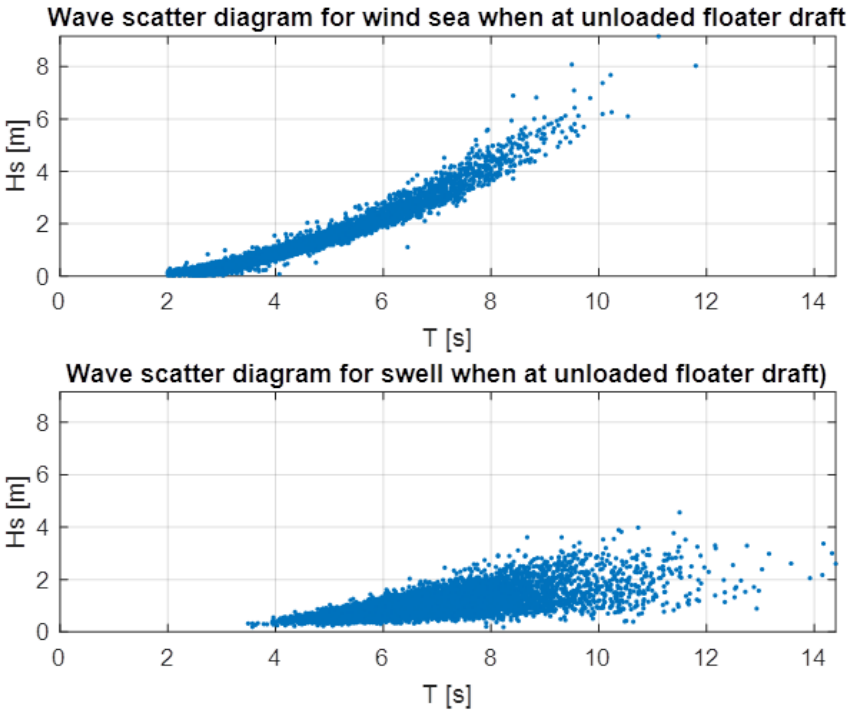

FIGURE 5.11: Wave scatter diagrams for when the unit is at unloaded floater draft

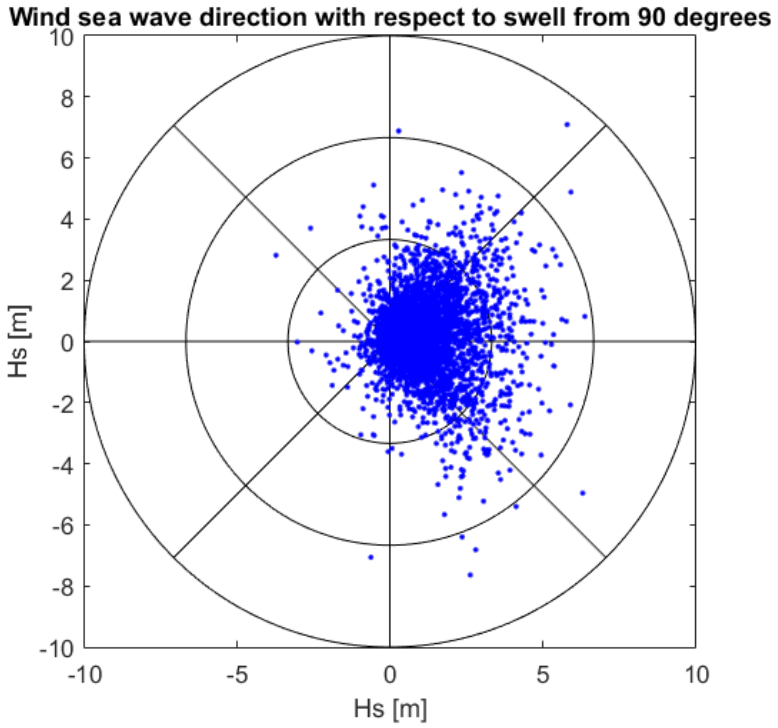

FIGURE 5.12: The wind sea wave direction with respect to swell

5.6 Wave spectra

The waves should be modeled as irregular to get a more realistic stress response of the structure to the waves. This can be realized by combining the stress RAOs with wave spectra. The wave spectra depend on the location where the installation unit will be operating. The chosen wave spectra are the Pierson Moskowitz and the JONSWAP spectrum, since the unit is expected to be operating in the North Sea. The Pierson Moskowitz spectrum is used for the swell component and JONSWAP spectrum is used for the wind sea component. The spectra are described by a significant wave height (H_s), a peak period (T_p) and a peakedness factor (γ), see equation (5.4). The Pierson Moskowitz is computed by a peakedness factor of 1 and the JONSWAP by a peakedness factor of 3.3. The significant wave height and peak period are the parameters that define the sea state.

$$S(\omega) = A_\gamma \frac{5}{16} H_s^2 f_p^4 \omega^{-5} exp\left(\frac{-5}{4}\left(\frac{\omega}{f_p}\right)^{-4}\right) \gamma^{exp(-0.5\left(\frac{\omega - f_p}{\sigma - f_p}\right)^2)} \tag{5.4}$$

with:

A_γ	$1 - 0.287ln(\gamma)$
f_p	$\frac{2\pi}{T_p}$
σ	0.07 for $\omega \leq f_p$ and 0.09 for $\omega > f_p$

5.7 Stress time traces

The wave spectra give the distribution of energy for the different wave frequencies and are related to the amplitude of the waves. To get the amplitude of the stress time trace the magnitude of the stress RAO is multiplied with the wave energy per frequency step. This is done for each ith frequency.

$$R_i = |\sigma|\sqrt{2S(\omega)\Delta\omega} \tag{5.5}$$

So for every frequency a sinusoidal function of time is defined with amplitude R_i and a phase relation ($\angle\sigma$). The sum of all these sinusoidal functions will give a stress time trace, see equation (5.6). This approach is done for three normal stress directions (σ_x, σ_y and σ_z) and three shear stress directions (τ_{xy}, τ_{yz} and τ_{xz}).

$$\sigma(t) = \sum_{i=1}^{40} R_i cos(\omega_i t + \angle\sigma) \tag{5.6}$$

In Figure 5.13 an example of stress time traces is given for a vertical element. In this example the wave elevation and the six stress components are shown for a total time of 60 seconds. Within this time trace multiple cycles can be observed and the relation between the wave elevation and the stresses is clear, with respect to amplitudes and phases.

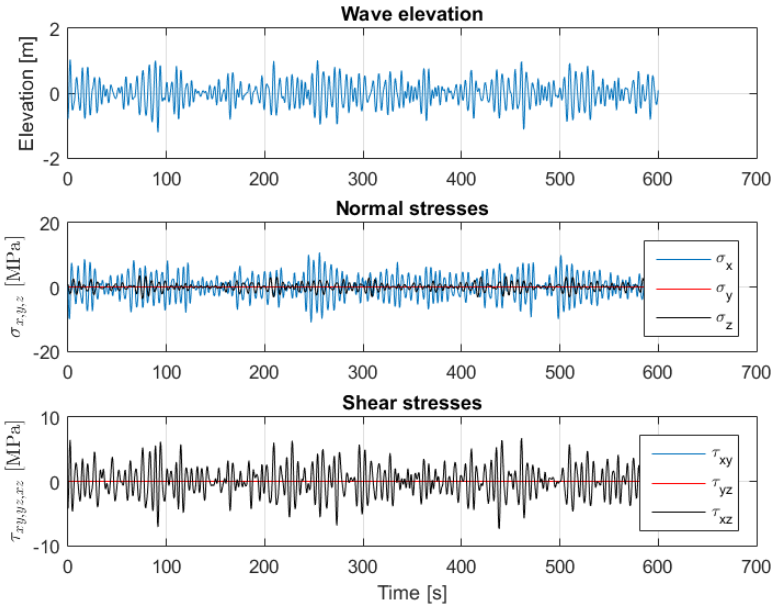

FIGURE 5.13: Example of stress time traces

By combining the stresses at each time step the time trace of equivalent stresses, like the principal stresses and the Von Mises stress, can be determined. Examples are given in Figure 5.14. As the direction of the principal stresses change also the angle as a time trace can be seen.

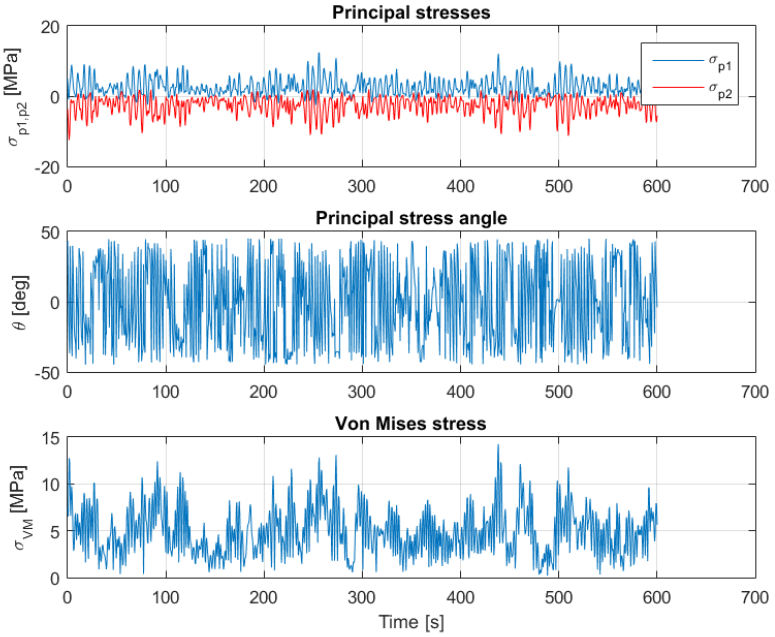

FIGURE 5.14: Example of equivalent stress time traces

5.8 Flow diagram: From stress time traces to fatigue damage

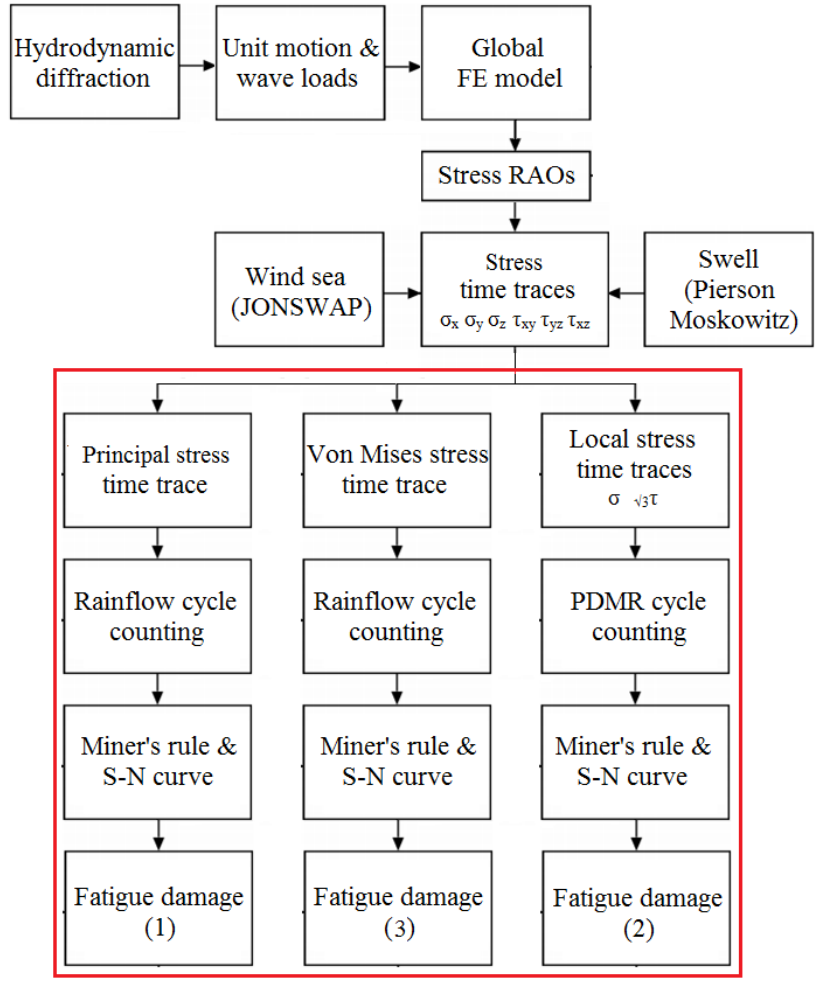

FIGURE 5.15: Flow diagram: From stress time traces to fatigue damage

5.9 Cycle counting

5.9.1 Rainflow method counting

The rainflow method counting is a particular method of counting the numbers of stress cycles of different magnitudes which occur in a stress history. The loads applied to the structure, considered in sequence, generate a particular stress history at each detail of interest. This stress history can be broken down into equivalent numbers of stress ranges of different magnitudes by the operation of cycle counting. The rainflow method is described in detail by ASTM-1049-85 [15]. A step by step approach from ASTM is given in Appendix D.

5.9.2 PDMR cycle counting

To show the proportionality between the normal stress and shear stress time traces a $\sqrt{\beta}\tau - \sigma$ plot is made. This plot shows the load path. With the Path-Dependent Maximum Range (PDMR) given by [16], [17] it is possible to retrieve the stress range per $\frac{1}{2}$ cycle for non-proportional multiaxial loading. An example of PDMR cycle counting is given in Appendix E.
PDMR cycle counting is performed by following certain steps repeatedly. These steps are:

- Find the maximum possible distance within the $\sqrt{\beta}\tau-\sigma$ history. The path between these points is the load path considered first.
- Two results will be gained from this load path, the reference stress range and the effective stress range.
- The maximum distance will be the reference stress range.
- The actual load path will determine the effective stress range
  - Start adding path length at the beginning of the path, while there is a monotonic increase in the path it adds to the effective stress range.
  - If a further increase in time will result in a decrease in distance a turning point is defined.
  - The length between the starting point and the turning point is the radius of an arc. Where the arc intersects the load path a projected turning point is defined.
  - The arc length (virtual path) between turning point and projected turning point adds to the effective stress range.
  - While there is a monotonic increase in the path after the projected turning point it is added again. If not then another turning point and projected turning point are defined. Until the monotonic increase reaches the end point of the load path.
  - The added total of the counted path is the effective stress range.
- The paths between the turning points and projected turning points return to the $\sqrt{\beta}\tau - \sigma$ history. The rest of the path in the maximum distance is removed.
- For the remaining $\sqrt{\beta}\tau-\sigma$ history the previous steps are repeated until the $\sqrt{\beta}\tau-\sigma$ history is empty.
- Each corresponding reference and effective stress range belong to 0.5 cycle.

In this thesis the PDMR cycle counting is simplified. This done according to: virtual paths are taken as the shortest distance between a turning point and the first data point after the position of the corresponding projected turning point. The length of the arc that should be counted is a bit larger, that is why the virtual paths are corrected by adding 5% of the path.

5.10 Difference between counting methods

The difference between both counting methods is the fact that the normal and shear stresses act simultaneously. The rainflow counting method is used separately for each stress time trace. This means that each load on the weld is considered individually and the sum of the damage due to these loads is the total damage. The PDMR counting method considers both loads together. Therefore the load path and the phase relation between the stresses is taken into account.
Physically the difference means that the counted stress ranges from rainflow counting are uniaxial. This means that the fatigue damage (crack growth) is determined by each stress individually, so the damage by mode I, mode II and mode III added. However for the PDMR the counted stress ranges are multiaxial. The different modes can act at the same time, which means the crack can be under tensile stress and shear stress simultaneously. This means the crack can be pulled open and sheared at the same time.

5.11 S-N curves

A detail class is a rating given to a particular structural detail to indicate which of the fatigue strength S-N curves should be used in the fatigue assessment. In the IIW code of practice [10] and DNV [18] the class is denoted by one of the following letters: A, B, C, D, E, F, G, S, T, W or X. The categorization takes into consideration the local stress concentration at the detail, the size and shape of the maximum acceptable discontinuity, the stress direction, metallurgical effects, residual stresses, fatigue crack shape, and in some cases the welding process and a post-weld improvement method.
The classes of S-N curves corresponding to the welded joint considered are given in Table 5.5.

The schematic drawings of the welded joint with the loading are given in Figure 5.16, in the drawings the expected crack is also shown. The corresponding SN curves needed for the welded joint are given in Figure 5.18.
The SN curve corresponding to the principal stress is dependent on the direction of the

TABLE 5.5: SN curve for each stress component

Stress component	**SN curve**
σ_z	Class E
τ_{xz}	Class E
σ_y	Class W3
τ_{xy}	Class E
σ_{p1}	Class E [18]
σ_{VM}	Master SN curve
$\sigma - \sqrt{3}\tau$	Master SN curve

principal stress with respect to the perpendicular direction to the weld. To illustrate this a top view of the weld and the angles are given in Figure . The corresponding SN curve classes are also given in the Figure. Since the principal stress remains within 45 degrees in both directions class E is considered as the corresponding SN curve. This is a simplification but for the means of the qualitative comparison it is considered sufficient.

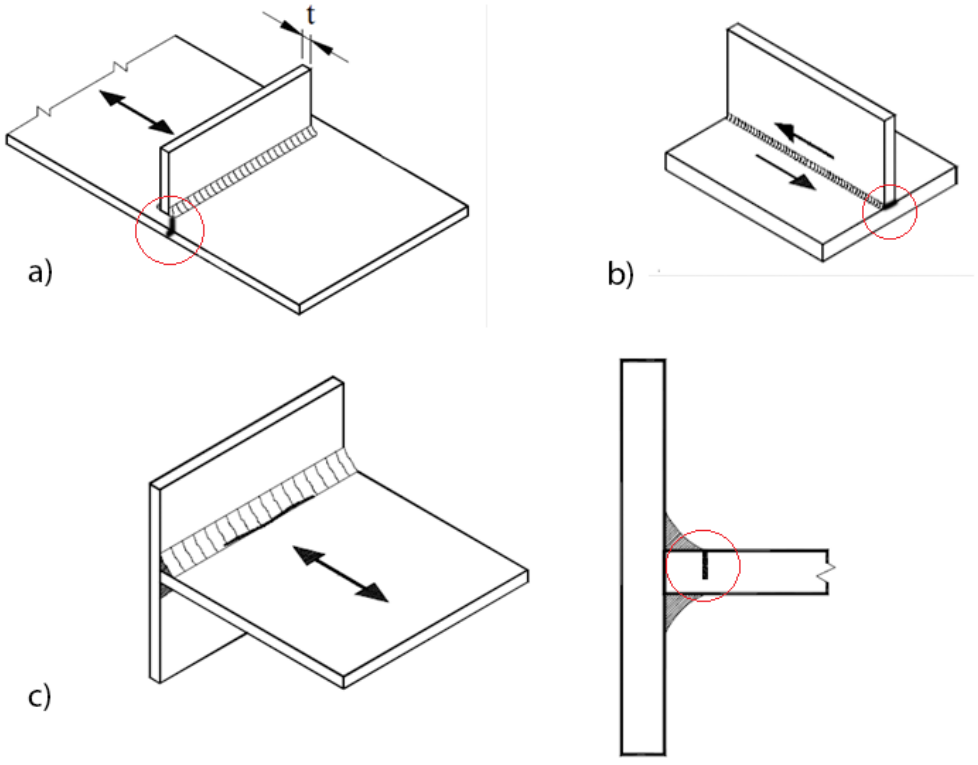

FIGURE 5.16: Schematic drawings of welded joint. a) σ_z, b) τ, c) σ_y

Angle φ	*Detail classified as E for stress direction normal to the weld*
0 - 30	E
30 - 45	D
45 - 60	C2
60 - 75	C2
75 - 90	C2*

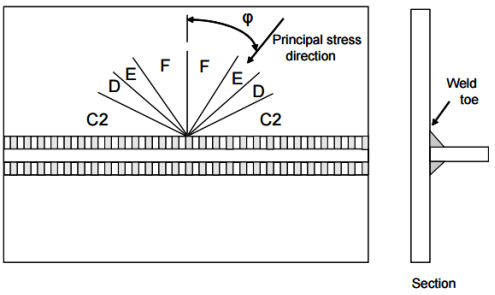

FIGURE 5.17: SN curve classes for principal stress

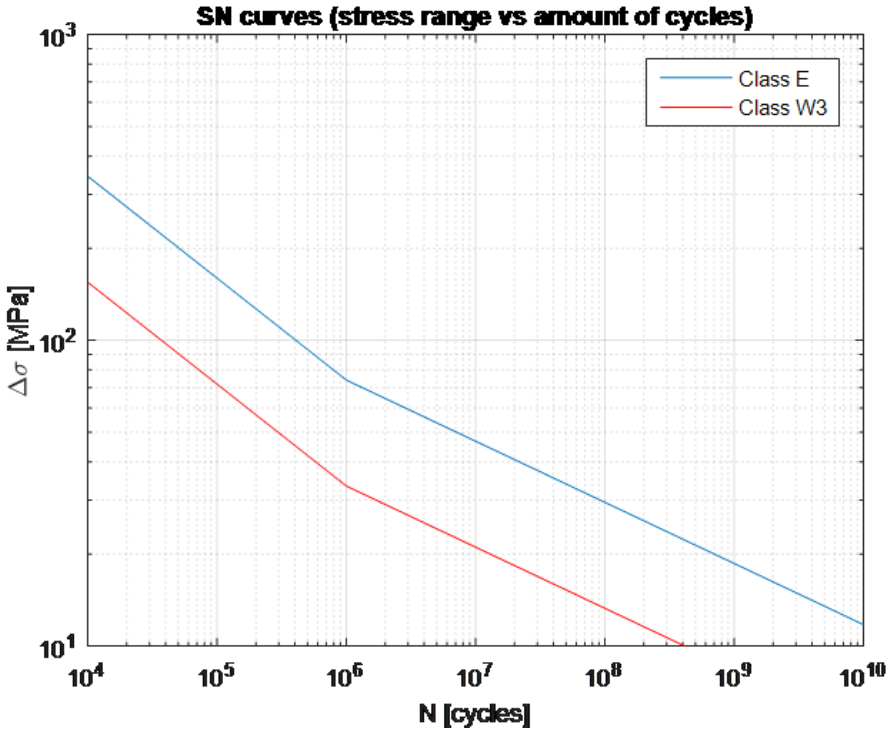

FIGURE 5.18: SN curves for class E and W3

The master SN curve is constructed from a lot of data from fatigue tests in ASME div2 by P. Dong and J.K. Hong [19], [20]. Before the counted stress ranges can be related to the master SN curve the stress ranges have to be normalized to get an equivalent structural stress range. The equation to normalize the counted stress ranges is given in equation 5.7. The value for m is 3.6 and I(r) to the power of 1/m is considered 1.2. The corresponding master SN curve is given in Figure 5.19.

$$\Delta S = \frac{\Delta\sigma}{t^{\frac{2-m}{2m}} I(r)^{\frac{1}{m}}} \tag{5.7}$$

with:

$I(r)$	dimensionless function of bending	-
ΔS	equivalent structural stress range	[MPa]

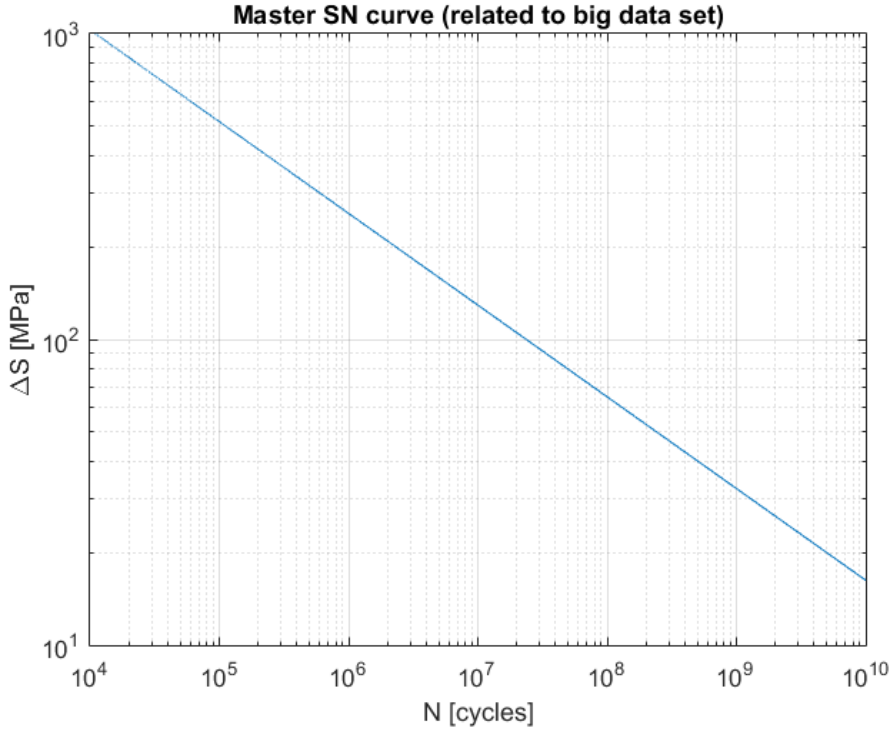

FIGURE 5.19: Master SN curve

5.12 Palmgren-Miner rule

For a joint subjected to a number of repetitions n_i of each of several stress ranges, the value of n_i corresponding to each stress range should be determined. The number of cycles to failure N_i at each stress range, should then be determined from the basic S-N curves, modified as necessary for the relevant detail class at the selected probability of failure. The design should then be modified so that the cumulative damage (Miner's) summation is as follows:

If all values of the stress ranges are less than the constant amplitude initial non-propagating stress range (S_0 at N = 10^7 cycles) don't need to be considered. However, if any values of stress ranges exceed S_0, all the stress ranges including those below S_0, need to be included in the summation. This is because the higher stresses in the spectrum of stress ranges are capable of propagating cracks which may then be propagated further by the lower stresses.

A limitation of the Palmgren-Miner rule is that it does not consider sequence effects, the order of loading makes no difference. Another limitation is that the damage accumulation is independent of the stress magnitude, it is dependent on the stress range and

does not take the stress amplitude into account. And also the rule is not able to take nonlinear effects into account. If the elastic limit is exceeded in a couple of stress cycles then the relation between the stress and strain will be nonlinear, which will be yielding. This will cause the damage accumulation to be different from the Palmgren-Miner rule.

$$D = \sum \left(\frac{n_i}{N_i} \right) \tag{5.8}$$

with:

D	cumulative damage
N_i	number of loading cycles to failure
n_i	number of repetitions of stress ranges during structure design life

Chapter 6

Results

In this chapter the results are presented with regard to the fatigue analyses. A uniaxial comparison between both counting methods is performed. The stress ranges for different elements under the same loading condition are shown. And finally a comparison between the fatigue damage factors are made for multiple wave direction cases and different elements.

6.1 Rainflow vs PDMR for uniaxial stress

6.1.1 Short time trace

For a uniaxial loading, either the normal or the shear stress is zero, the results of both the counting methods should be exactly the same. A uniaxial comparison between rainflow counting and pdmr counting for a time trace of about 30 seconds is made. A vertical element is considered with sea states for both swell and wind sea of $H_s = 1.5m$ and $T_p = 6s$ where both components are coming from 90deg wave direction.
The time trace of both σ_z and τ_{xz} for this case can be seen in Figure 6.1.

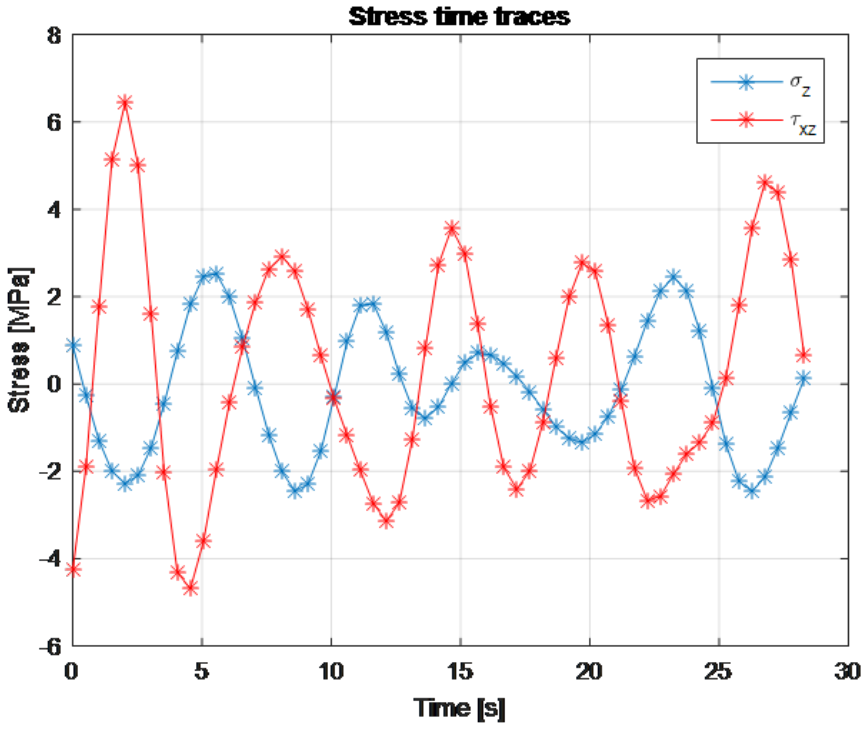

FIGURE 6.1: Time trace of stresses

If the uniaxial case where τ is equal to zero is considered, then the $\sigma - \sqrt{3}\tau$ plot would be Figure 6.2. By counting these plots both by rainflow counting and by PDMR counting the stress ranges per half cycles are determined. For the uniaxial case these results should be exactly the same. A small difference between the two counting methods can be observed in Figure 6.3.

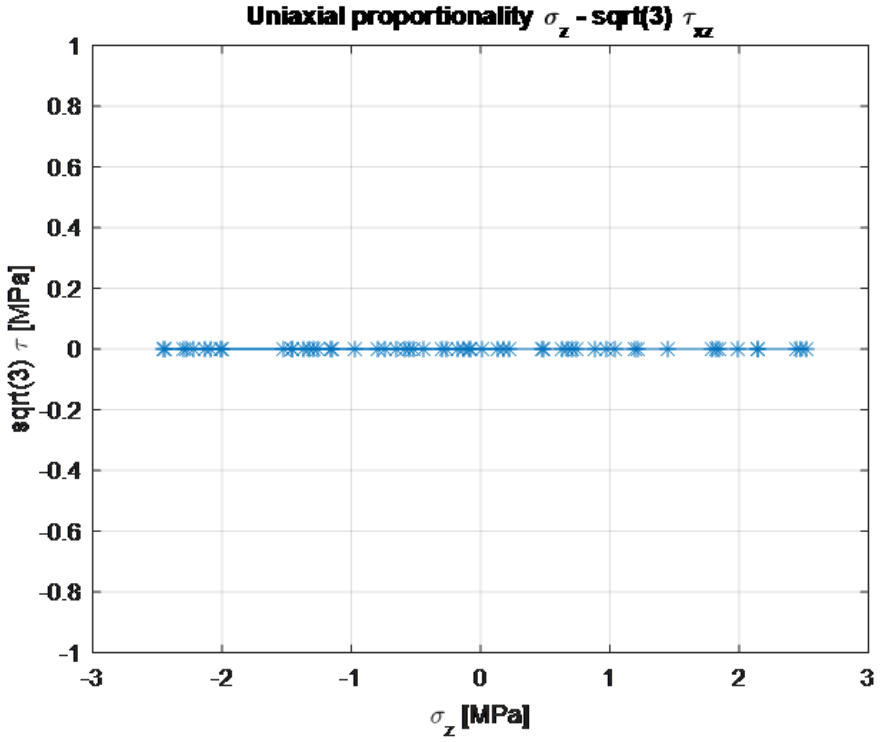

FIGURE 6.2: Uniaxial proportionality for $\tau = 0$

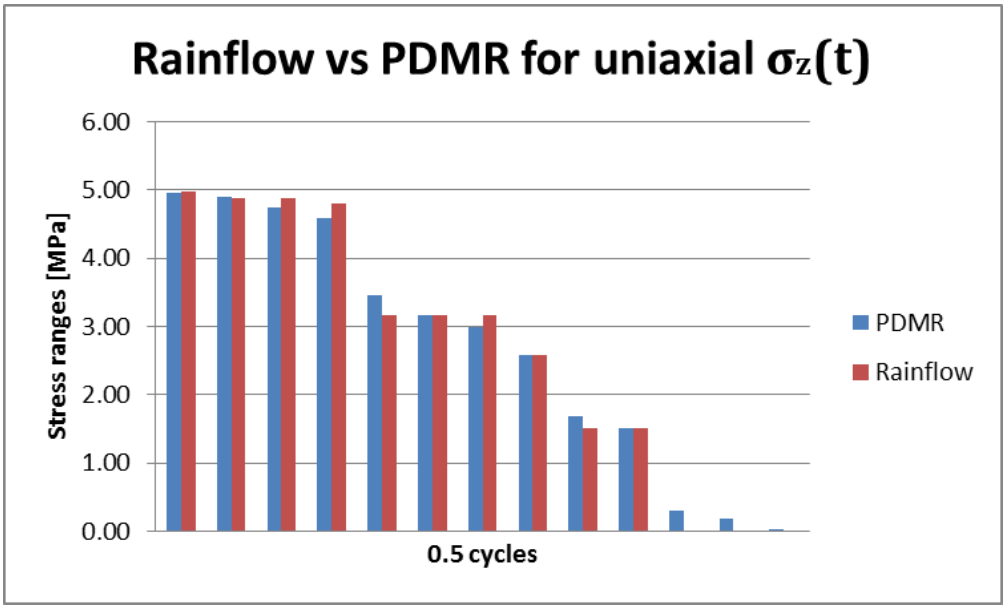

FIGURE 6.3: Stress ranges for rainflow counting and PDMR counting

The same process is done for the uniaxial case where σ is zero, then the $\sigma - \sqrt{3}\tau$ plot would be Figure 6.4. Again both counting methods should give the exact same result but a small difference is observed.

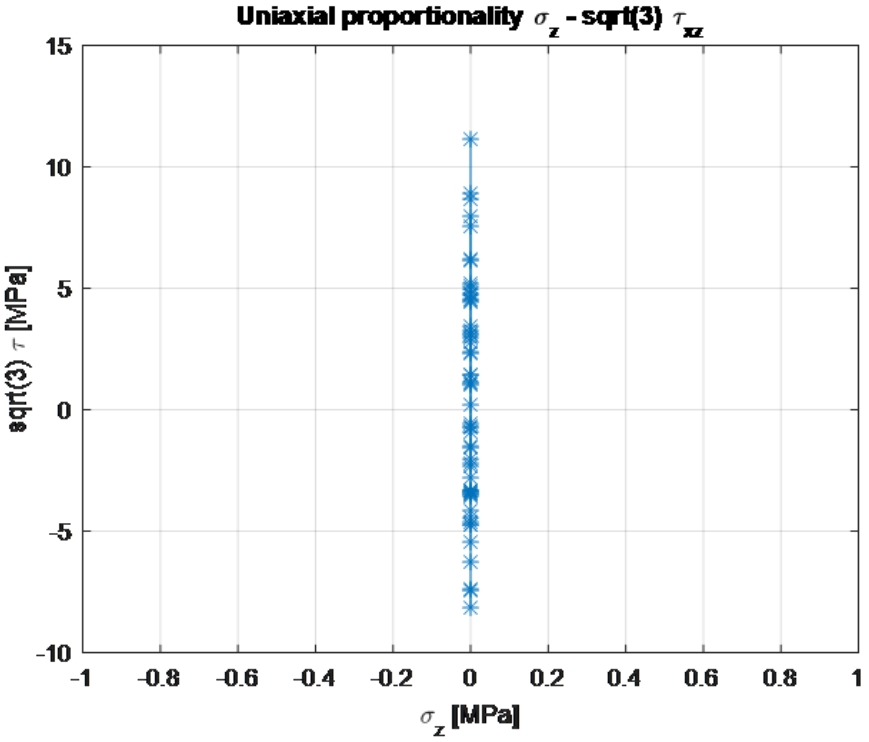

FIGURE 6.4: Uniaxial proportionality for $\sigma = 0$

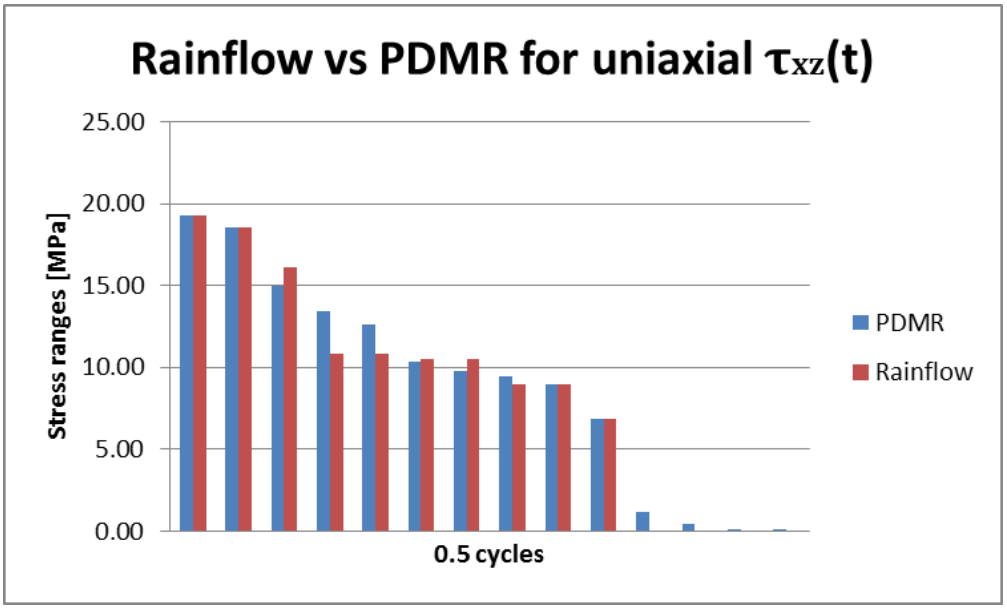

FIGURE 6.5: Stress ranges for rainflow counting and PDMR counting

The essential information from both these checks is shown in Table 6.1 and 6.2. From these tables the small difference between both counting methods can be seen directly.

TABLE 6.1: Difference between counting methods for $\tau = 0$ uniaxial case

	PDMR	**Rainflow**
Total cycles	6.5	5
Max stress range	4.97 MPa	4.98 MPa
Mean stress range	2.70 MPa	3.46 MPa
Fatigue damage	2.56e-12	2.73e-12

TABLE 6.2: Difference between counting methods for $\sigma = 0$ uniaxial case

	PDMR	**Rainflow**
Total cycles	7	5
Max stress range	19.28 MPa	19.28 MPa
Mean stress range	9.00 MPa	12.14 MPa
Fatigue damage	1.50e-9	1.48e-9

6.1.2 Longer time trace

Also a uniaxial comparison between rainflow counting and PDMR counting for a time trace of 2 hours is made. This is done to check the effect of the small inaccuracy between the two counting methods. The results from these time traces are shown in Table 6.3 and 6.5.

TABLE 6.3: Difference between counting methods for $\tau = 0$ uniaxial case (2 hr)

	PDMR	**Rainflow**
Total cycles	1735	1223
Max stress range	7.71 MPa	7.71 MPa
Mean stress range	1.93 MPa	2.70 MPa
Fatigue damage	4.62e-10	5.35e-10

TABLE 6.4: Difference between counting methods for $\sigma = 0$ uniaxial case (2 hr)

	PDMR	**Rainflow**
Total cycles	1974	1389
Max stress range	31.06 MPa	31.06 MPa
Mean stress range	6.44 MPa	8.96 MPa
Fatigue damage	2.34e-7	2.84e-7

6.2 Comparison of stress ranges

6.2.1 Time traces

To get a fair comparison between the different fatigue analyses the time trace generation has to be the same for the different cases. For this reason the frequency grid is 'frozen'. This means that the frequency grid is still irregular but the values remain the same during the comparison. An example of the stress time traces that are generated is shown in Figure 6.6.

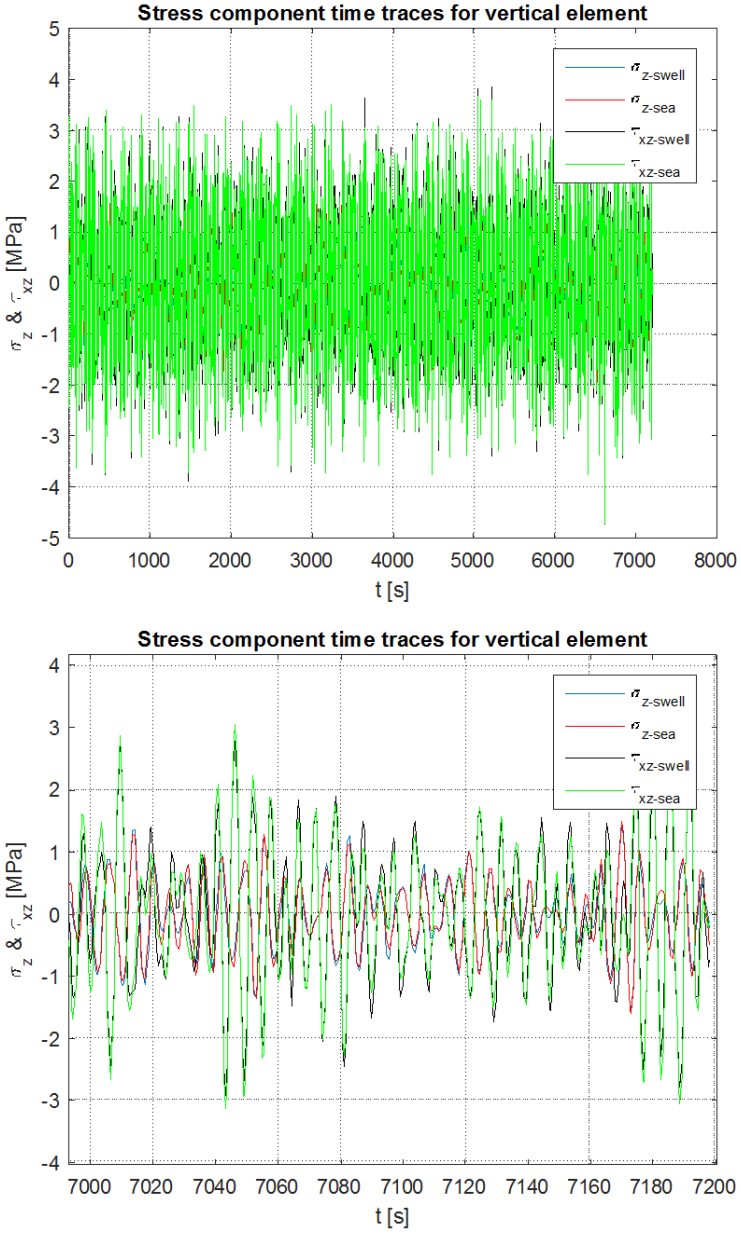

FIGURE 6.6: Stress time traces for the different components

6.2.2 Histograms for multiple cases

Because each component has its own SN curve the differences between the fatigue analyses can best be shown by comparing the stress ranges per cycle after the counting procedures. The amount of cycles per category of stress ranges is plotted in histograms for different load cases. Also the corresponding $\sigma - \sqrt{3}\tau$ plot is given to see the proportionality for each case.

TABLE 6.5: Categories of stress ranges for the histograms

Category	**Stress ranges in [MPa]**
1	< 1
2	1 - 2
3	2 - 3
4	3 - 5
5	5 - 10
6	10 - 15
7	15 - 20
8	> 20

The input is with sea states for both swell and wind sea of $H_s = 1.5m$ and $T_p = 6s$ where both components are coming from 90deg wave direction. The stress range histograms, for the normal and shear stresses and for the equivalent stresses, and $\sigma - \sqrt{3}\tau$ plot are given for three different elements connected to the weld, two vertical elements and one horizontal element respectively. The results are shown in Figures 6.7 to 6.9.

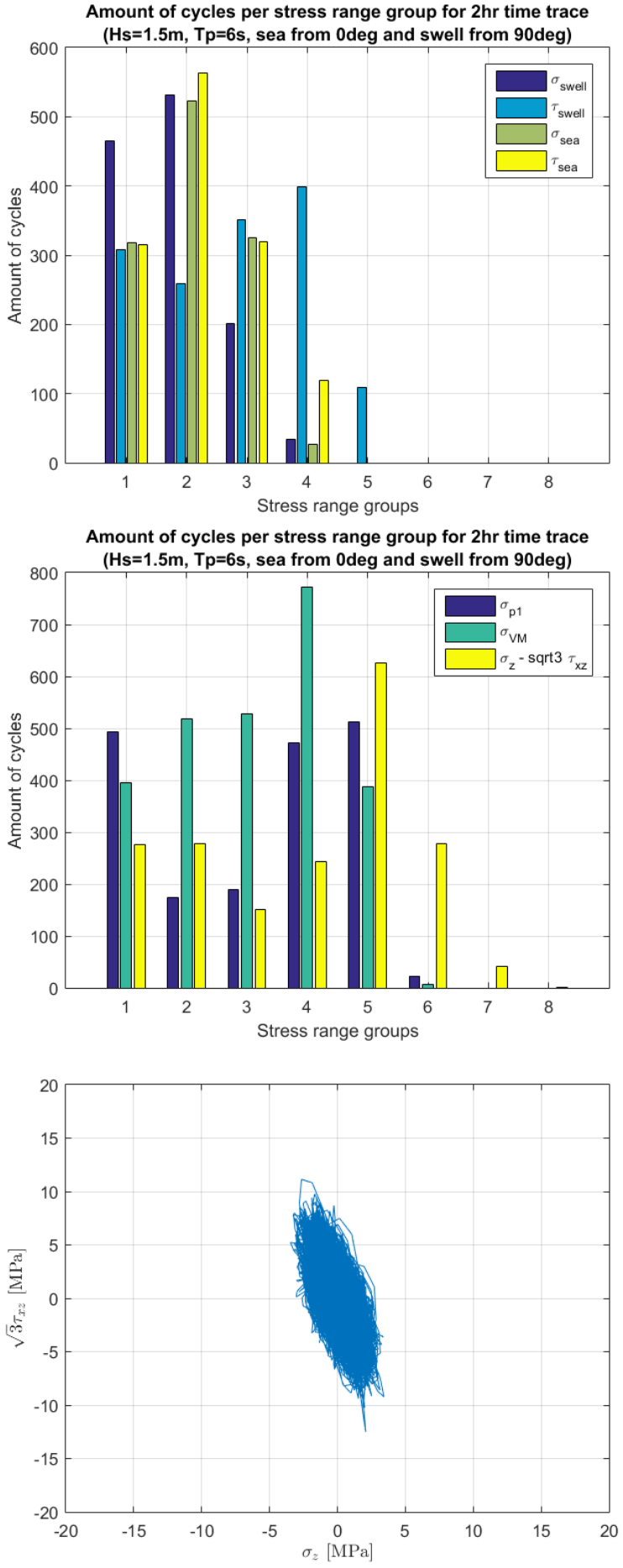

FIGURE 6.7: Stress range histogram for vertical element 10843

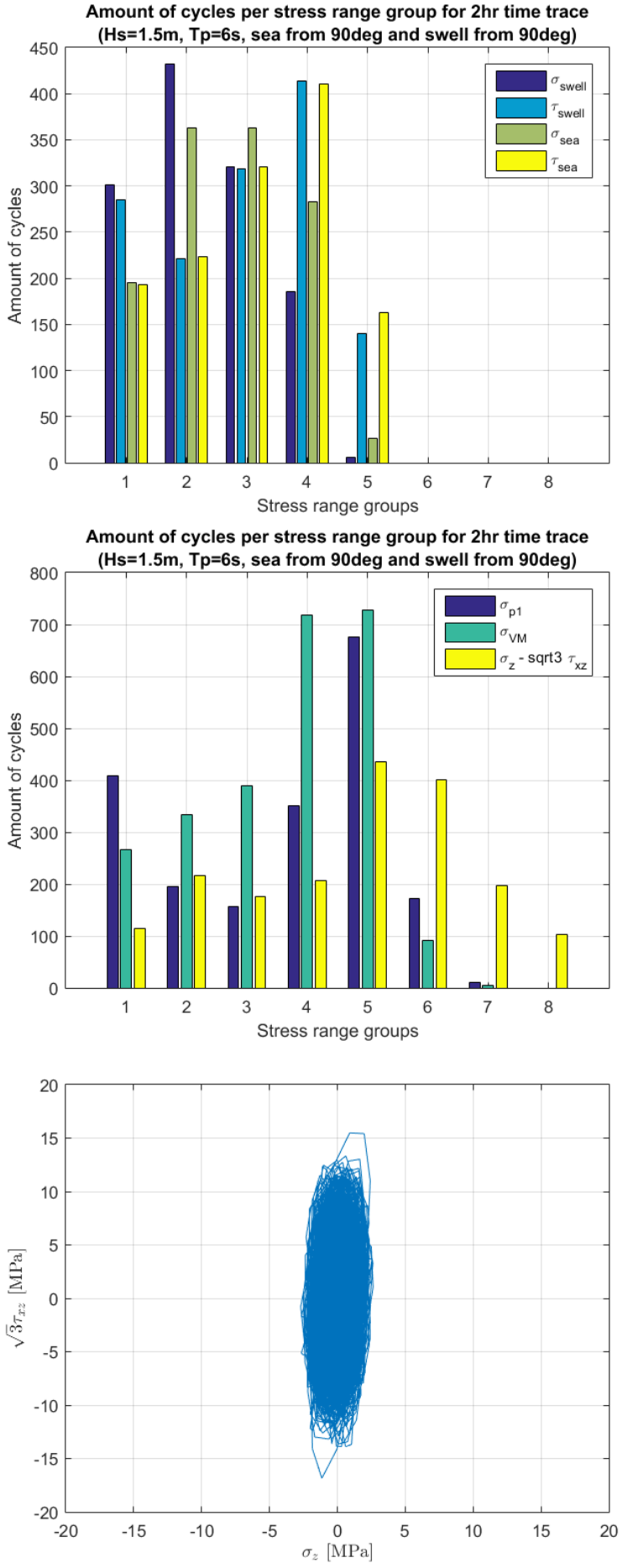

FIGURE 6.8: Stress range histogram for vertical element 10844

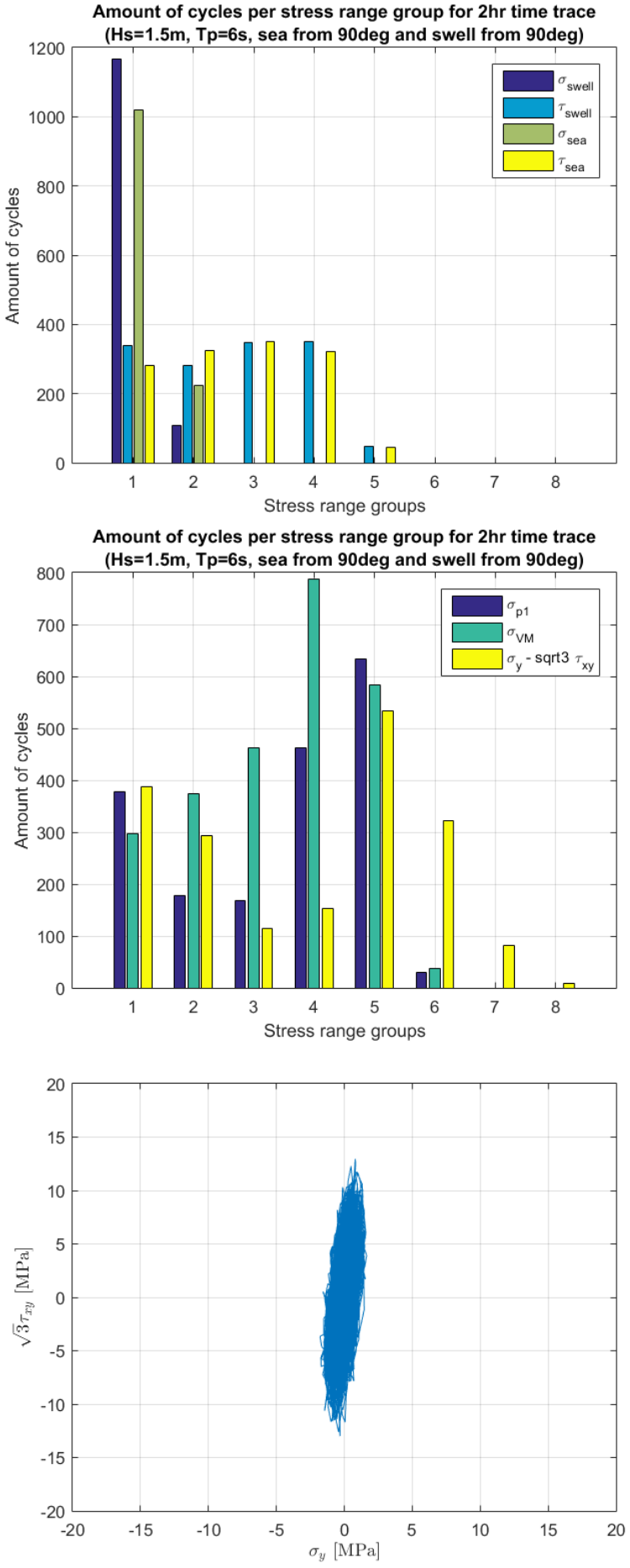

FIGURE 6.9: Stress range histogram for horizontal element 48866

6.3 Fatigue damage factor

6.3.1 Different sea states

From the stress ranges per counted cycle the fatigue damage can be determined. This is done by relating the stress ranges to the amount of cycles that are obtained from the corresponding SN curve. The fatigue damage is first determined for a vertical element connected to the weld for $T_p = 6s$, swell and wind sea coming from 90deg wave direction and multiple values for H_s are considered. The frequency grid remains the same as was the case in the previous computations, however the normal stress components from swell and wind sea are now added as well as the shear stress components.

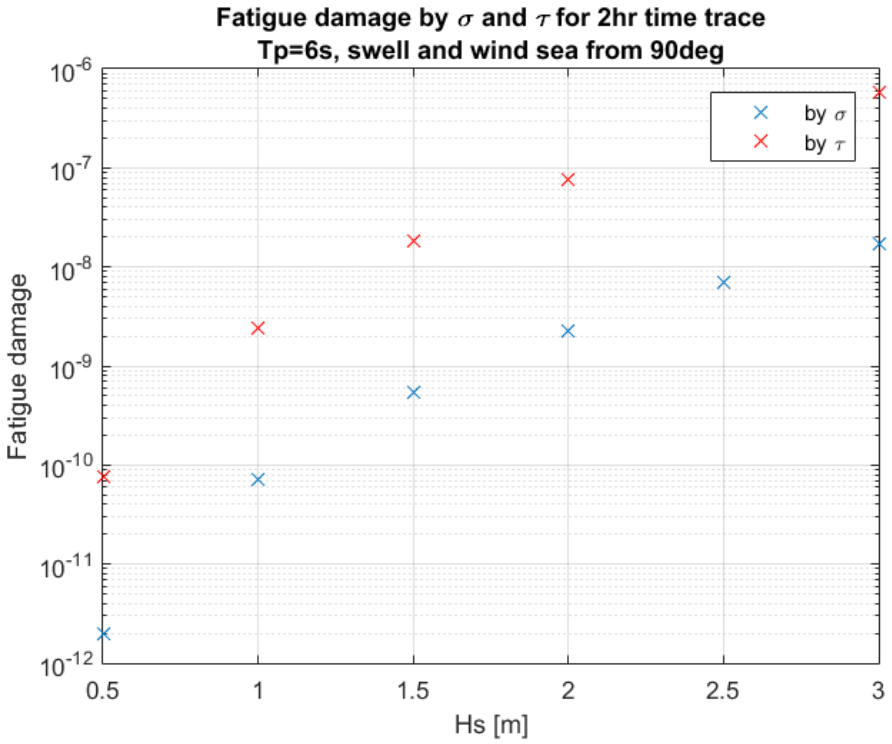

FIGURE 6.10: Fatigue damage related to the significant wave height

6.3.2 Comparison of fatigue damage factors

Varying wind sea direction

The absolute value of the stresses retrieved from the FEM model are not accurate enough for a fatigue analysis. Because it is about a qualitative comparison between different fatigue analyses the actual fatigue damage is not determined. Instead of the fatigue damage a fatigue damage factor is determined. This is done by using only one SN curve

for all the different fatigue analyses. The SN curve which is used is the class E defined in chapter 5. The results presented in this chapter are already normalized (load case with both swell and wind sea from 90deg is considered unity), the actual values for the fatigue damage factor are given in Appendix F.

The swell is considered to come from 90deg wave direction. The wind sea is able to come from different directions based on the averaged direction per 6hr time step. Here the comparison is made between four cases of the fatigue damage factor after 2hr. For each case the wind sea is coming from a different direction, as seen in Figure 6.11. The results are summarized in Tables 6.6 and 6.7.

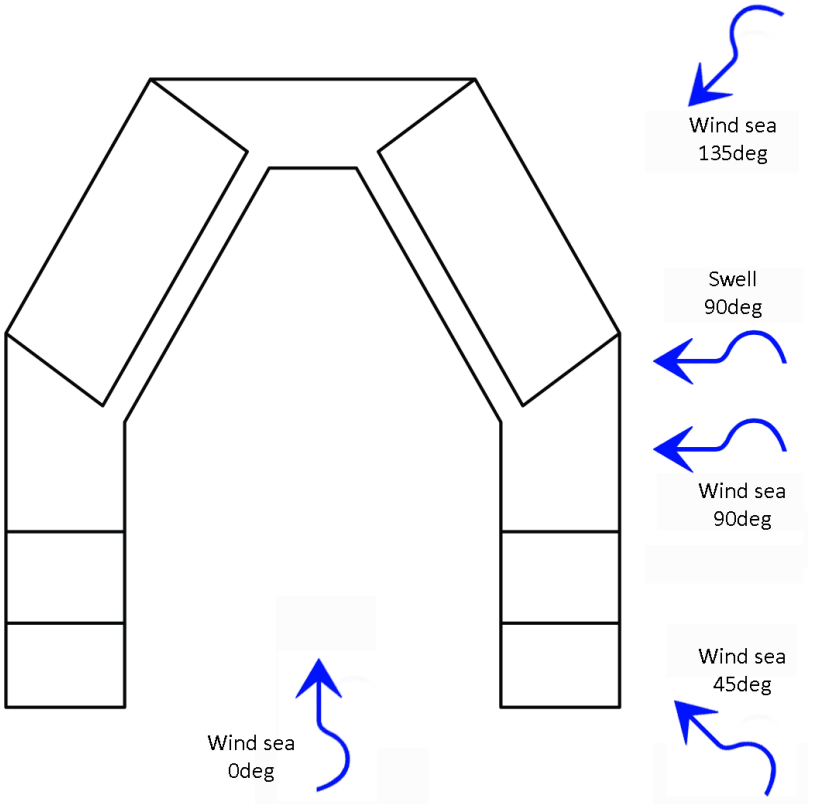

FIGURE 6.11: Possible combinations of swell and wind sea directions

TABLE 6.6: Percentage of sum for 2hr for different wind sea directions

Stress component	**Wind sea 0deg**	**Wind sea 45deg**	**Wind sea 90deg**	**Wind sea 135deg**
σ_{swell}	2.5%	0.2%	1.3%	1.9%
τ_{swell}	87.2%	6.6%	45.1%	65.3%
σ_{sea}	3.2%	0.2%	1.6%	0.0%
τ_{sea}	7.2%	93.0%	52.1%	32.8%

TABLE 6.7: Normalized fatigue damage factors after 2hr for different wind sea directions

Fatigue damage factor	**Wind sea 0deg**	**Wind sea 45deg**	**Wind sea 90deg**	**Wind sea 135deg**
$Df_{\sigma_{p1}}$	0.3	0.5	1.0	0.2
$Df_{\sigma_{vm}}$	0.2	1.2	0.7	0.3
$Df_{\sigma-\sqrt{3}\tau}$	3.1	39	13	5.6

Comparison of vertical elements

There are multiple elements connected to the weld. Here the fatigue damage of two adjacent vertical elements are compared. The loading conditions are the same as used before, $H_s = 1.5m$, $T_p = 6s$ and both swell and wind sea are coming from 90deg wave direction.

TABLE 6.8: Percentage of sum for 2hr for different vertical elements

Stress component	**Element 10843**	**Element 10844**
σ_{swell}	1.3%	4.8%
τ_{swell}	45.1%	39.0%
σ_{sea}	1.6%	10.2%
τ_{sea}	52.1%	46.0%

TABLE 6.9: Normalized fatigue damage factors after 2hr for different vertical elements

Fatigue damage factor	**Element 10843**	**Element 10844**
$Df_{\sigma_{p1}}$	1.0	1.6
$Df_{\sigma_{vm}}$	0.7	0.9
$Df_{\sigma-\sqrt{3}\tau}$	13	24

Vertical vs horizontal element

Besides the vertical elements there are also horizontal elements connected to the weld. As stated before these horizontal elements are related to different SN curves due to the configuration of the fillet weld. Therefore also a horizontal element is compared to a vertical element under the same loading conditions used for the comparison between vertical elements.

TABLE 6.10: Percentage of sum for 2hr for a vertical and horizontal element

Stress component	**Element 10843**	**Element 48866**
σ_{swell}	1.3%	0.2%
τ_{swell}	45.1%	52.4%
σ_{sea}	1.6%	0.1%
τ_{sea}	52.1%	37.3%

TABLE 6.11: Normalized fatigue damage factors after 2hr for a vertical and horizontal element

Fatigue damage factor	**Element 10843**	**Element 48866**
$Df_{\sigma_{p1}}$	1.0	0.4
$Df_{\sigma_{vm}}$	0.7	0.4
$Df_{\sigma-\sqrt{3}\tau}$	13	5.7

Chapter 7

Discussion

In this chapter the method to get to the results and the results from Chapter 6 are discussed. First the general discussion points about different steps in the method are discussed. Then the value of the results is discussed.

7.1 Discussion on method

7.1.1 Absolute stress values

The accuracy of the absolute stress values is of importance for the fatigue analysis. A small change in the determination of the (high) stress ranges can have a relatively large impact on the fatigue damage due to the relation of the SN curves. In this thesis there are multiple ways to increase the accuracy of the determined absolute stress values. Because in the end a comparison is made between different fatigue analyses the influence of the absolute stress values is assumed not critical for the outcome.

Optimize structural design

The design used in this thesis is a preliminary design. Structural members and geometry should be improved to reduce stress concentrations. The braces should be relocated to find an optimum and the cross section should be varied to find an optimum to. Furthermore the hard edges in the structure should be reduced as much as possible to reduce the amount of stress concentrations in the structure. Certain parts of the structure should be reinforced due to high local loading. For example the top of the columns at which the gravity based wind turbine will be connected. Also at locations where machinery and equipment will be added.

Equivalent plate for stiffeners

The way the stiffeners are modeled in the global FEM model is like this: the cross section area of the stiffeners on a plate is added to the cross section area of that plate. This gives a too high bending stiffness of the plate in the perpendicular direction of the stiffeners. To get more accurate stress results the model should contain an orthotropic plate value. By using that approach other material properties should be corrected to maintain realistic material behavior. Another way to model the stiffeners would be to use beam elements.

Local FEM model

A relatively coarse mesh is used in the FEM model. To get more accurate results for the absolute stress results a finer mesh should be used. Using a local FEM model is required for engineering. This local FEM model could also consist of plate elements. The accuracy would again improve if beam elements are used for the stiffeners. The most accurate results would be retrieved when solid elements are used. Also the weld itself can be modeled by using solid elements.

7.1.2 Loading on the structure

The loading on the structure also has an effect on the absolute stress values, thus on the fatigue damage. The loading condition due to sea state limits is based on a preliminary timeline. This gives an incomplete fatigue exposure time.
Because in this thesis a multiaxial fatigue analysis is considered the phase relation between the different loading components is essential. This phase relation is clearly present in the thesis but might change due to wave directionality.

Fatigue exposure time

Now only the unloaded unit at floater draft is considered in the fatigue damage calculation. For more detailed fatigue damage also the loaded unit should be considered. This will increase the total fatigue damage due to increased exposure time, thus more stress range cycles.
The unloaded floater draft exposure time is considered conservative because for relative long waiting times in the operation timeline the unit will submerge or be towed away to reduce the loading on the structure.

Wave directionality

In the data used the wave direction is kept constant for each 6 hour period. In reality this is not the case, the waves will keep changing direction over time and will vary around a certain average direction during these 6 hours. This average direction is used in the data for this thesis.

7.1.3 Counting methods

Difference rainflow and PDMR counting

Rainflow counting a time trace should give the same result as PDMR counting a uniaxial σ-τ plot. As observed in Chapter 6 this is not the case for the PDMR procedure in this thesis. It is expected that the effective stress ranges from the PDMR counting method are higher than the stress ranges from the rainflow counting method. For the uniaxial case it is observed that the fatigue damage is smaller for the PDMR. Therefore it is considered a conservative error. This means that if in the final results the fatigue damage due to PDMR is higher that it is assumed that the error is not the cause.
The reason it is expected the effective stress ranges counted by PDMR are higher is because the path length is considered instead of the path range. The length can be an arc which will always have more length than the shortest distance (range).

7.1.4 Physical explanation of difference in fatigue analysis

Crack growth under multiaxial stresses

Experiments by N. Shamsaei and A. Fatemi [21] show that the crack length for a certain amount of cycles is larger for material under multiaxial stresses. It can also be seen that for a tensile normal stress the crack growth is larger than for a compressive normal stress. If this normal stress is combined with a shear stress the crack growth rate is increased. In Figure 7.1 the uniaxial case for K and L is shown and then the multiaxial case for F and G is shown. The multiaxial cases have higher crack growths.
This is explained by the combination of stresses acting on the crack. If only a shear stress is acting on the crack, the crack surfaces are touching each other permanently and there is friction which decelerates the crack growth process. If there is a tensile normal stress and a shear stress acting on the crack, the crack opens and there is less friction which accelerates the crack growth process [22].

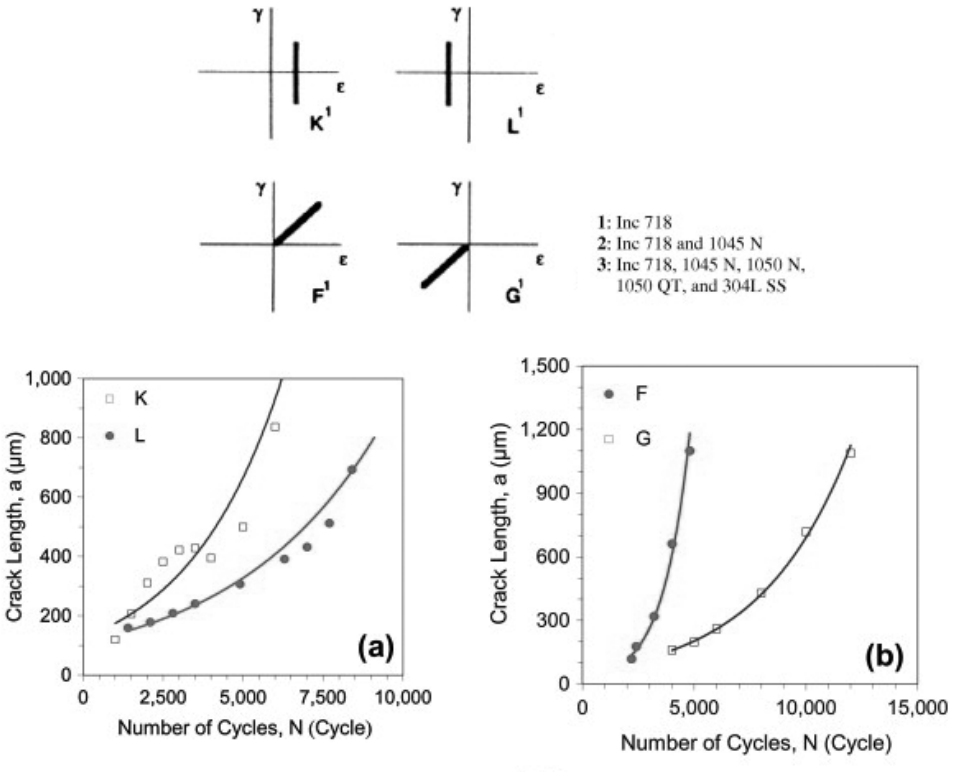

FIGURE 7.1: Crack growth comparison for uniaxial vs multiaxial

From the results of this thesis it can also be observed that the fatigue damage factor of the sum of the individual components is smaller than for the cases where the stresses are combined either as an equivalent stress or by using the PDMR method.

Crack growth under non-proportional loading

Mixed-mode fatigue crack growth behavior may be affected by load non-proportionality. Experiments by N. Shamsaei and A. Fatemi [21] also show that the crack length for a certain amount of cycles is larger for material under non-proportional loading. It can be seen that there is a dependency on the material considered, the bottom graphs in Figure 7.2 are for a different material. In Figure 7.2 the proportional case for C is shown and then the non-proportional case for N is shown. The non-proportional case has a higher crack growth.

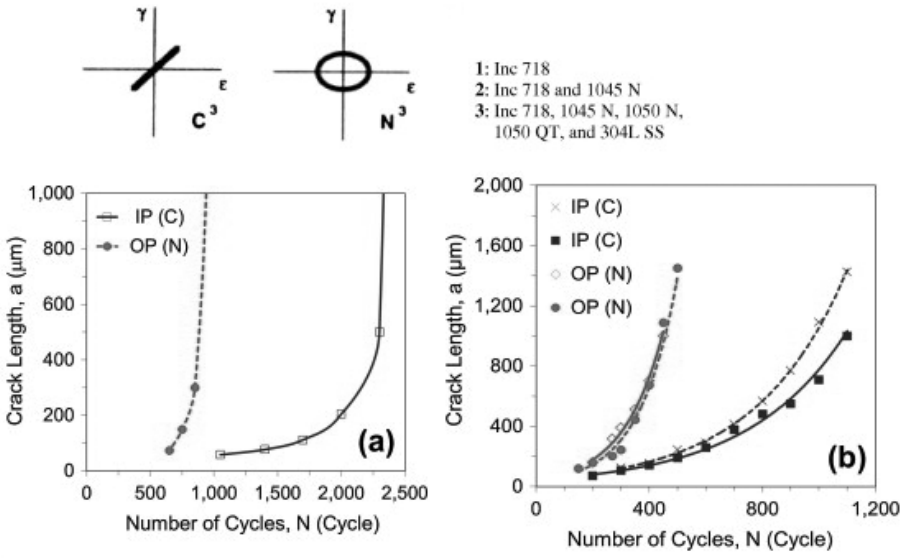

FIGURE 7.2: Crack growth comparison for proportional vs non-proportional

From Figure 7.3 it can be seen that the proportionality for the four cases is quite similar, however the amplitudes of the components are not. It is not directly clear to see the relation with the fatigue damage factor here.

7.1.5 Fatigue damages

SN curves

For the different stress components different SN curves are used. For the normal and shear stresses, for both wind sea and swell, the SN curves are based upon experiments related to either nominal or structural stresses. The master SN curve is based upon a lot of experiments and uses an equivalent stress related to the structural stress. The structural stress is higher than the nominal stress because of a stress concentration factor.

In this thesis a stress concentration factor has not been applied. Therefore if all the corresponding SN curves were used the stress ranges used for the results of the Von Mises and PDMR fatigue damage would be higher. This leads to higher fatigue damages as well.

7.2 Discussion on results

7.2.1 Rainflow vs PDMR for uniaxial stress

For both of the cases σ and τ equal to zero a difference between the counted cycles and stress ranges is observed. For the short time trace this leads to a difference in fatigue damage of 6.2% for τ is zero and 1.35% for σ is zero. This difference can be explained by the algorithm of the PDMR counting. In the process of removing counted paths from the $\sigma - \sqrt{3}\tau$ plot, in certain situations some parts of the path remains. This leads to small differences in the effective stress ranges that correspond to half cycles. The 'bug' in the algorithm will have a bigger effect on a longer time trace. For the 2hr time trace this leads to a difference in fatigue damage of 13.6% for τ is zero and 17.6% for σ is zero.
From the tables and histogram plots it can be seen that the PDMR counting has more counted cycles than the rainflow counting. However the cumulative fatigue damage is less in both cases. This is explained due to more cycles that correspond to a lower stress range, which contribute significantly less to the fatigue damage. This can also be concluded from the mean stress ranges given in the tables.
In both of the cases σ and τ equal to zero the fatigue damage is higher for the rainflow counting method. Because it is expected that in the final result the fatigue damage due to the PDMR counting method will be higher, this 'bug' is considered to be on the optimistic side.

7.2.2 Comparison of stress ranges

From the histogram plots it can directly be seen that for the higher stress range groups the amount of cycles counted by PDMR are significantly higher. All the stress time traces counted with the rainflow method show more counted cycles for the lower stress range groups. It can be seen that both σ_{p1} and σ_{VM} have more counted cycles. This is related to the fact that these are equivalent stresses. Another observation is that the shear stresses have more cycles in the higher stress range groups.
The fatigue damage is dependent on the SN curves, the dominant parameter in the SN curves is the stress range. As a first observation the normal stresses will contribute the least to fatigue damage and the shear stresses the most. It can also directly be seen that there will be more fatigue damage by $\sigma - \sqrt{3}\tau$ method.
From the proportionality plots it can be seen that the horizontal element has a more proportional, almost uniaxial, loading. It also has more counted cycles than the vertical

elements which have a more non-proportional loading, especially for normal stresses in the smallest stress range group. This can be explained by the small amplitude of σ_y.

7.2.3 Fatigue damage

Swell and wind sea components

By increasing the significant wave height H_s the fatigue damage also increases. This is logical since the higher waves will cause more pressure on the structure as well as higher inertia loads.

The contribution of shear stress to fatigue damage is significantly higher for the considered fillet weld. The stress ranges of the shear stress components are higher, the reason for this is the combination of the wave loading and the shape of the structure. Apparently the transverse shear and torsion at the weld due to the wave loading is higher than the bending and compression/tension.

From the results for combining swell and wind sea from different directions the contribution of each of the components can be determined, as shown in Table 6.6. The corresponding proportionality plots for the sum of normal stress components and the sum shear stress components are shown in Figure 7.3.

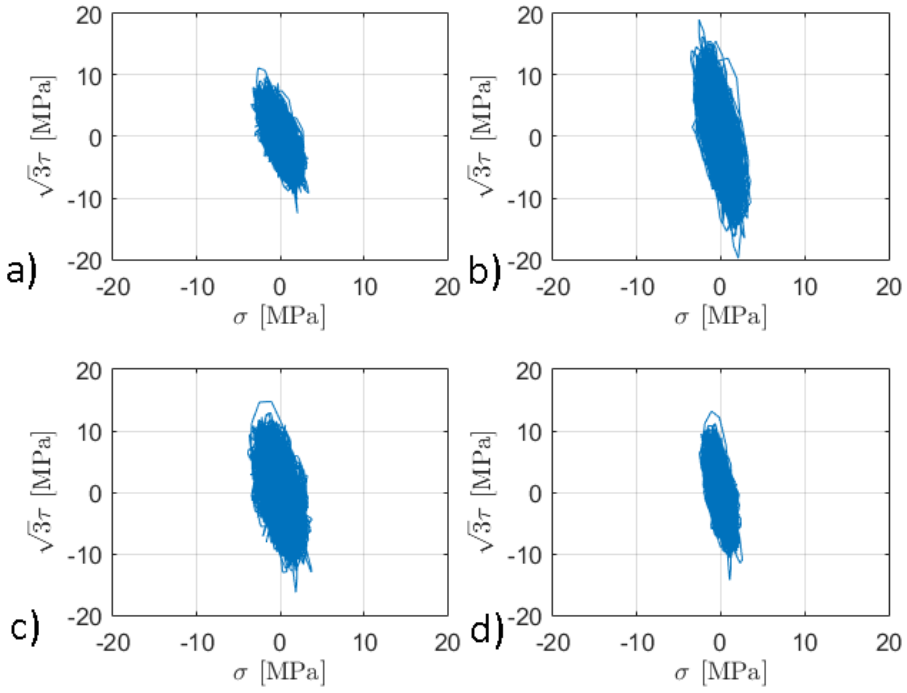

FIGURE 7.3: Proportionality plots: a) 0deg b) 45deg c) 90deg d) 135deg

Comparison of fatigue analyses

From the results for combining swell and wind sea from different directions the comparison between the common practice fatigue analysis and the multiaxial fatigue analysis can be made. This is done by relating the fatigue damage factors found by the PDMR counting of $\sigma - \sqrt{3}\tau$ to the fatigue damage found by rainflow counting the maximum principal stress σ_{p1} in Table 6.7. The same factor can be determined for the comparison between vertical elements and horizontal element, which is shown in Tables 6.9 and 6.11. Here both the wind sea and swell are coming from 90 degrees wave direction.

As can be seen from Tables 6.7, 6.9 and 6.11 the fatigue damage factor due to the multiaxial approach is higher up to a factor of $\frac{39}{0.5}$.
Another interesting relation is observed when relating Table 6.7 to Table 6.6. When the percentage of shear is increasing the fatigue damage factor increases. This is both in absolute value and when the multiaxial fatigue approach ($\sigma - \sqrt{3}\tau$) is related to the common practice fatigue(σ_p) approach.

Chapter 8

Conclusions & Recommendations

The conclusions in this chapter are directly related to the results and discussion given in the previous chapters. For each of these results one or more conclusions are drawn. Also some recommendations are given for the continuation and improvement of the comparative analysis in this thesis.

8.1 Conclusions

The multiaxial fatigue analysis, consisting of PDMR counting the normal stress perpendicular to the weld and the shear stress along the weld, is a more conservative fatigue analysis.
The fatigue damage factor determined in this thesis between the common practice fatigue analysis and the multiaxial fatigue analysis is between 10 and 80. To get a more accurate results a more extensive and detailed research should be done, recommendations are given later in this chapter.

The PDMR counting method is more accurate than the rainflow counting method when considering simultaneous (multiaxial) loading.
The PDMR counting method is considered more accurate because it can get the same results for a uniaxial loading as rainflow counting. On top of that PDMR is also able to count when the loading is simultaneous and multiaxial, taking into account the phase relation between normal and shear stress. Thus it considers the effect of shear when the crack is pulled open by a simultaneous tensile load. Therefore the shear will face less friction.
A higher normal stress on the maximum shear plane for out-of-phase loading as compared to in-phase loading can explain the observed higher crack growth rate due to

out-of-phase loading.
In plate-type geometries under multiaxial stresses, cracks often form under mixed-mode loading; however, they usually turn into a mode I (4.7) macro-crack soon after micro-crack growth [21].

For the welded joint considered for this particular installation unit structure the shear stresses are dominant with regard to fatigue damage.
The fact that the fatigue damage is shear driven has effect on the crack growth rate and thus on the fatigue damage. Since it is shear driven for all the cases considered it has no significant effect on the overall conclusions.

8.2 Recommendations

With the knowledge gained from this thesis, from the literature and the results and conclusions, recommendations are given.
Failure due to fatigue can be minimized by avoiding as much stress concentrations as possible in the structure. If there are fatigue hot spots in the structure then it is recommended to do a multiaxial fatigue analysis because it is shown to be more conservative than common practice fatigue analyses.

A list of recommendations regarding the continuation of this thesis:

- Improve the structural design
- Improve the global FEM model
- Create a local FEM model
- Remove small error from the PDMR counting algorithm
- Include gravity based wind turbine in the fatigue analysis
- Check motions of the installation unit on scale in an experiment
- Check more fatigue hot spots on the installation unit
- More SN curves are needed, especially for multiaxial loading

Appendix A

Gravity based wind turbine specifications

The gravity based foundation used in this thesis is a design by Strabag [23].

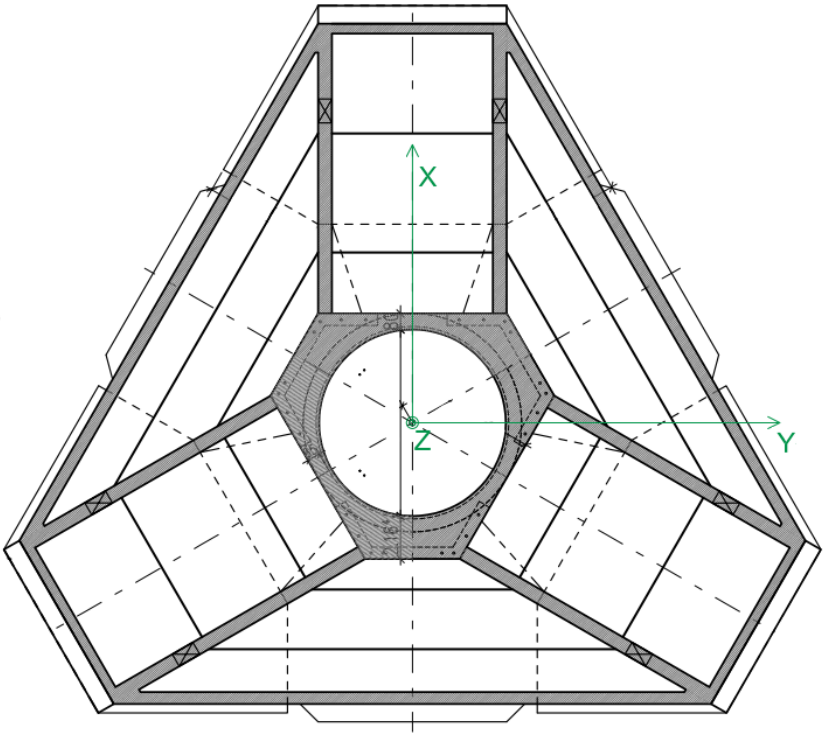

FIGURE A.1: Gravity based foundation

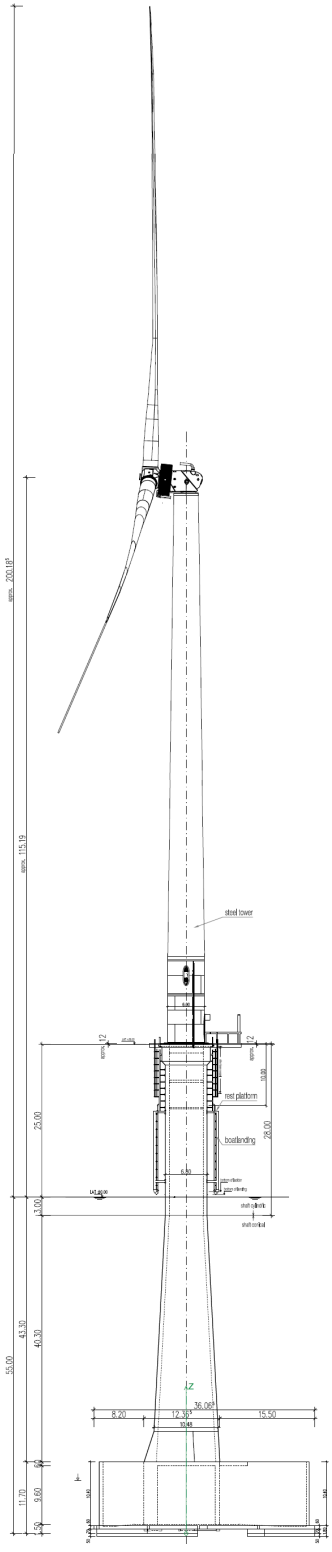

FIGURE A.2: Wind turbine

Mass distribution

Location z [m]	Mass [t]	Comments
4.54	7,097	Foundation base
30.33	1,869	Conical Schaft
53.50	104	Cylindrical shaft unter w ater line
67.50	864	Cylindrical shaft above w ater line
49.16	386	Other components
87.12	128	Steel tow er section 1
109.63	207	Steel tow er section 2
145.93	137	Steel tow er section 3
169.61	504	Wind energy converter
Sum Σ =	**11,295**	

Center of mass

z = 27.53 m

Mass inertia tensor in relation to center of mass in [t·m²]

$$\Theta^{(CM)} = \begin{bmatrix} \Theta_x & \Theta_{xy} & \Theta_{xz} \\ \Theta_{yx} & \Theta_y & \Theta_{yz} \\ \Theta_{zx} & \Theta_{zy} & \Theta_z \end{bmatrix} = \begin{bmatrix} 2.008E+07 & -9.776+01 & 2.154E+03 \\ -9.776E+01 & 2.007E+07 & 3.323E+05 \\ 2.154E+03 & 3.323E+05 & 1.389E+06 \end{bmatrix}$$

CM = Center of mass

FIGURE A.3: Wind turbine mass distribution and mass inertia tensor

Appendix B

Initial design

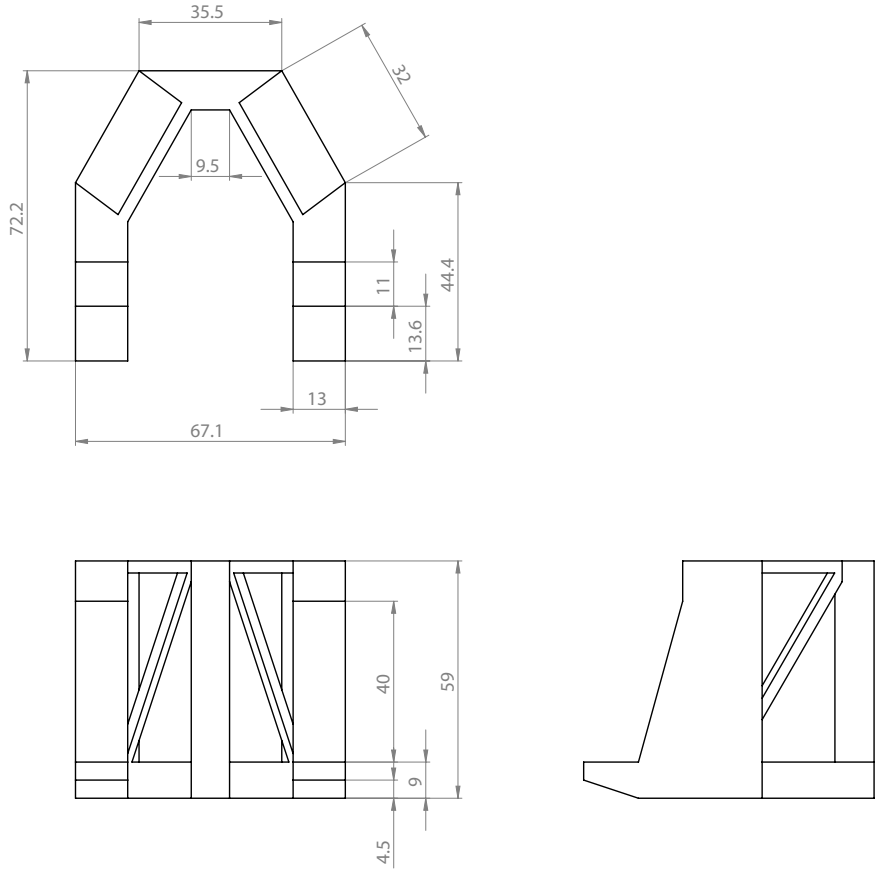

FIGURE B.1: Initial design dimensions in meter

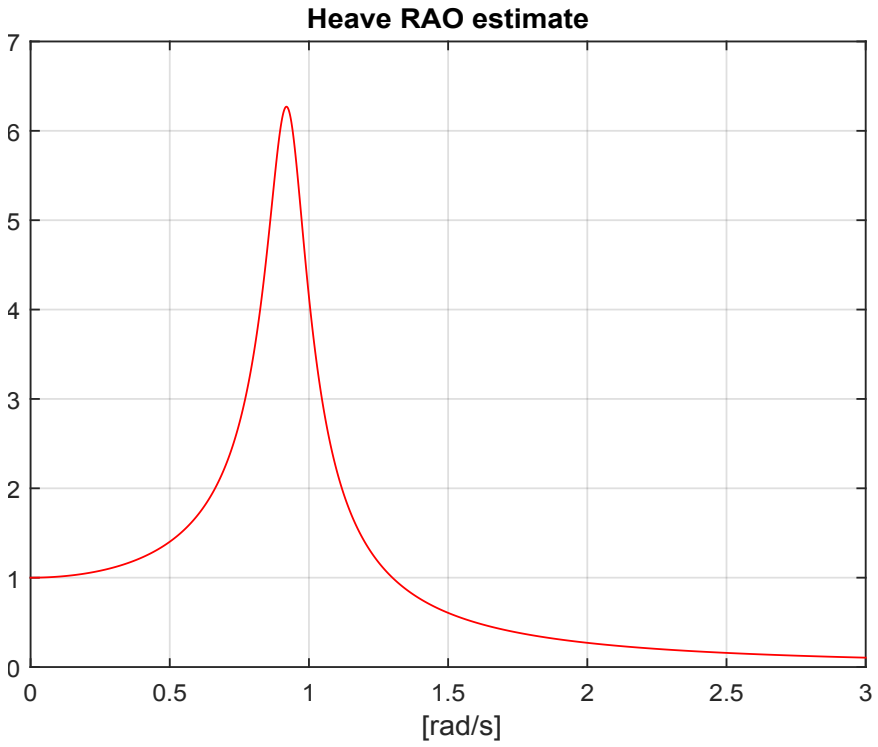

FIGURE B.2: Heave RAO estimate of unloaded unit

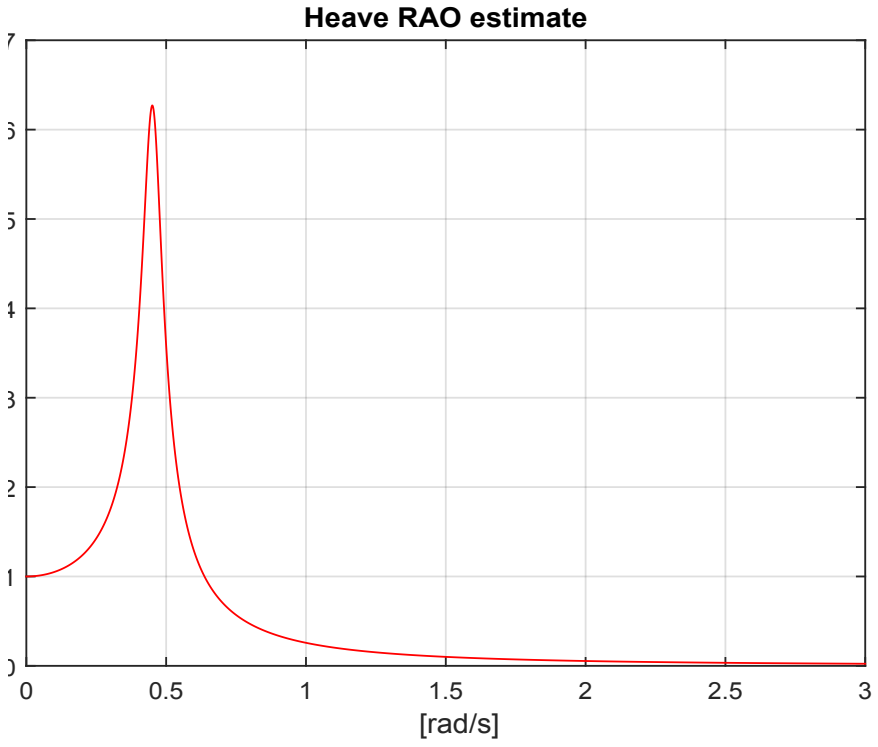

FIGURE B.3: Heave RAO estimate of loaded unit

Appendix C

Wave length - Wave period

The information in this Appendix is from DNV Rules and Regulations-RP-C205.
The dispersion relationship gives the relationship between the wave period T and the wave length λ. An accurate approximation is given by:

$$\lambda = T\sqrt{g * d} * \sqrt{\frac{f(\omega)}{1 + \omega * f(\omega)}} \tag{C.1}$$

in which:

$$f(\omega) = 1 + \alpha_1 * \omega + \alpha_2 * \omega^2 + \alpha_3 * \omega^3 + \alpha_4 * \omega^4 \tag{C.2}$$

$$\omega = \frac{4\pi^2 * d}{g * T^2} \tag{C.3}$$

with:

d	water depth	[s]
g	gravitational acceleration	[s]
T	wave period	[s]
α_1	=0.666	[-]
α_2	=0.445	[-]
α_3	=-0.105	[-]
α_4	=0.272	[-]
λ	wave length	[m]

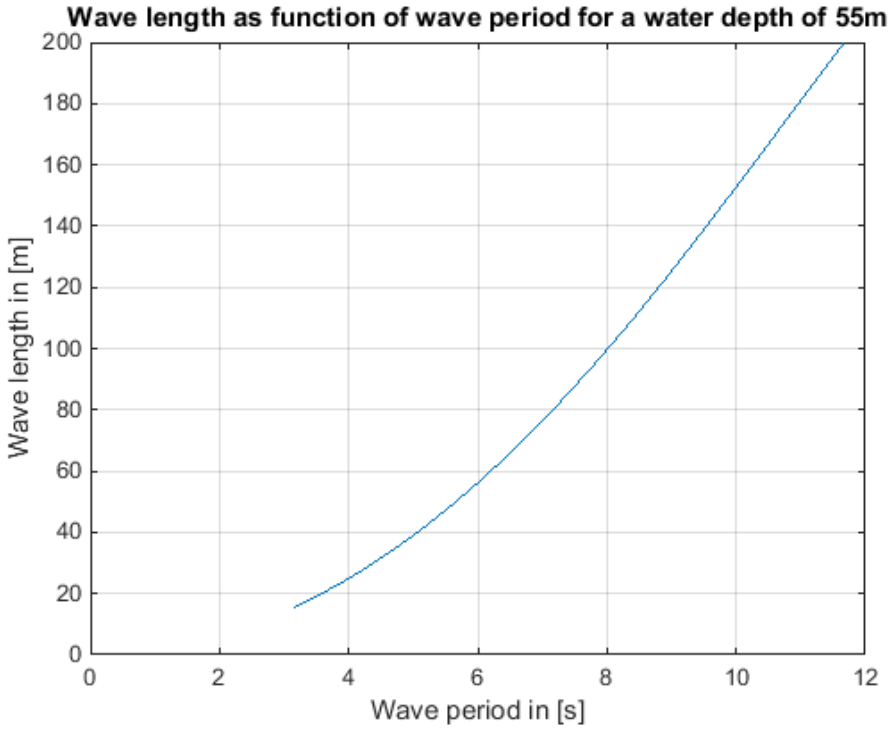

FIGURE C.1: Wave length as function of wave period for 55m water depth

Appendix D

Rainflow cycle counting

An quick way of understanding the rainflow cycle counting method is shown by Figure D.1. The idea is to turn the stress time trace 45deg clockwise and start 'dripping' water on top of the graph. The water will drip down the peaks of the stress time trace. With this approach the tensile and compressive peaks of each half cycle can be counted. The official explanation by ASTM is also given in this Appendix.

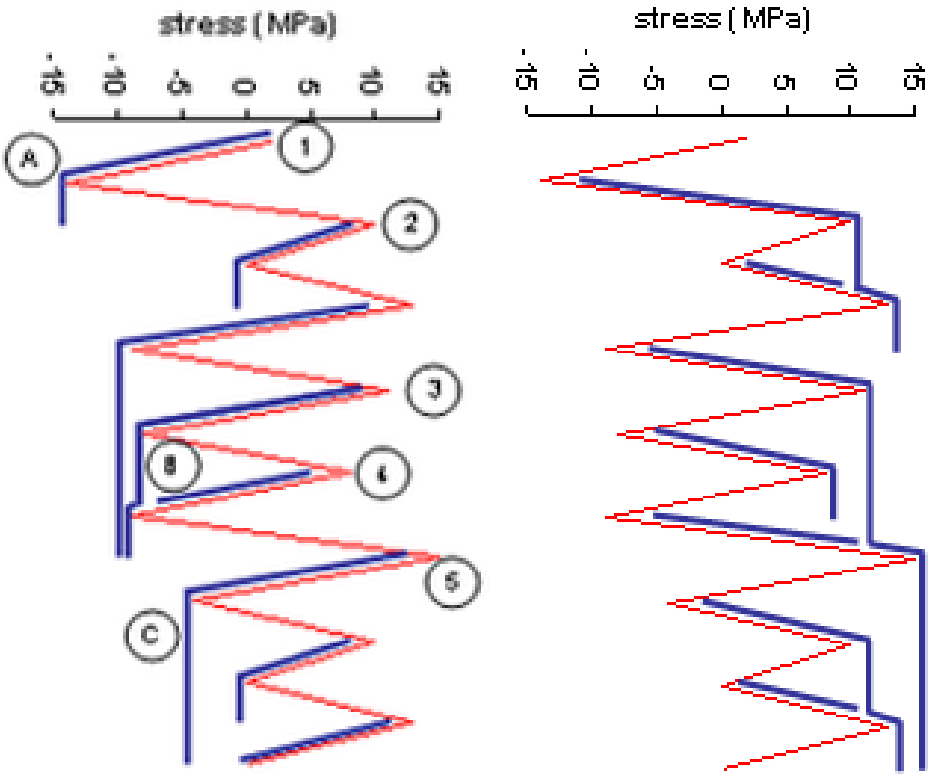

FIGURE D.1: Rainflow counting example

The upcoming information in this Appendix is from ASTM-E1049-85.
Rainflow Counting:
Rules for this method are as follows: let X denote range under consideration; Y, previous range adjacent to X; and S, starting point in the history.

- Read next peak or valley. If out of data, go to Step 6.
- If there are less than three points, go to Step 1. Form ranges X and Y using the three most recent peaks and valleys that have not been discarded.
- Compare the absolute values of ranges X and Y.
  - If X $<$ Y, go to Step 1.
  - If X $\geq$ Y, go to Step 4.
- If range Y contains the starting point S, go to Step 5; otherwise, count range Y as one cycle; discard the peak and valley of Y; and go to Step 2.
- Count range Y as one-half cycle; discard the first point (peak or valley) in range Y; move the starting point to the second point in range Y; and go to Step 2.
- Count each range that has not been previously counted as one-half cycle.

Details of the example cycle counting are as follows (Figure D.2):

- S = A; Y = $|A - B|$; X = $|B - C|$; X $>$ Y. Y contains S, that is, point A. Count $|A - B|$ as one-half cycle and discard point A; S = B.
- Y = $|B - C|$; X = $|C - D|$; X $>$ Y. Y contains S, that is, point B. Count $|B - C|$ as one-half cycle and discard point B; S = C.
- Y = $|C - D|$; X = $|D - E|$; X $<$ Y.
- Y = $|D - E|$; X = $|E - F|$; X $<$ Y.
- Y = $|E - F|$; X = $|F - G|$; X $>$ Y. Count $|E - F|$ as one cycle and discard points E and F. Note that a cycle is formed by pairing range E-F and a portion of range F-G.)
- Y = $|C - D|$; X = $|D - G|$; X $>$ Y; Y contains S, that is, point C. Count $|C - D|$ as one-half cycle and discard point C. S = D.
- Y = $|D - G|$; X = $|G - H|$; X $<$ Y.
- Y = $|G - H|$; X = $|H - I|$; X $<$ Y. End of data.

- Count $|D-G|$ as one-half cycle, $|G-H|$ as one-half cycle, and $|H-I|$ as one-half cycle.
- End of counting.

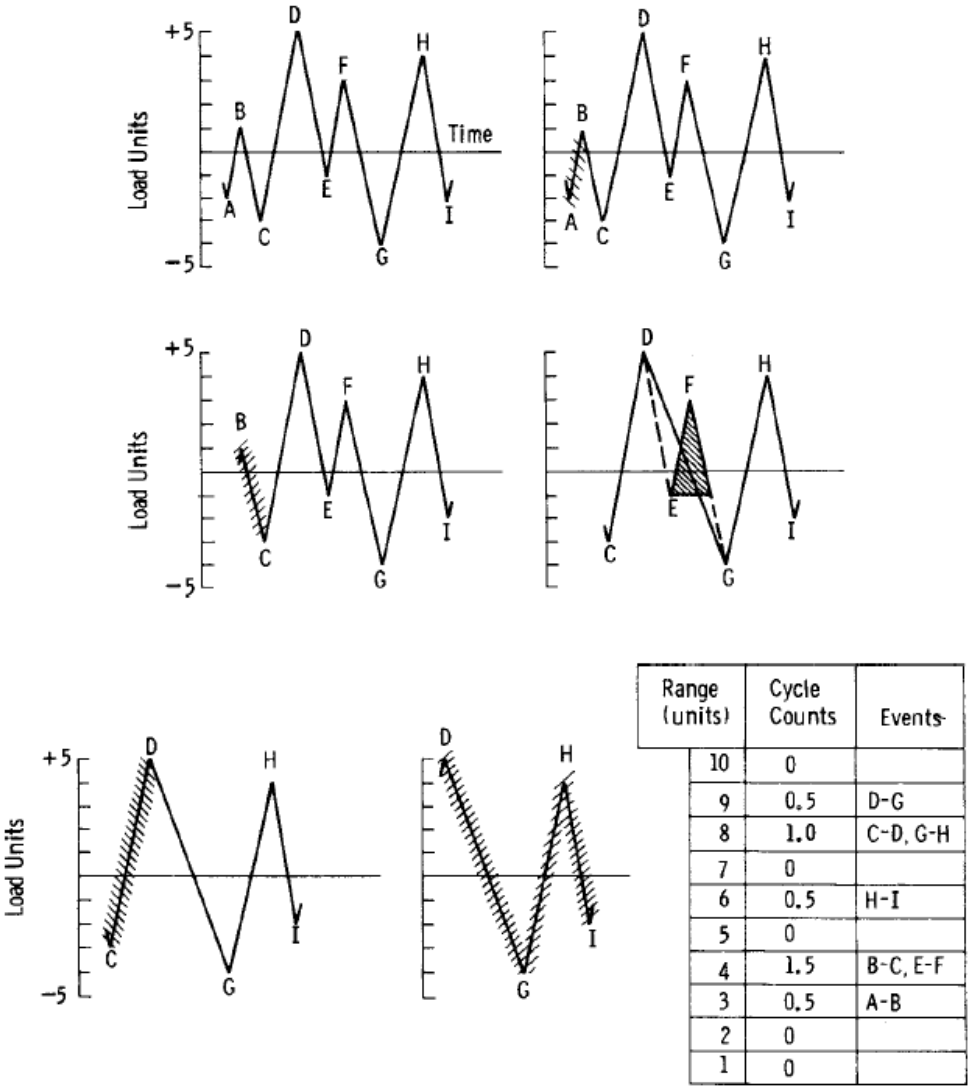

Range (units)	Cycle Counts	Events
10	0	
9	0.5	D-G
8	1.0	C-D, G-H
7	0	
6	0.5	H-I
5	0	
4	1.5	B-C, E-F
3	0.5	A-B
2	0	
1	0	

FIGURE D.2: Rainflow counting example

Appendix E

PDMR cycle counting

In this Appendix an example of one of the $\sigma - \sqrt{3}\tau$ plots is given and the PDMR concept is explained by using images and short explanations.
First the stress time traces and $\sigma - \sqrt{3}\tau$ proportionality plot are given for a vertical element, Figures E.1 and E.2. This mean that the σ_z and τ_{xz} components are analyzed.

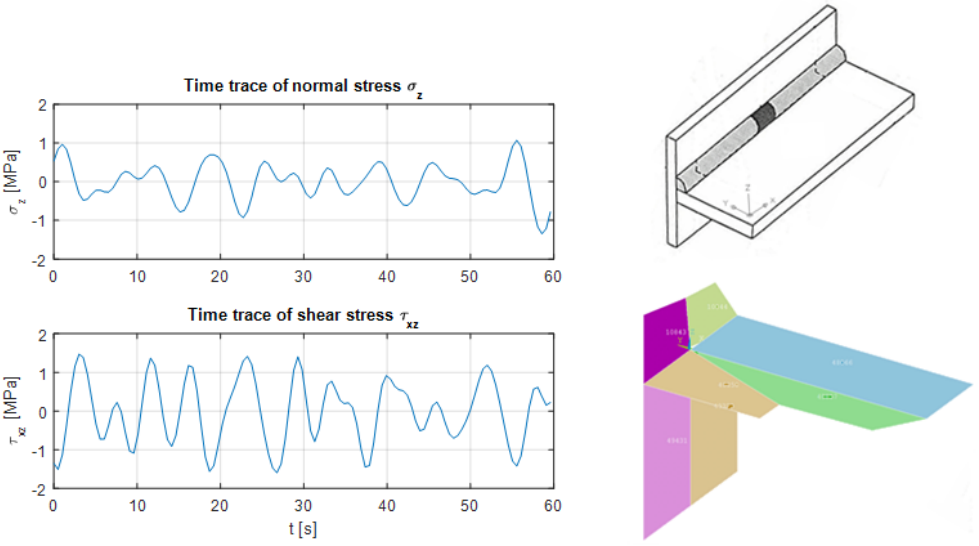

FIGURE E.1: Stress time traces and considered vertical element

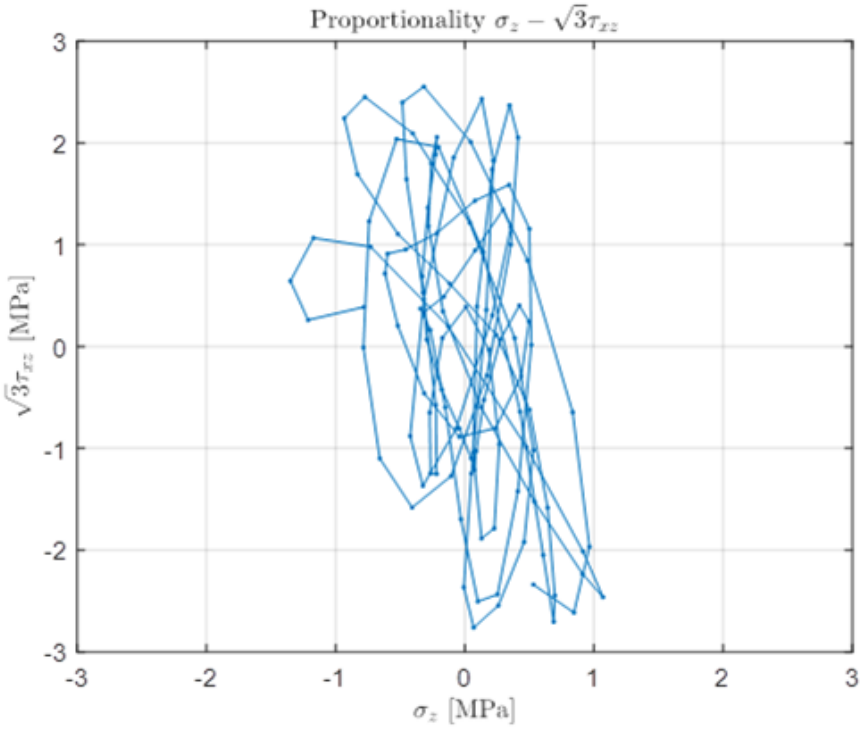

FIGURE E.2: $\sigma - \sqrt{3}\tau$ proportionality plot

The first thing to do is to determine the maximum range within the $\sigma - \sqrt{3}\tau$ proportionality plot. This is done by calculating the shortest distance between each point. The maximum range found for this example is given in Figure E.3.

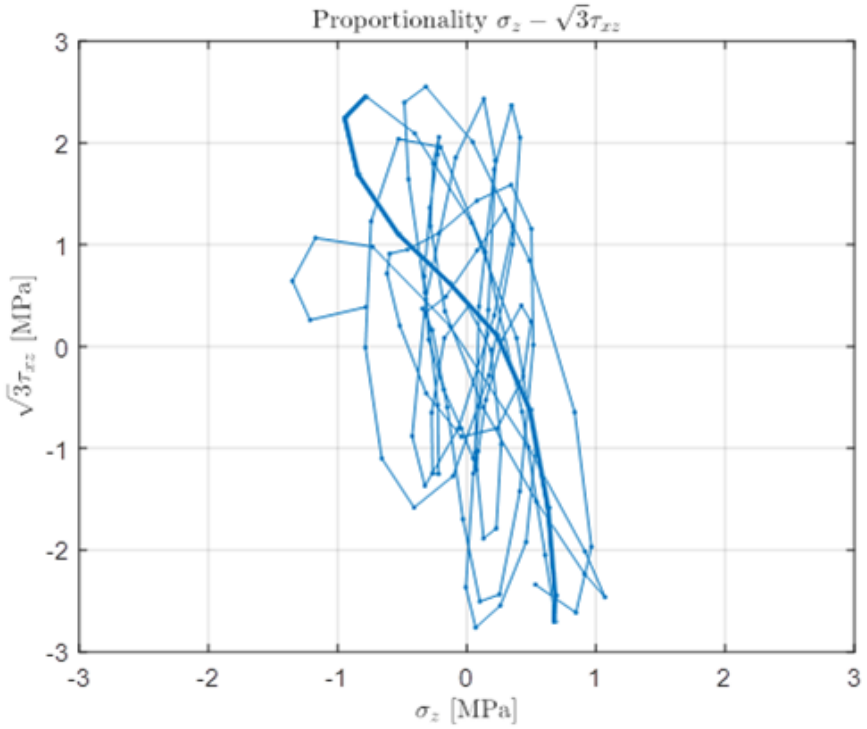

FIGURE E.3: Maximum range

The next step is to check if this maximum range is monotonically increasing. This means if the next data point has a larger range with respect to the first data point than the previous data point. This can be checked by drawing circles around the first data point which coincide with the next data point, see Figures E.4 and E.5.

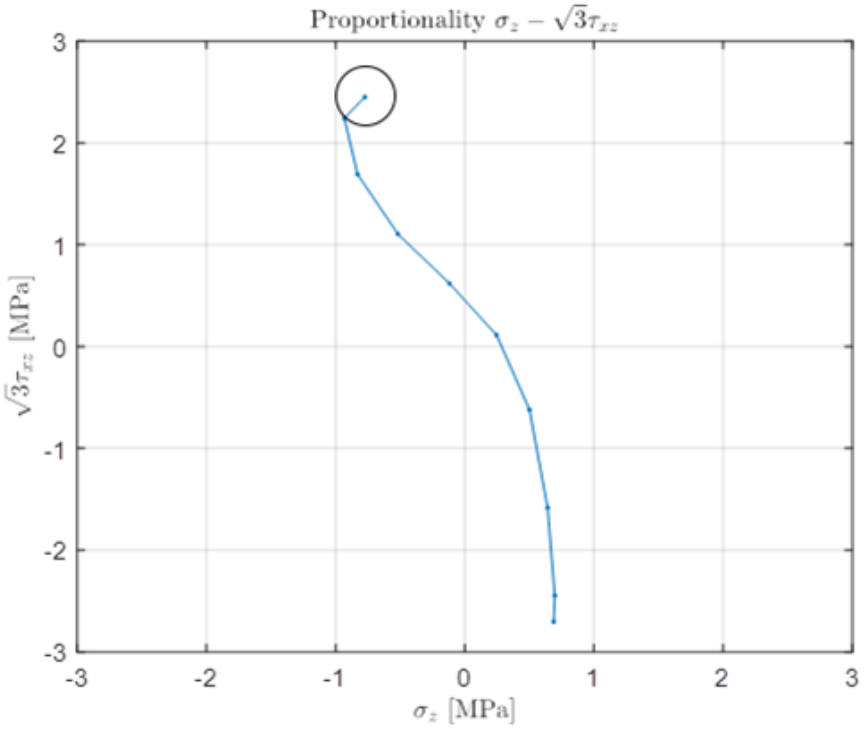

FIGURE E.4: First data point is monotonically increasing

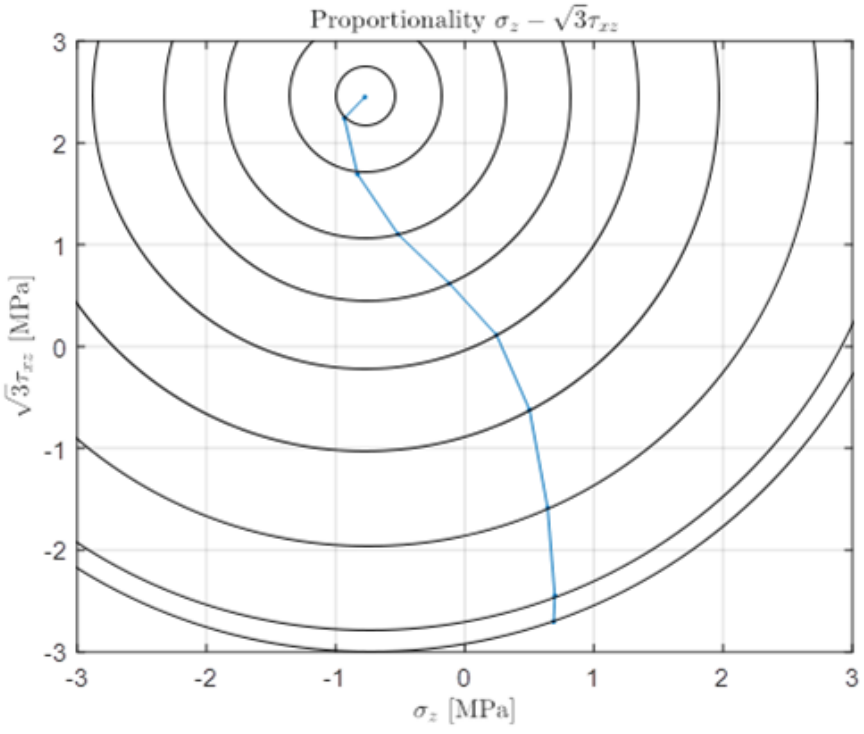

FIGURE E.5: All data points are monotonically increasing for this range

In the counting process the sum of the path is counted as an effective stress range as one half cycle. Because the considered range is monotonically increasing it will be completely

removed from the $\sigma - \sqrt{3}\tau$ proportionality plot, Figure E.6.

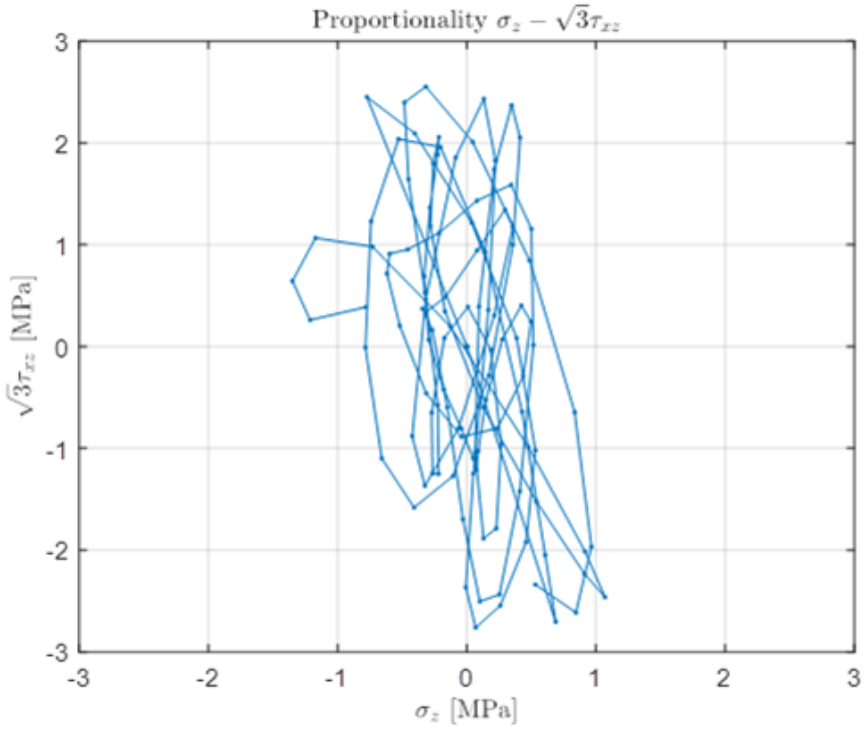

FIGURE E.6: $\sigma - \sqrt{3}\tau$ with removed counted range

Again the maximum range has to be determined for the remaining part of the $\sigma - \sqrt{3}\tau$ proportionality plot. The next maximum range is shown in Figure E.7.

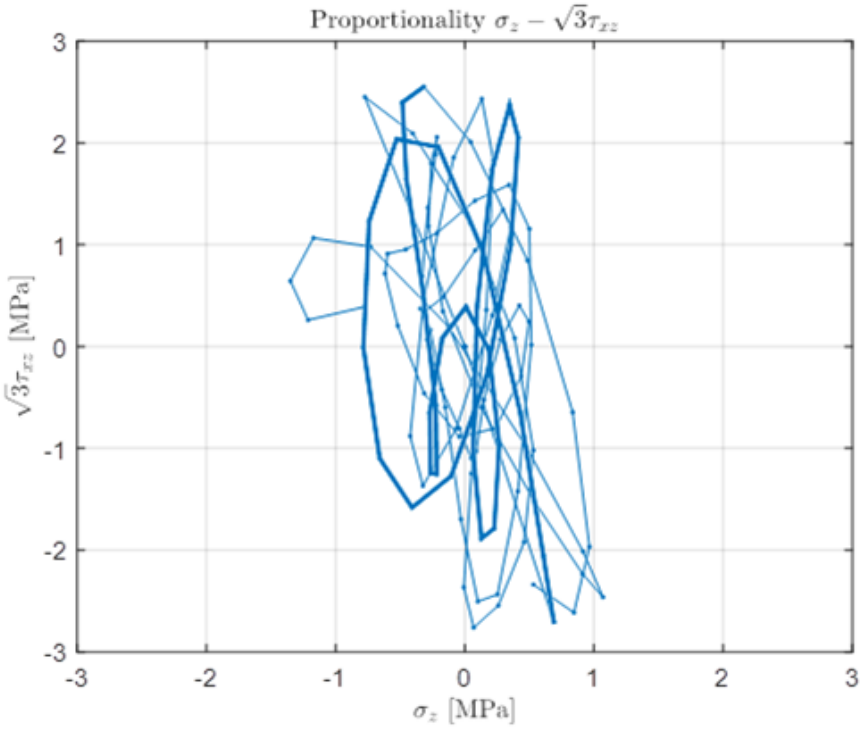

FIGURE E.7: Maximum range in remaining part of $\sigma - \sqrt{3}\tau$

Also for this range it has to be checked if the data points are monotonically increasing. By drawing the circles it becomes clear that for this range a different situation arises, Figures E.8 and E.9.

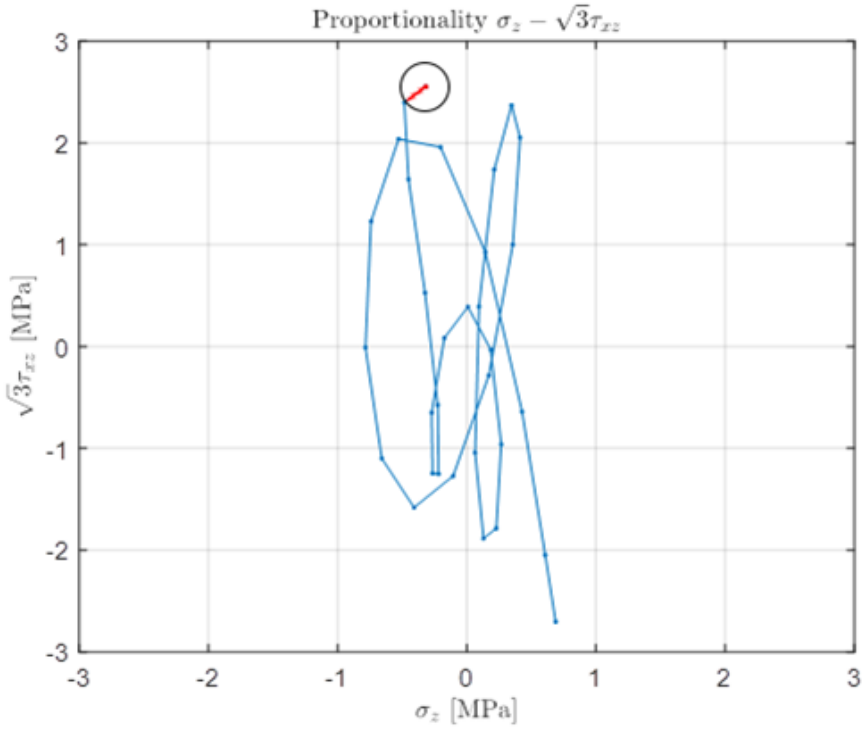

FIGURE E.8: First data point is monotonically increasing

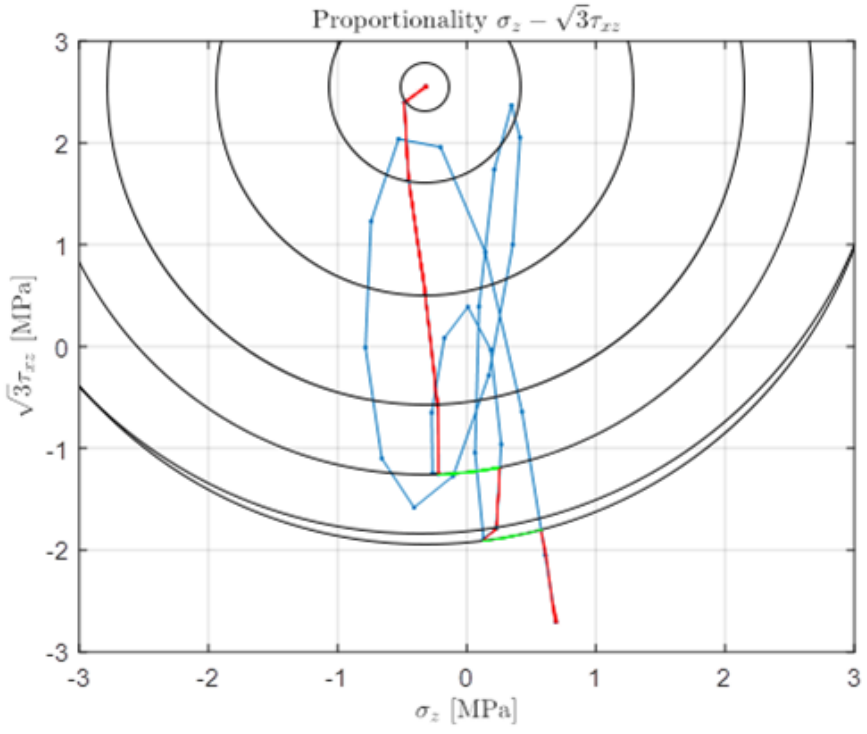

FIGURE E.9: But not all data points are monotonically increasing for this range

The red part in Figure E.9 is the part that is monotonically increasing. The green parts are the so called virtual paths. The blue parts are the parts of the path between the

virtual paths. In the counting process the sum of the red paths is counted as an effective stress range as one half cycle. Each green path is counted as an effective stress range as one half cycle. The blue path is not contributing to the counting process for now. So for this range 3 half cycles are counted.
The red path is removed and the blue part remains in the $\sigma - \sqrt{3}\tau$ proportionality plot, Figure .

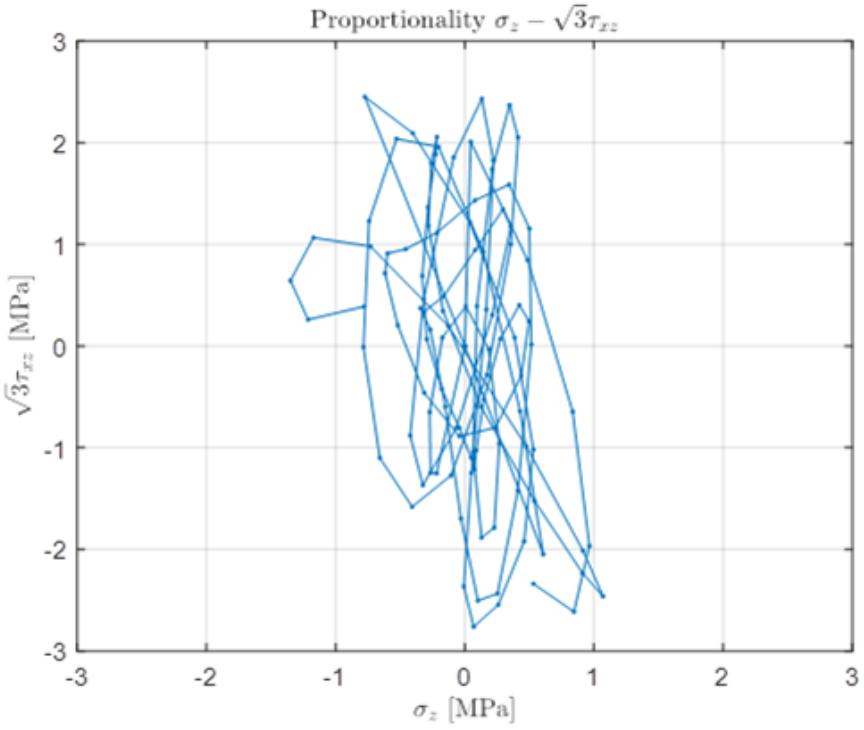

FIGURE E.10: $\sigma - \sqrt{3}\tau$ with removed counted range

The process of finding the maximum range, checking if it is monotonically increasing and counting the effective stress ranges continues until the $\sigma - \sqrt{3}\tau$ proportionality plot is completely counted and removed.

Appendix F

Absolute values of results

Table F.1: Fatigue damage factors after 2hr for different wind sea directions

Fatigue damage factor	**Wind sea 0deg**	**Wind sea 45deg**	**Wind sea 90deg**	**Wind sea 135deg**
$Df_{\sigma_{swell}}$	1.56e-11	1.56e-11	1.56e-11	1.56e-11
$Df_{\tau_{swell}}$	5.42e-10	5.42e-10	5.42e-10	5.42e-10
$Df_{\sigma_{sea}}$	1.97e-11	1.94e-11	1.88e-11	3.77e-13
$Df_{\tau_{sea}}$	4.45e-11	7.66e-9	6.27e-10	2.73e-10
$\sum Df$	6.22e-10	8.24e-9	1.20e-9	8.31e-10

Table F.2: Fatigue damage factors after 2hr for different wind sea directions

Fatigue damage factor	**Wind sea 0deg**	**Wind sea 45deg**	**Wind sea 90deg**	**Wind sea 135deg**
$Df_{\sigma_{p1}}$	6.45e-9	9.89e-9	2.21e-8	3.80e-9
$Df_{\sigma_{vm}}$	3.35e-9	2.69e-8	1.58e-8	6.25e-9
$Df_{\sigma-\sqrt{3}\tau}$	6.94e-8	8.66e-7	2.93e-7	1.23e-7

Table F.3: Fatigue damage factors after 2hr for different vertical elements

Fatigue damage factor	**Element 10843**	**Element 10844**
$Df_{\sigma_{swell}}$	1.56e-11	8.81e-11
$Df_{\tau_{swell}}$	5.42e-10	7.12e-10
$Df_{\sigma_{sea}}$	1.88e-11	1.86e-10
$Df_{\tau_{sea}}$	6.27e-10	8.41e-10
$\sum Df$	1.20e-9	1.83e-9

TABLE F.4: Fatigue damage factors after 2hr for different vertical elements

Fatigue damage factor	**Element 10843**	**Element 10844**
$Df_{\sigma_{p1}}$	2.21e-8	3.45e-8
$Df_{\sigma_{vm}}$	1.58e-8	1.98e-8
$Df_{\sigma-\sqrt{3}\tau}$	2.93e-7	5.20e-7

TABLE F.5: Fatigue damage factors after 2hr for a vertical and horizontal element

Fatigue damage factor	**Element 10843**	**Element 48866**
$Df_{\sigma_{swell}}$	1.56e-11	1.31e-12
$Df_{\tau_{swell}}$	5.42e-10	3.10e-10
$Df_{\sigma_{sea}}$	1.88e-11	7.50e-13
$Df_{\tau_{sea}}$	6.27e-10	2.80e-10
$\sum Df$	1.20e-9	5.91e-10

TABLE F.6: Fatigue damage factors after 2hr for a vertical and horizontal element

Fatigue damage factor	**Element 10843**	**Element 48866**
$Df_{\sigma_{p1}}$	2.21e-8	7.94e-9
$Df_{\sigma_{vm}}$	1.58e-8	8.00e-9
$Df_{\sigma-\sqrt{3}\tau}$	2.93e-7	1.27e-7

Bibliography

[1] Freyssinet International. Freyssinet join alliance to revolutionise offshore wind, 2011. URL `http://www.freyssinet.co.uk/freyssinet-join-alliance-to-revolutionise-offshore-wind`.

[2] Det Norske Veritas. Stability and watertight integrity. *DNV Offshore Standard C301*, October 2013.

[3] Det Norske Veritas. Environmental conditions and environmental loads. *DNV Recommended Practice C205*, October 2010.

[4] J.M.J. Journée and W.W. Massie. Offshore hydromechanics. *Delft University of Technology*, January 2001.

[5] J.M.J. Journée and L.J.M. Adegeest. Seaway for windows. *Theory manual*, December 2003.

[6] Det Norske Veritas. Structural design of offshore units (wsd method). *DNV Offshore Standard C201*, April 2011.

[7] R.C. Hibbeler. In *Mechanics of materials*. Prentice Hall Pearson, 2008.

[8] D. Radaj and C.M. Sonsino. In *Fatigue assessment of welded joints by local approaches*. Abington Publishing, 1998.

[9] A. Hobbacher. Recommendations for fatigue design of welded joints and components. *International Institute of Welding*, 2008.

[10] British Standard. Fatigue design and assessment of steel structures. *IIW-BS7608: Code of practice*, 1993.

[11] Bong-Ryul You and Soon-Bok Lee. A critical review on multiaxial fatigue assessments of metals. *International Journal of Fatigue*, 1995.

[12] C. M. Sonsino and M. Kueppers. Multiaxial fatigue of welded joints under constant and variable amplitude loadings. *Fatigue and Fracture of Engineering Materials and Structures*, 2001.

[13] M. Bäckström and G. Marquis. A review of multiaxial fatigue of weldments: experimental results, design code and critical plane approaches. *Fatigue and Fracture of Engineering Materials and Structures*, 2001.

[14] Det Norske Veritas. Global response analysis. *DNV Recommended Practice C103*, April 2012.

[15] ASTM. Standard practices for cycle counting in fatigue analysis. *ASTM International*, September 2005.

[16] J.K. Hong P. Dong, Z. Wei. A path-dependent cycle counting method for variable-amplitude multi-axial loading. *International Journal of Fatigue*, October 2009.

[17] Z. Wei P. Dong. A rapid path-length searching procedure for multi-axial fatigue cycle counting. *Fatigue and Fracture of Engineering Materials and Structures*, October 2011.

[18] Det Norske Veritas. Fatigue design of offshore steel structures. *DNV recommended Practice C203*, October 2011.

[19] J.K. Hong P. Dong. The master s-n curve approach to fatigue evaluation of offshore and marine structures. *Proceedings of OMAE04*, June 2004.

[20] T.P. Forte J.K. Hong. Fatigue evaluation procedures for multiaxial loading in welded structures using the batelle srtuctural stress approach. *Proceedings of OMAE2014*, June 2014.

[21] N. Shamsaei and A. Fatemi. Small fatigue crack growth under multiaxial stresses. *International Journal of Fatigue*, February 2013.

[22] R. Plank and G. Kuhn. Fatigue crack propagation under non-proportional mixed mode loading. *Engineering Fracture Mechanics*, October 1998.

[23] Strabag Offshore Wind. The strabag gravity foundation, 2013. URL `http://www.strabag-offshore.com/en/projects/strabag-serial-system/strabag-gravity-foundation.html`.